Fabrication and Electromagnetic Applications of Periodic Nanostructures.

by

Erik Hyde Anderson

S.B. Massachusetts Institute of Technology
(1981)
S.M. Massachusetts Institute of Technology
(1984)

Submitted in partial fulfillment of the requirements
for the degree of
Doctor of Philosophy
at the
Massachusetts Institute of Technology

©Massachusetts Institute of Technology, 1988

Signature of Author ____________________
Department of Electrical Engineering and Computer Science,
May 27,1988.

Certified by ____________________
Henry I. Smith, Thesis Supervisor

Accepted by ____________________
Arthur C. Smith, Committee on Graduate Students

MASSACHUSETTS INSTITUTE
OF TECHNOLOGY

JUL 26 1988

LIBRARIES

ARCHIVES

Fabrication and Electromagnetic Applications
of Periodic Nanostructures.
by

Erik Hyde Anderson

Submitted to the Department of Electrical Engineering and Computer Science on May 13,1988 in partial fulfillment of the requirements for the Degree of Doctor of Philosophy in Electrical Engineering.

Abstract

Several new techniques have been developed to fabricate periodic structures with linewidths less than 0.1μm. The first technique uses an achromatic holographic configuration in which both spatially and temporally incoherent sources of light, readily available in the deep-uv, can be used to produce very fine period gratings. This configuration has been feedback stabilized allowing long exposure times so that both weak sources of deep-uv and high resolution, low sensitivity resists such as PMMA can be used. A high-contrast grating with a period of 120nm has been fabricated. The achromatic configuration is extendable to even shorter wavelengths in the VUV and soft x-ray region. The second technique is the feedback stabilization of a conventional holographic lithography system. This system is in a cleanroom where unavoidable environmental disturbances create significant fringe noise, greatly reducing the contrast. An active feedback system modulates the phase of one arm of the interferometer canceling the effects of vibration and drift. The feedback system greatly increases the process latitude and useful area of the $\approx$ 200nm period gratings. A high resolution method for aligning gratings using a photoelastic modulator is described. This technique uses the the partial polarization property of fine period gratings and has a measured resolution of less than 1 arc-second. Third, a procedure for making "x-ray nanolithography" masks with electron beam generated patterns has been demonstrated. This process has been used to make and replicate x-ray masks with small area 100nm period ($\approx$ 50nm linewidth) gratings as well as arbitrary-shaped "device" patterns allowing researchers to combine the arbitrary-pattern, fine linewidth capability of electron beam lithography with the high contrast, large process latitude of x-ray lithography. Finally, a program for the rigorous eigenmode solution of Maxwell's equations in square wave grating structures has been implemented.

Thesis Supervisor: Henry I. Smith, Professor of Electrical Engineering.

Acknowledgments

The research results reported here took place during a period of several years and many people contributed to this effort. First and foremost, I would like to thank Professor Henry I. Smith who provided the scientific insight and guidance that was critical to the success to my projects. He has created an intellectual and physical environment where interdisciplinary research into important scientific and technical problems can be carried out. For this, an entire generation of students will be grateful. The key role of Jim Carter in transforming ideas into accomplishments, in my projects and those of most other workers in the lab, cannot be over emphasized. His talents and ability to get the job done in the quickest and most efficient manner has been critical to most of the scientific accomplishments made in our lab and to my work in particular. I would like to thank the technicians who keep the lab running, in particular, Tim Mclure and in the recent past Mark Porter, Darrell Roan, and Russell McDonnell.

I would like to thank Mark Schattenburg for his critical role in this work, particularly the x-ray nanolithography mask processing and holographic grating production. His requirements for better quality and larger area gratings were a motivating force for building the feedback system as well as other important improvements. Also critical to the x-ray nanolithography mask fabrication work was Margaret Hamnett, whose detailed knowledge of that process averted disaster at several points.

Dieter Kern and his colleagues at IBM deserves special recognition for the electron beam lithography part of this work. Under his guidance and with help from Steve Rishton, Hubert Schmid, Hans Luhn, and Joe Smyth we were able to accomplished our goals in a short time.

I would like to thank Alan M. Levine who is largely responsible for the PEM alignment technique which greatly surpassed his original AXAF requirements after we eliminated sources of error and drift.

I thank Tony Yen for his help and wish him well as he continues this work and makes practical use of some of the techniques described here (conventional and achromatic holographic fabrication of gratings and electron beam lithography) for quantum-effect electronics and other experiments.

Finally, I would like to thank my parents whose support, understanding and love has been so important to me and my friends who mean so much to me.

Contents

1 Introduction **9**

2 Achromatic Holography **14**

2.1 Introduction 14
2.2 Achromatic Holography Configuration 17
2.3 Experimental Results 25
2.4 Conclusion 28

3 Feedback Stabilization of Holographic Lithography **33**

3.1 Introduction 33
3.2 Details of Feedback Theory 34
3.3 Experimental Configuration 35
3.4 Conclusion 43

4 X-ray Nanolithography Masks from Electron Beam Lithography **44**

4.1 Introduction 44
4.2 Mask Fabrication Process 45
4.3 Experimental Results 51
4.4 Conclusion 51

5 Alignment of X-ray Gratings **67**

5.1 Introduction 67
5.2 Alignment Using the Partial Polarization of a Grating. . . . 68
5.3 System Resolution 72
5.4 Experimental Results 73
5.5 Conclusion 77

6 Electromagnetic Grating Theory and Calculations **78**

6.1 Introduction 78

6.2 Basic Equations 82

6.2.1 Solving the Basic Equations with the Matrix method 84

6.2.2 Solving the Boundary Conditions 89

6.3 Solving the Equations with the Algebraic Method 95

6.4 Sample Calculation Results 98

6.5 Conclusion 105

7 Summary and Future Work **106**

List of Figures

2.1 Conventional holographic lithography consists of generating an intensity pattern in space from the interference of two coherent beams. . . . 15
2.2 Configuration for achromatic holographic lithography. . . . 18
2.3 This figure shows the Wood's interferometer 20
2.4 This plot shows the first order efficiency for a quartz phase grating. . . . 23
2.5 This plot shows the minus second order efficiency of a pure phase grating. . . . 24
2.6 270nm-period grating exposed in photoresist using a Hg arc-lamp source, filtered for $\lambda \approx 365$nm. . . . 26
2.7 A 120nm-period grating pattern in PMMA exposed with an ArF excimer laser, $\lambda = 193$nm. . . . 29
2.8 A 120nm-period grating produced by achromatic holography, shadowed with aluminum and reactive ion etched in oxygen. 31

3.1 This shows the holographic configuration with feedback stabilization. . . . 36
3.2 Noise signal with and without feedback. . . . 37
3.3 An SEM micrograph of exposed photoresist profiles using feedback. . . . 39
3.4 An SEM micrograph of exposed photoresist without using feedback. . . . 41

4.1 X-ray nanolithography mask fabrication process. . . . 47
4.2 SEM micrograph of x-ray mask after CCl_2F_2 and O_2 RIE and just before gold electroplating. . . . 49

4.3 SEM micrograph of interdigitated fingers connected to pads replicated in 300nm of PMMA by x-ray nanolithography. . 52
4.4 Another SEM micrograph of interdigitated fingers connected to pads replicated in 300nm of PMMA by x-ray nanolithography. 54
4.5 SEM micrograph of a narrow line with gap pattern replicated in 300nm of PMMA by x-ray nanolithography. 56
4.6 Another SEM micrograph of a narrow line with gap pattern replicated in 300nm of PMMA by x-ray nanolithography. . 58
4.7 SEM micrograph of 85nm linewidth chevron structure with a pitch of 200nm replicated in 300nm of PMMA using x-ray nanolithography. 60
4.8 Another SEM micrograph of 85nm linewidth chevron structure with a pitch of 200nm replicated in 300nm thick PMMA using x-ray nanolithography. 62
4.9 SEM micrograph of 100nm-period grating (50nm nominal linewidth) replicated by x-ray nanolithography in 80nm of PMMA. 64

5.1 Grating alignment setup using a PEM. 70
5.2 SEM micrograph of a 200nm period x-ray transmission grating with Au lines electroplated to about 1μm and supported on a 1μm polyimide membrane. 74

6.1 The orientation of the grating with respect to the coordinate system. 83
6.2 This figure shows the three regions of interest: region I with the incident field, region II inside the grating, and region III where the transmitted waves propagate. 91
6.3 This shows the calculated first order efficiency for both the TE and TM polarization of a 200nm period pure phase grating etched in quartz (n=1.6) with a λ =193nm source as a function of depth and linewidth. 100
6.4 This shows the minus second order efficiency for both TE and TM polarizations with the incident wave at an angle of 75 degrees. 101

6.5 This plot shows the calculated zero order transmitted efficiency for a 200nm period Au grating with a linewidth of 0.5 as a function of depth. 102
6.6 This plot shows the calculated zero order transmitted efficiency for a 200nm period Al grating with a linewidth of 0.5 as a function of depth. 103
6.7 This plot show the zero order transmitted beam for Au and Al wire grid polarizer gratings. 104

Chapter 1

Introduction

Periodic and quasi-periodic microstructures have a long and rich history [1]. In 1821, Joseph von Fraunhofer invented the diffraction grating as we know it today. He produced ruled grooves on a metal surface and his finest grating was 12mm wide with 9600 grooves ($\Lambda = 1.25\mu$m). These gratings allowed him to measure the wavelength of light for the first time, explain the phenomenon of diffracted orders, derive and test the grating equation, and even discuss the effects of errors in the grating line positions. In 1874, Lord Rayleigh showed theoretically that a grating could have a higher resolution than a prism. It was not until much later, in 1880, that Henry A. Rowland, at John Hopkins University, built a ruling engine producing sufficiently high quality gratings that this theoretical advantage became a reality. Another grating researcher, Albert A. Michelson, made several important contributions to the art of grating fabrication, along with many other well known scientific achievements. He apparently demanded perfection in his gratings and as a result produced very few. One of the select few that he was satisfied with was dropped and ruined while being demonstrated to his guests at a dinner party. He suggested using an interferometer to control the motion of the ruling engine stage. This was implemented almost half a century latter at MIT by Harrison and Stroke (in 1955) and resulted in a major improvement in the quality of gratings that could be produced. An impressive fraction of all atomic, molecular, and astrophysical science is based on spectroscopic data derived from grating-based spectrometers.

The invention of the laser started a revolution in optics and a whole new field of research known as modern optics was born. The laser gave

researchers a highly coherent source of light. With this coherent source, large interference patterns could be generated and "holographic" methods for producing diffraction gratings were developed. It is difficult to trace the origin of the idea of using an interference pattern to produce gratings, but Michelson considered it as far back as 1915. With the development of high-power lasers in the late 1960's both Rudolph and Schmahl [2] in Germany and Labeyrie and Flamand [3] in France developed holographic techniques for grating fabrication. Since that time, considerable effort has gone into making gratings with high efficiency, low distortion, and in some cases smaller periods to measure shorter wavelength interactions. The emphasis of the work described here is on the development of technology to make very fine period gratings and other small structures in order to probe the short wavelength interactions of x-rays, electrons in solids, and other (not necessarily electromagnetic) diffraction phenomenon. Further, many of the techniques developed for periodic nanostructure fabrication can also be applied to arbitrary shaped patterns and are of general interest to the microstructure engineering community.

The generation of holographic gratings has depended on the development of lasers (with appropriate wavelengths) to expose photosensitive material. In order to expose finer and finer period gratings, shorter wavelength lasers are needed. However, in the deep-uv region of the electromagnetic spectrum (180nm-250nm) there are very few options available for the generation of coherent light. Rapid advances in excimer laser technology, have resulted in "line-narrowed" lasers that have quite good coherence properties. However, these lasers are still very expensive ($\approx$ \$100,000). Because deep-uv sources such as ordinary excimer lasers and arc-lamps have rather poor temporal and spatial coherence properties, compared to near-uv and visible lasers, an achromatic interferometer configuration that requires neither good spatial nor temporal coherence properties has been demonstrated. This achromatic configuration uses the dispersive properties of transmission gratings to produce an standing intensity pattern in space with half the period of the "parent" gratings. This intensity pattern is independent of both the source wavelength and angle of incidence. The spatial coherence of the source does determine the acceptable "depth of focus" so that extended sources require precise alignment. The temporal "coherence length" sets an upper bound on the allowed optical path length difference between the two arms. When using quartz disks for the parent gratings this constraint

determines how flat and parallel the substrates must be. Gratings were exposed using both a mercury arc-lamp, filtered for the "I" line $\lambda = 365$nm, and an ArF excimer laser, $\lambda = 193$nm. The contrast of these gratings was sufficient so that further processing steps such as shadowing, and reactive ion etching (RIE) were carried out. The finest period grating produced with this achromatic system was 120nm; the limit imposed by the wavelength of the ArF excimer laser is about 100nm. Because the power of many deep-uv sources is rather low, and the sensitivity of the high resolution resist material, PMMA, is also low, the exposure time is very long. To counteract the inevitable mechanical drift, a feedback compensator was incorporated into the system allowing arbitrarily long exposure times.

The combination of an achromatic holographic configuration and a drift compensating feedback loop allows for the use of modest deep-uv sources to produce very fine period gratings. These gratings are of great interest in several areas, such as x-ray spectroscopy, microstructure fabrication research, quantum-effect electronic device research, cryogenic compatible polarizers, soft x-ray interferometers, thin film materials research, and possibly atomic or molecular interferometers. The development of a feedback-compensated achromatic interferometer system represents a significant practical advance in the art of grating fabrication because a highly coherent or powerful source is no longer needed.

In order to fabricate high quality, large area gratings, with a conventional holographic lithography system placed in a clean room environment, an active feedback system has been developed. The vibration and noise levels encountered in the clean room environment are large enough so that passive mechanical vibration isolation alone is insufficient to produce high contrast fringes. By placing a beamsplitter above the substrate, forming a Mach-Zehnder interferometer, and measuring the fringe intensity as a function of time, a feedback signal can be generated. The feedback signal is proportional to the sine of the phase difference between the two arms. The feedback element, an ADP Pockels's cell, not only compensates for the slow fringe drift but also for the audio frequency vibrations, resulting in high contrast fringes. The feedback locking of the fringes allows one to make arbitrarily long exposures even in very "noisy" environments.

Electron beam lithography is a non-optical system for making fine period gratings and as well as other patterns. Electron beam lithography systems are able to "write" patterns of arbitrary geometry with extremely

small linewidths and are an important tool in microstructure research. Many e-beam systems have a laser interferometer controlled stage and can be thought of as a modern general-purpose "ruling" engine for producing arbitrary patterns. It is a sad fact of life that high resolution electron-beam systems are very expensive both to obtain and operate. Therefore a technique had been developed to produce high-contrast x-ray nanolithography masks using e-beam lithography, done off campus, and then replicate the masks at MIT using x-ray nanolithography. A collaborative arrangement was set up with the e-beam lithography experts at IBM's Yorktown Heights research lab to expose fine linewidth patterns using a high resolution system at IBM and then process the masks and replicate them at MIT. This arrangement has worked very well: 100nm period gratings, and ≈100nm linewidth "device" structures have been written and replicated. Although initially developed to study periodic structures, this technique is of general interest to the submicron structures and electronic "quantum device" researchers because arbitrary patterns can be generated and replicated. The combination of fine linewidth pattern generation using electron beam lithography and the high contrast, parallel replication process of x-ray nanolithography gives researchers the best of both technologies.

No matter how the fine-period gratings are made, in most practical applications precise alignment to other elements of the system is needed. For example, diffraction gratings with periods of 200nm must be properly oriented in an x-ray spectrometer with respect to the detector. A high resolution technique has been developed using the partial polarization property of these gratings and a photoelastic modulator (PEM). This technique uses a lock-in amplifier to measure a signal that is proportional to the sine of twice the angle between the crystal axis of the PEM and the grating lines. A resolution of better than 1 arc-second has been measured. This system will be used in the alignment of several hundred gratings on the AXAF x-ray telescope satellite and may also be used on other x-ray spectroscopy instruments giving a simple and easy-to-implement solution to what otherwise can be a very difficult alignment problem.

Another difficult problem to solve is the accurate prediction of grating performance for a wide range of wavelengths and different materials. For example, when making the gratings for the achromatic interferometer it is important to know what the optimum depth and linewidth parameters are. These gratings are used with a wavelength that is comparable to the

grating period, the scalar diffraction theory is no longer valid. Another example where electromagnetic calculations are needed is the performance of "wire grid" polarizers. A wire grid polarizer consists of conducting grating lines (i.e. Au or Al) with a period much smaller than the wavelength on a transparent substrate. Light polarized with the electric field polarized parallel to the grating lines is reflected much more and transmitted much less than light polarized perpendicular to the grating lines. Complete electromagnetic vector theory is needed for these gratings. To analyze these different situations a computer program has been written and tested to solve the electromagnetic problem of a rectangular wave (lamellar) grating structure. Most of the gratings produced by our lab are essentially rectangular wave structures so the lack of generality is not a serious shortcoming. Further, more general shapes can be approximated by many layers of rectangular wave gratings. The program rigorously solves Maxwell's equations using the eigenmode approach where the wave equation is translated into an infinite matrix equation. The grating eigenmodes correspond to the eigenvalues of this infinite matrix and the eigenvalues of a truncated matrix are good approximations of the true grating eigenmodes. These eigenvalues are then "polished" to be exact roots of a transcendental equation. After the eigenmodes are found, the boundary conditions of continuous tangential electric and magnetic fields at the front and back of the grating are used to solve for the undetermined constants giving the exact field. This program has been very useful in understanding and predicting various diffraction grating phenomena.

Chapter 2

Achromatic Holography

2.1 Introduction

This chapter closely follows the author's paper "Achromatic Holography in the Deep UV" [4]. For many applications of gratings in optoelectronics [5], quantum effect devices [6], and diffractive x-ray optics and spectroscopy [7], very small periods are needed. For some applications the smaller the grating period the better the performance. For example, the dispersion of an x-ray diffraction grating is proportional to the line density (spatial frequency), and in most x-ray spectrometer configurations the energy resolution is proportional to the dispersion.

Currently, nearly all fine-period gratings are made with conventional holographic lithography where a periodic intensity pattern in space is produced by the interference of two coherent beams, as shown in Fig. 2.1 The period of this intensity pattern, Λ, is directly proportional to the wavelength of the source and inversely proportional to the sine of half the angle between the incoming beams:

$$\Lambda = \frac{\lambda}{2\sin(\theta)}. \tag{2.1}$$

This intensity pattern is usually recorded in photoresist as part of a multistep process to produce a desired structure [8],[9]. To generate a standing intensity pattern with a period of 100nm (in free space) requires a source wavelength less than 200nm. Unfortunately, such deep UV sources generally lack either the temporal or spatial coherence, or both, to yield gratings

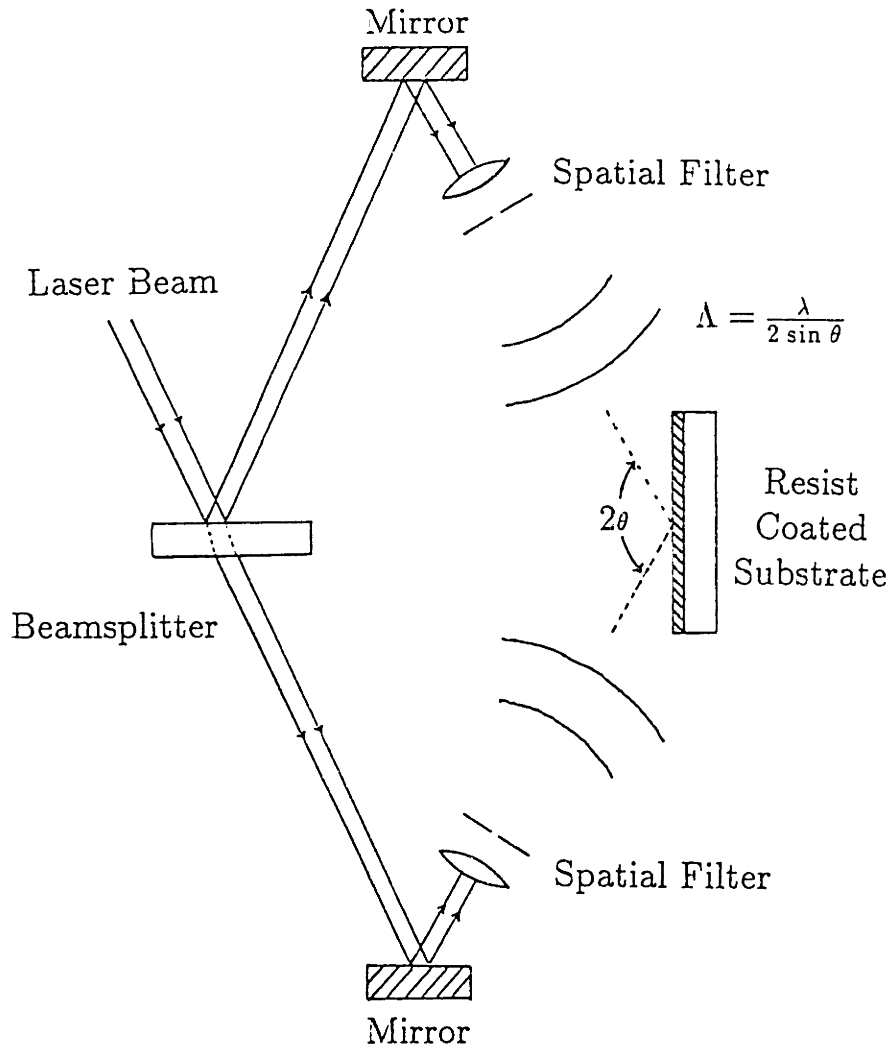

Figure 2.1: Conventional holographic lithography consists of generating an intensity pattern in space from the interference of two coherent beams. In the usual set up, a beamsplitter splits the beam of a coherent laser source into two parts. These two beams are directed by mirrors through a spatial filter to clean up spatial "noise" caused by scattering from imperfections and dust. Sometimes a collimating lens is used to reduce the curvature of the wavefront after the spatial filter. The spatially filtered and perhaps collimated, beams overlap at the substrate plane resulting in an intensity pattern with period $\Lambda = \lambda/(2\sin\theta)$.

with a large number of lines. The number of high contrast fringes in a conventional configuration is limited by the temporal coherence and is given by

$$N \approx \frac{\nu}{\Delta\nu}, \tag{2.2}$$

where ν and $\Delta\nu$ are the source frequency and bandwidth respectively.

Several attempts have been made to fabricate very fine period gratings while circumventing the requirement of a coherent deep-UV source. One technique is to use a high refraction index medium to lower the effective wavelength of a mid-UV laser source [10]. A high-index prism was placed on a photoresist-coated substrate, with a xylene index-matching fluid in between. Grating periods of 110nm were obtained. However, it is difficult to get highly uniform exposure with such evanescent coupling. Also, conventional photoresist has a natural granularity which leads to ragged line edges at $\approx$ 100nm periods. Another approach is to generate the required deep-UV wavelength by non-linear optical techniques [11]. However, this requires a sophisticated optical set up in order to properly phase match the harmonic generating non-linear crystals or gas cells. Further, most popular nonlinear crystals become opaque in the deep-uv region.

A state-of-the-art "linewidth-narrowed" ArF excimer laser, $\lambda = 193$nm, with a coherence length of about 2mm ($\nu/\Delta\nu \approx 10^4$) was tested to produce gratings in a conventional holographic configuration. High contrast fringe patterns could be produced during each pulse. But the pattern would shift significantly from pulse to pulse because of small changes in the angle of the beam as well as low level vibration in the interferometer. The maximum allowable change in angle, $\Delta\alpha$, from pulse to pulse is given by

$$\Delta\alpha \ll \frac{\Lambda}{l} \tag{2.3}$$

where l is the length of the interferometer arm. If only one pulse is needed to expose the resist, excellent gratings were produced, but not otherwise. Further, the cost of a line-narrowed excimer laser is on the order of $100,000, which makes the purchase of such a laser an expensive obstacle to producing very fine period gratings.

Earlier, a simple achromatic technique, called "near field spatial frequency doubling" [12] which is compatible with deep-UV sources having poor coherence, was investigated. This technique uses the achromatic characteristics of the intensity pattern in the near field of a parent grating with

the zero order suppressed. However, gratings made with this technique still have a Fourier component at the fundamental spatial frequency, which is a problem in some applications, such as spectroscopy. The complete suppression of the zero order is difficult if not impossible and the degree to which the zero order must be suppressed is a quadratic function of the allowed tolerance of the fundamental Fourier coefficient. For example, if the application for the grating can tolerate no more that 0.1% fundamental component then the zero order must be suppressed by a factor of 10^6.

A far-field holographic configuration that allows the source to have both large bandwidth, $\Delta\nu$, and angular spread has been demonstrated [4]. This achromatic configuration can be used with a wide variety of sources in the deep-UV, such as arc-lamps and short-coherence-length excimer lasers. In order to stabilize this system over long exposure times, a feedback network has been included in the achromatic design. The exposure time using our "museum vintage" excimer laser is 15 to 20 minutes, and the allowable drift over this time period must be less that a small fraction of the final grating period. A HeCd laser ($\lambda = 335$nm) is used to monitor the drift and a piezoelectric translator makes corrections in the position of the optical elements to lock the fringes in place so that the inevitable mechanical drift is no longer an exposure-time limiting constraint.

2.2 Achromatic Holography Configuration

The basic idea of using gratings to make a balanced configuration was presented by Weinberg and Wood [13] in 1959, and a detailed study of making holograms with partially coherent light was published by E.N. Leith and B.J. Chang in 1973 [14] as well as Y.S. Cheng [15]. The achromatic holographic scheme is shown in Fig. 2.2. The first grating, with period Λ, acts as a beamsplitter and diffracts the incoming light into plus and minus first-order beams. The zero-order beam is subsequently blocked by a stop. The second grating recombines the two beams by diffracting them back towards the substrate. If the recombiner grating has the same period as the beamsplitter, this diffraction is second order. When the optical distance from the first to the second grating is the same as the optical distance from the second grating to the substrate the intensity pattern at the substrate has a period half that of the beamsplitter grating, independent

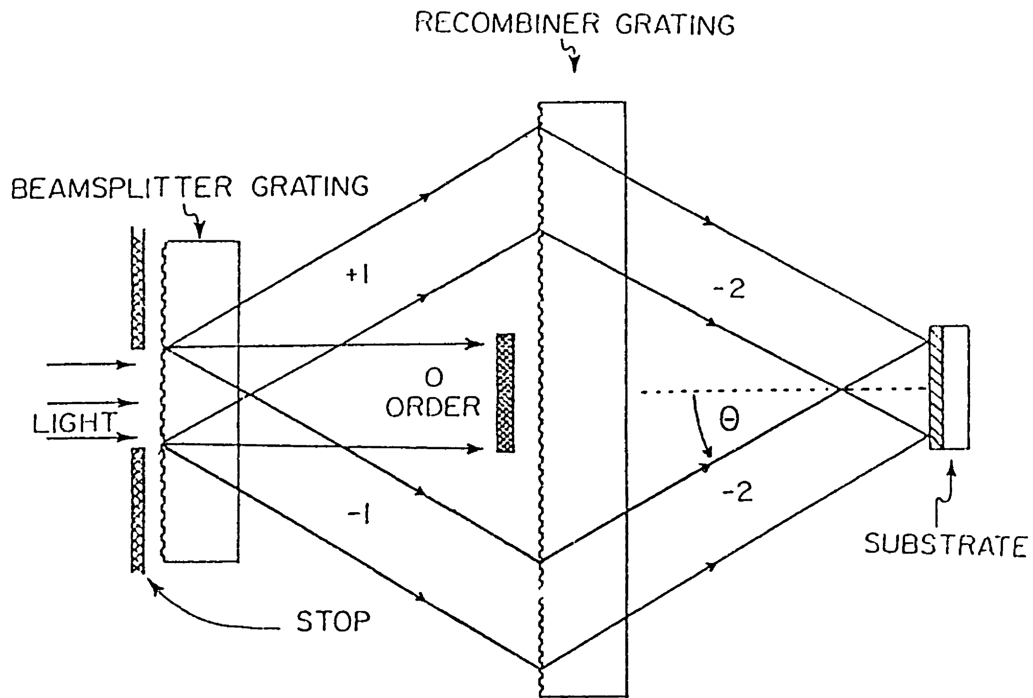

Figure 2.2: Configuration for achromatic holographic lithography consisting of a set of identical-period gratings. The beamsplitter grating diffracts the incoming light into plus and minus first-order beams. The recombiner grating diffracts these two beams back to the substrate. A beam stop blocks the beamsplitter's zero order.

of the source wavelength and the angle of the input beam. It is easy to show that this intensity pattern period at the substrate, $P/2$, is independent of the wavelength. Consider a source with wavelength λ. The diffraction condition requires that the angle θ in Fig. 2.2 is

$$\sin(\theta) = \frac{\lambda}{\Lambda}. \tag{2.4}$$

From the equation 2.1 the final grating period is then given by

$$\begin{aligned} \Lambda_{\text{final}} &= \frac{\lambda}{2\sin(\theta)} &(2.5)\\ &= \frac{\lambda}{2(\frac{\lambda}{\Lambda})} &(2.6)\\ &= \frac{\Lambda}{2} &(2.7) \end{aligned}$$

It is more difficult, although straightforward, to show that the registration of different wavelengths is correct and that the result is independent of the input angle. Suppose that a monochromatic plane wave is incident on the interferometer at a small angle α. See Fig. 2.3. The incident wavefunction will be

$$\psi(x,z) = Ae^{i(k_x x + k_z z)} \tag{2.8}$$

where

$$\begin{aligned} A &= \text{amplitude} \\ k_x &= \frac{2\pi}{\lambda}\sin(\alpha) \\ k_z &= \frac{2\pi}{\lambda}\cos(\alpha). \end{aligned}$$

In region I of Fig. 2.3 ψ is given by

$$\begin{aligned} \psi_A^I(x,z) &= At_1 e^{i(k_x + \frac{2\pi}{\Lambda})x} e^{ik_{z1}z} \\ \psi_B^I(x,z) &= At_1 e^{i(k_x - \frac{2\pi}{\Lambda})x} e^{ik_{z2}z} \end{aligned}$$

where

$$k_{z1} = \sqrt{\left(\frac{2\pi}{\lambda}\right)^2 - \left(\frac{2\pi}{\Lambda} + \frac{2\pi}{\lambda}\sin(\alpha)\right)^2}$$

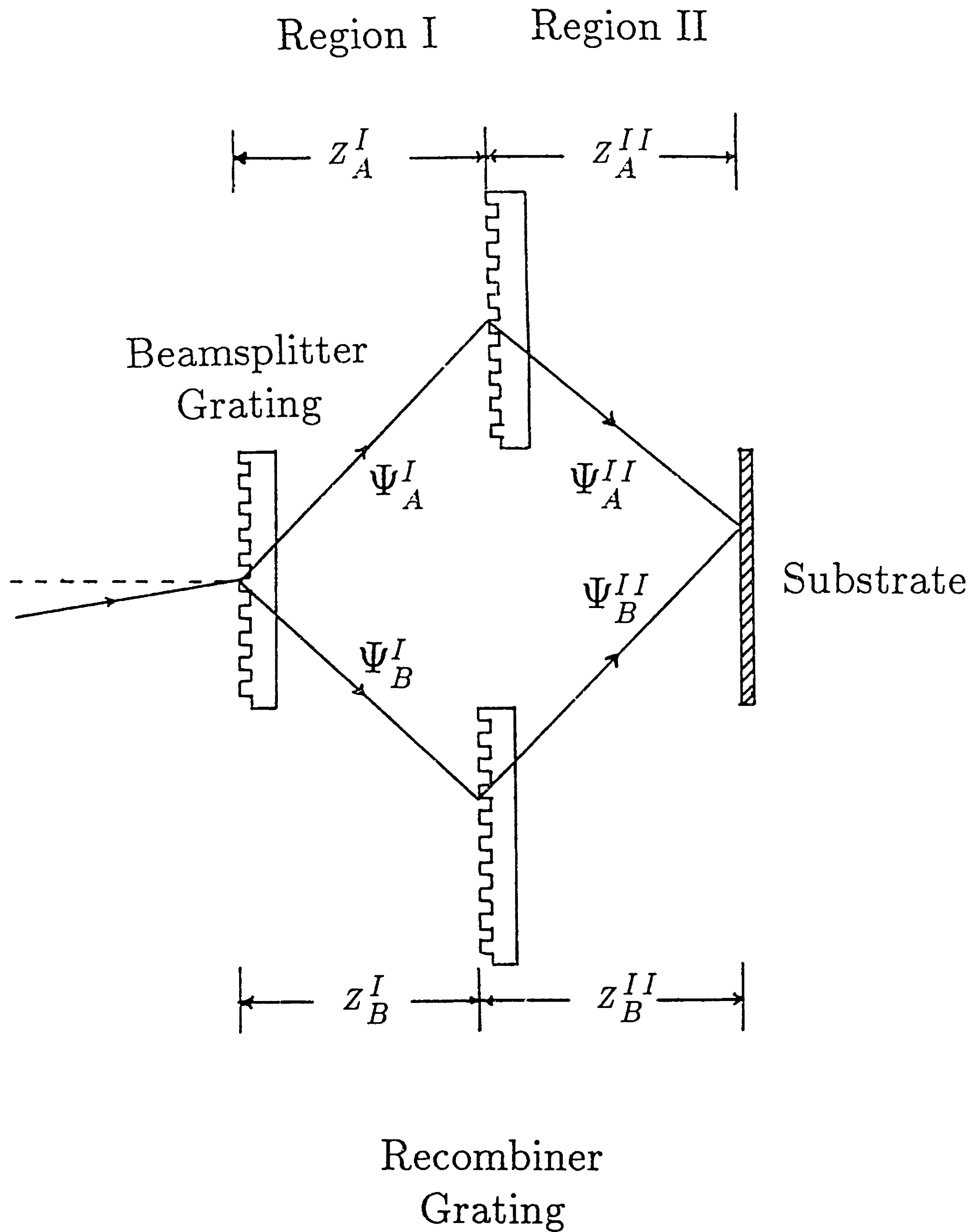

Figure 2.3: This figure shows the Wood's interferometer with a plane wave incident at an angle of α. For simplicity the zero order beam is not shown since it would normally be blocked by a beam stop.

$$
\begin{aligned}
k_{z2} &= \sqrt{\left(\frac{2\pi}{\lambda}\right)^2 - \left(\frac{2\pi}{\Lambda} - \frac{2\pi}{\lambda}\sin(\alpha)\right)^2} \\
t_1 &= \text{first-order transmission amplitude}
\end{aligned}
$$

Now in region II, ψ is given by

$$
\begin{aligned}
\psi_A^{II}(x,z) &= At_1t_2e^{i(k_x-\frac{2\pi}{\Lambda})x}e^{ik_{z1}z_A^I}e^{ik_{z2}(z-z_A^I)} \\
\psi_B^{II}(x,z) &= At_1t_2e^{i(k_x+\frac{2\pi}{\Lambda})x}e^{ik_{z2}z_B^I}e^{ik_{z1}(z-z_B^I)} \\
t_2 &= \text{second-order transmission amplitude}
\end{aligned}
$$

Thus

$$
\psi_A^{II}(x,z) + \psi_B^{II}(x,z) = At_1t_2e^{ik_xx}\left(e^{i\phi_A(z)}e^{-i\frac{2\pi}{\Lambda}x} + e^{i\phi_B(z)}e^{+i\frac{2\pi}{\Lambda}x}\right) \tag{2.9}
$$

where

$$
\begin{aligned}
\phi_A(z) &= k_{z1}z_A^I + k_{z2}z_A^{II} \\
\phi_B(z) &= k_{z2}z_B^I + k_{z1}z_B^{II}
\end{aligned}
$$

When the system is in perfect alignment, i.e. $z_A^I = z_B^{II}$ and $z_B^I = z_A^{II}$, then

$$
|\psi_A + \psi_B|^2 = 4I_0t_1t_2\cos^2\left(\frac{2\pi}{\Lambda}x\right) \tag{2.10}
$$

where the parameters λ and α do not appear. The spatial period and *position* of this intensity pattern are determined by the parent grating, independent of source wavelength and incident angle. If the system is not in perfect alignment, but is "defocused" by a small amount, Δz, then

$$
\begin{aligned}
\phi_A &= \phi_A(z_0) + k_{z2}\Delta z \\
\phi_B &= \phi_B(z_0) + k_{z1}\Delta z
\end{aligned}
$$

Taylor expanding $(k_{z1} - k_{z2})$ to find that

$$
|\psi_A + \psi_B|^2 = 4I_0t_1t_2\cos^2\left(\frac{2\pi}{\Lambda}x + \frac{2\pi\sin(\alpha)}{\Lambda\cos(\beta)}\Delta z\right) \tag{2.11}
$$

where

$$
\frac{2\pi}{\lambda}\cos(\beta) = \sqrt{\left(\frac{2\pi}{\lambda}\right)^2 - \left(\frac{2\pi}{\Lambda}\right)^2}. \tag{2.12}
$$

From this equation it is clear that Δz must be small enough so that

$$\frac{2\pi\sin(\alpha)}{\Lambda\cos(\beta)}\Delta z << \frac{\pi}{4}. \tag{2.13}$$

When the interferometer is well aligned there is an intensity pattern in space that is independent of the wavelength and spatial frequency of the input wavefront. Thus, the phase and period of the intensity pattern are determined by the parent gratings and do not depend on the source characteristics. From equation 2.13 the allowable Δz is small when a conventional source is used. For example, if $\Delta\alpha$ is about 1/2 degree then Δz must be less than about $4\mu m$. This makes sense because "white light" interferometers need to have small path length differences. In a real interferometer, there will be a difference in the optical path lengths between one arm and the other due to thickness variations in the parent gratings. These path length differences cannot be eliminated by any adjustments of the alignment since they are characteristic of the parent gratings. The difference in optical path length must be kept less than the coherence length of the source to get high contrast fringes. Therefore, when selecting materials for the parent gratings the optical parallelism and flatness of the substrates are important parameters.

One drawback to the configuration shown in Fig. 2.2 is that the second order diffraction efficiency of the second set of transmission gratings is generally small. For a phase grating etched in quartz, 10 percent efficiency has been measured, although numerical calculation show that much higher efficiencies are possible with optimum linewidth and depth parameters. This is illustrated in Fig. 2.4 and 2.5. If a third grating is placed in the substrate location, an achromatic interferometer configuration results which is very useful for alignment purposes and feedback control. The low overall efficiency of this configuration, coupled with the low brightness of deep-uv sources available in our lab and the low sensitivity of high-resolution resists, such as PMMA, conspire to require very long exposure times. The exposure time can be on the order of 20 minutes. In even the most solid mechanical systems there will be some mechanical drift due to temperature variations, air currents and other sources of disturbance. The amount of allowable drift must be a small fraction of the final grating period for high contrast fringes. A feedback system is used to correct for this mechanical drift. A monitor grating is kept in place during the exposure and a laser

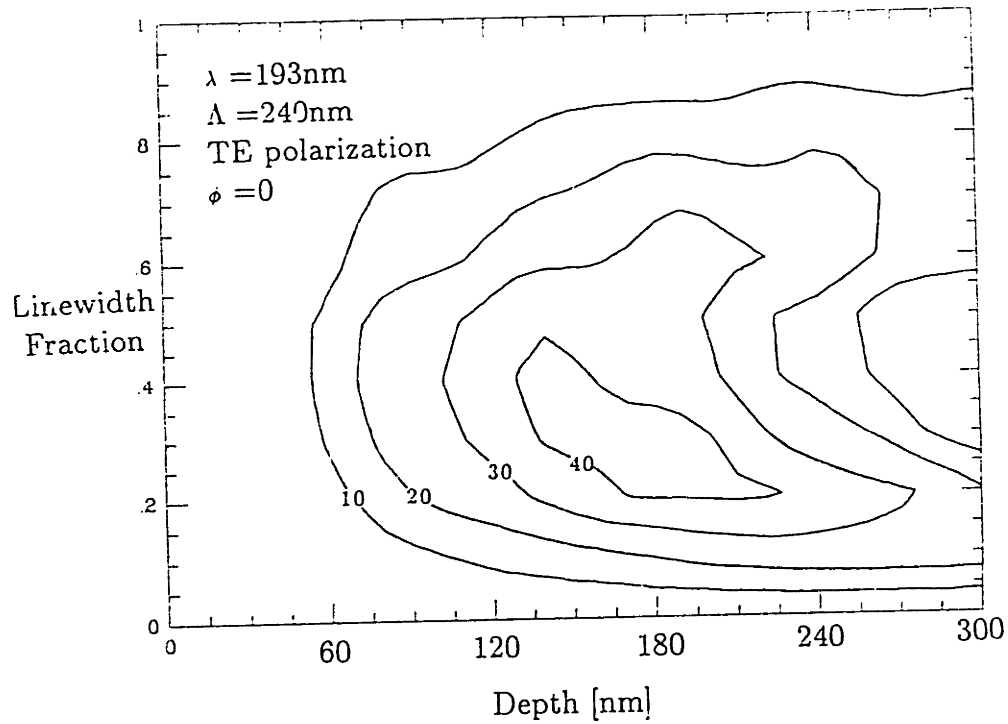

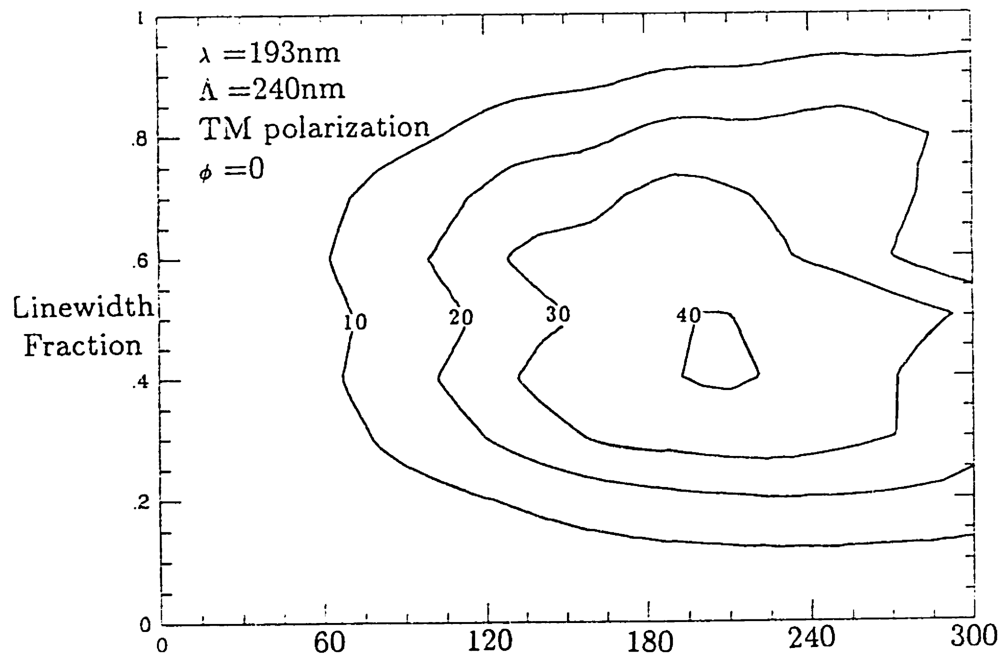

Figure 2.4: This plot shows the first order efficiency for a quartz phase grating (n = 1.6) with a period of Λ = 240nm and a source wavelength of λ = 193nm as a function of linewidth and etch depth, for both the TE (top) and TM (bottom) polarizations. Each contour represents a 10% intensity level. Plots are based on rigorous electromagnetic calculations.

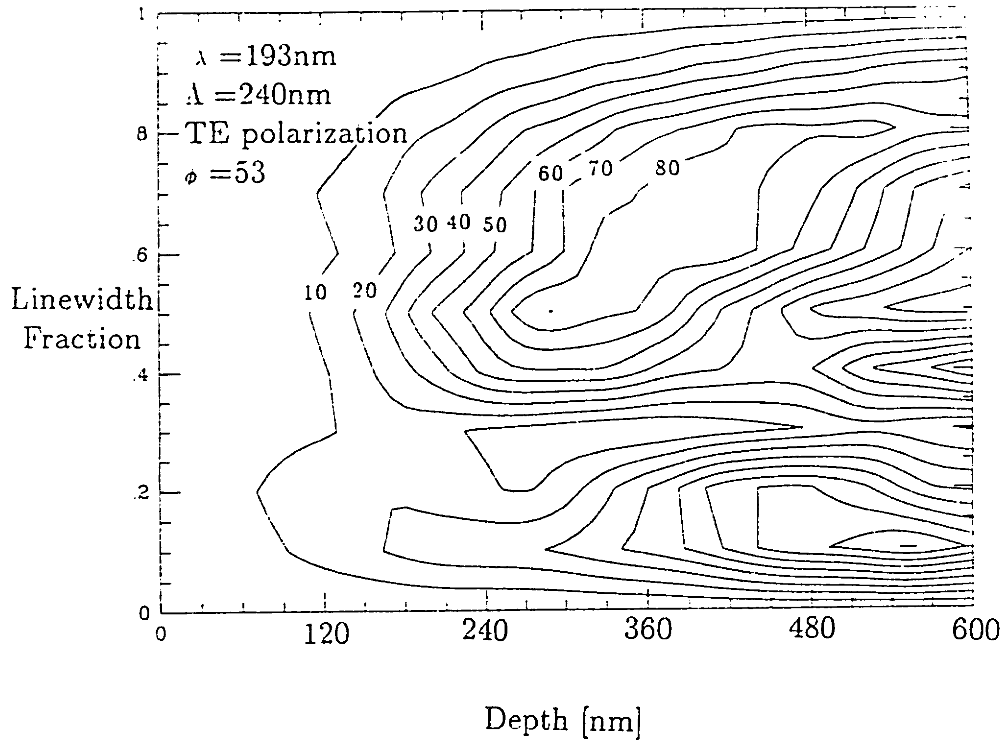

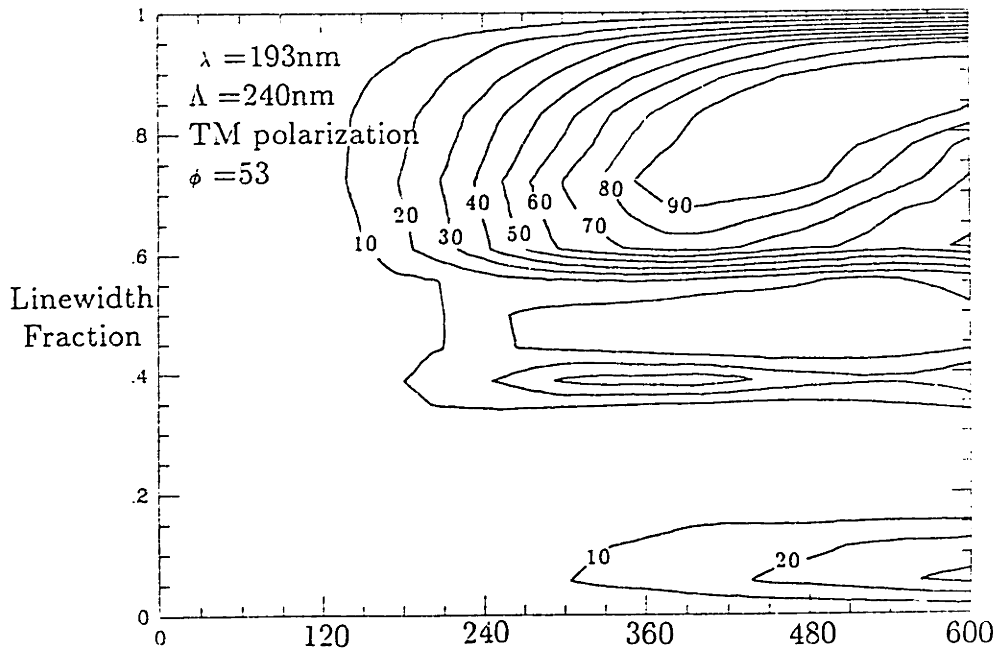

Figure 2.5: This plot shows the minus second order efficiency of a pure phase grating ($n = 1.6$) with a period of $\Lambda = 240$nm at a source wavelength of $\lambda = 193$nm and with the incident wavefront at an angle $\phi = 53$ degrees, as a function of linewidth and etch depth for both the TE (top) and TM (bottom) polarizations. Each contour represents a 10% intensity level.

beam probes the interferometer for changes in position of the fringe pattern. The probe beam will have well spaced moiré fringes due to the slight misalignment or distortion of the gratings. This moiré pattern is sensed by two photodiodes connected to a differential amplifier. If the moiré fringe pattern moves in one direction, one diode signal will become larger and the other will become smaller. A feedback network amplifies this error signal, filters it, and drives a piezoelectric translator that pushes on the recombiner grating, reducing the error signal and therefore closing the loop. With this feedback loop, the interferometer has negligible mechanical drift for very long periods of time.

Since the number of high-contrast fringes produced with this configuration is independent of the source characteristics, the size of the final grating is limited only by the sizes of the parent gratings or any obstructions in the light paths. If a single recombiner grating is used, then the maximum final grating size is limited to about one third the width of the recombiner grating. However, if two separate recombiner gratings are used then the final grating size is limited to the width of the smallest of the three parent gratings.

2.3 Experimental Results

Two sets of gratings were fabricated using conventional holographic lithography to test the achromatic configuration. The first set, having a period of 540nm, was used with the 365nm line of a mercury arc lamp. A second set of gratings had a period of 240nm and was used with both an ArF excimer laser, $\lambda = 193$nm, and the $210 - 220$nm radiation from a cadmium-xenon arc lamp. Both sets were pure phase gratings etched in UV-grade fused silica (Supersil 2) to a depth designed to optimize the appropriate diffracted orders: plus and minus first order for the beamsplitter and second order for the recombiner grating. A third grating was placed in the substrate plane for alignment and feedback control. When strong fringes were visible behind this third grating the system was in alignment. A HeCd laser was used for feedback control.

The achromatic features of this system are apparent as the source is moved to simulate large changes in the incident angle and the fringe pattern behind the third grating stayes constant.

Figure 2.6: 270nm-period grating exposed in photoresist using a Hg arc-lamp source, filtered for $\lambda \approx 365$nm.

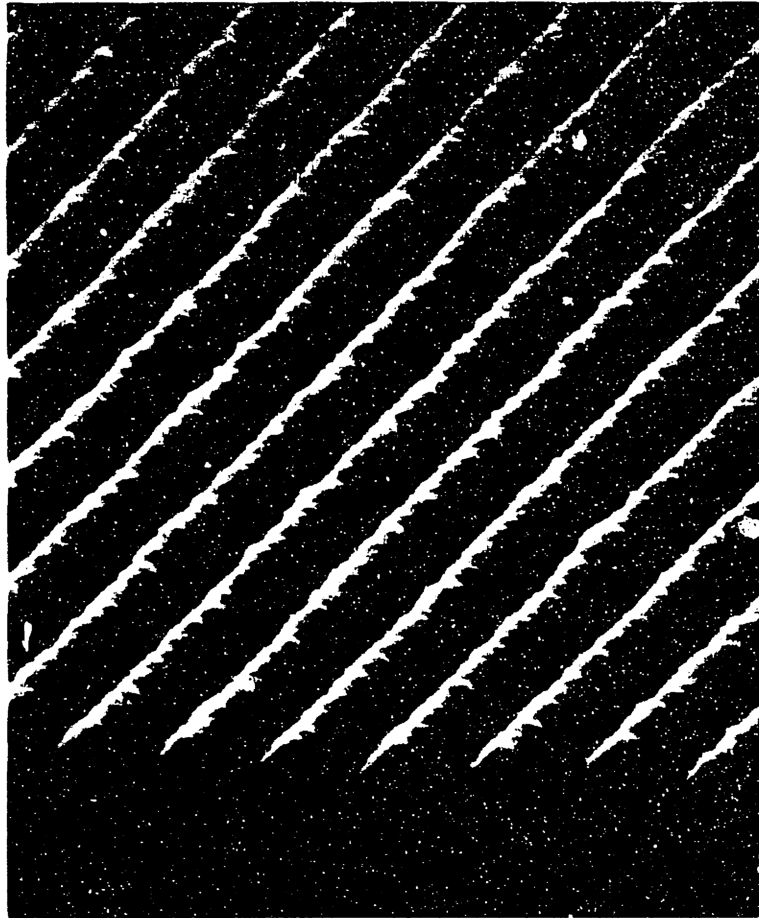

270*nm* Period Grating in
Photoresist made using
Achromatic Holographic Lithography
Hg Arc-Lamp Source $\lambda = 365nm$

Figure 2.6 shows the photoresist profile resulting from exposure with a Hg arc-lamp source filtered for the 365nm line in conjunction with the 540nm-period grating set. This profile is about the same as we obtain using an Ar-ion laser in a conventional holographic configuration [8]. Figure 2.7 shows the pattern produced in PMMA with an ArF excimer laser in conjunction with the 240nm-period set of gratings. The depth of modulation in the resist is sufficient so that subsequent processing by metal deposition, reactive-ion-etching, liftoff, electroplating, or other processes can yield useful structures for optical, electronic or other devices. For example, Fig. 2.8 shows a 120nm-period grating that has been shadowed with aluminum and reactive-ion-etched, resulting in 40nm wide lines. A grating with this aspect ratio can be used in further processing steps such as liftoff, etching, and electroplating.

2.4 Conclusion

A far-field achromatic holographic system has been built and tested using mid-UV and deep-UV sources to expose grating patterns. A Hg arc lamp source, $\lambda = 365$nm, was used with 540nm-period parent gratings to expose 270nm-period gratings in photoresist, and an ArF excimer laser, $\lambda = 193$nm, was used to expose 120nm-period gratings in PMMA. The system works well with spatially incoherent sources that have a large bandwidth, making it especially useful in the deep-UV region. A feedback system has been incorporated to control the mechanical drift, reducing the net drift to a negligible value over long time periods. Exposure times as long as 20 minutes have been needed to expose the high-resolution but low sensitivity PMMA resist. This configuration can be extended into the vacuum UV and soft x-ray regions, and is a potential candidate for molecular interferometry with low energy atoms using free standing gratings [16].

Figure 2.7: A 120nm-period grating pattern in PMMA exposed with an ArF excimer laser, $\lambda = 193$nm.

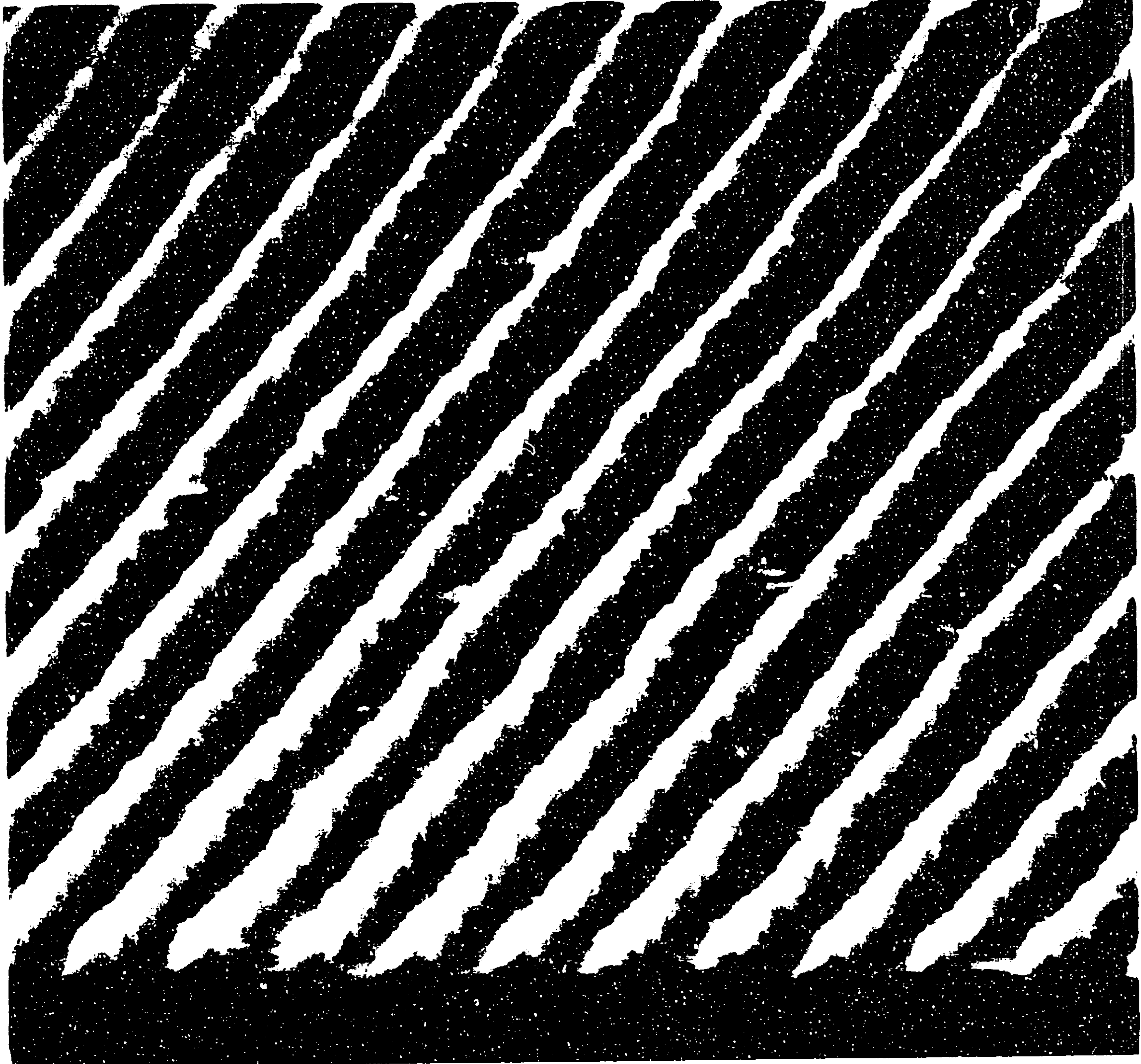

120nm Period Grating
in PMMA
Produced by
Achromatic Holography

Figure 2.8: A 120nm-period grating produced by achromatic holography, shadowed with aluminum and reactive ion etched in oxygen. The linewidth is about 40nm and this structure can be used for further processing such as liftoff, etching, and electroplating.

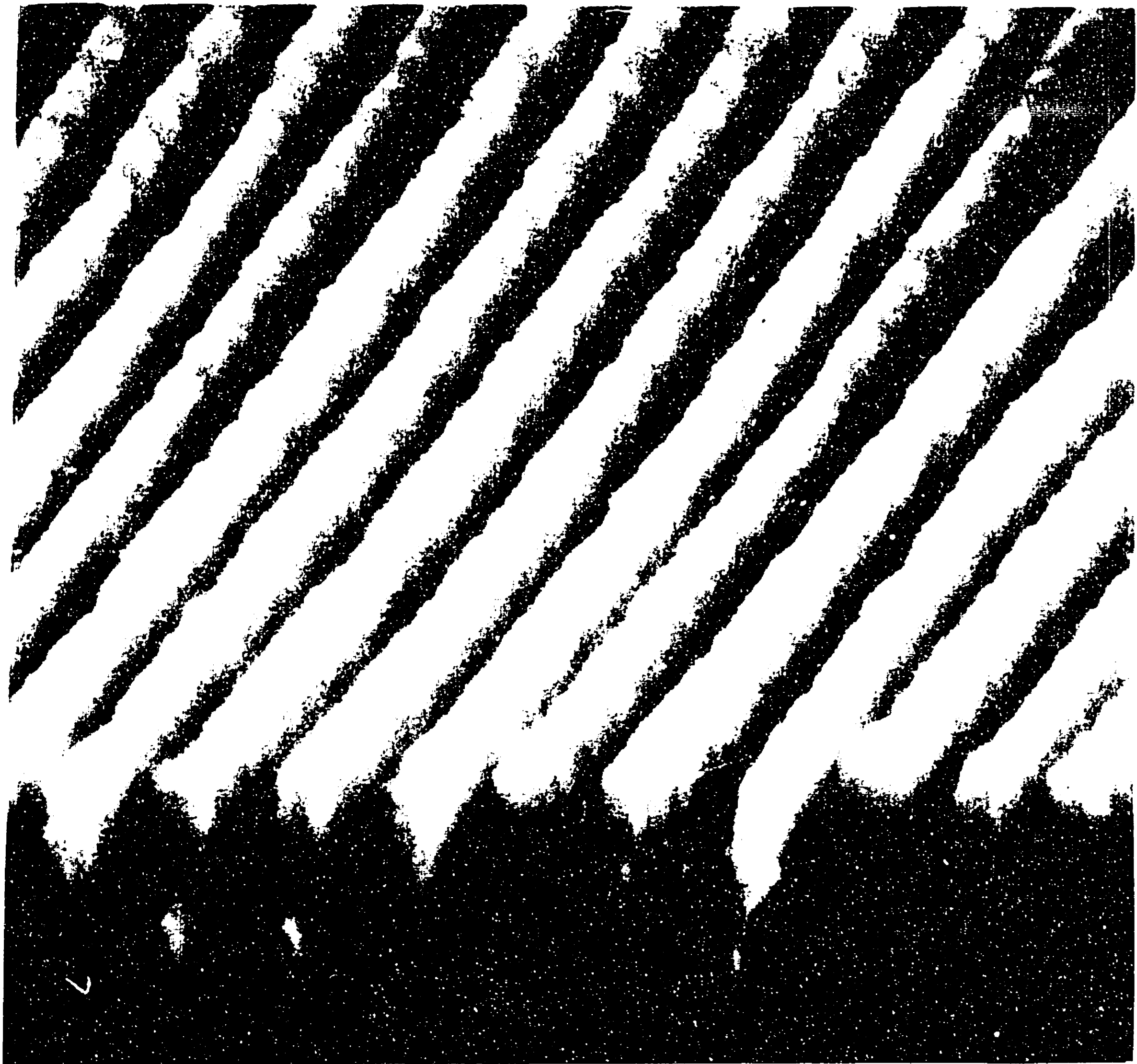

120nm Period Grating
Produced by
Achromatic Holography,
Shadowing and RIE

Chapter 3

Feedback Stabilization of Holographic Lithography

3.1 Introduction

In a conventional holographic lithography system, the interference of two coherent beams produces an intensity pattern in space that can be used to expose photosensitive material. As the period of this intensity pattern becomes finer, even small vibrations that could be ignored for larger period gratings can seriously degrade the fringe contrast. This problem becomes even worse when the holographic system must be in an environment, such as a clean room, where large amounts of acoustic noise, mechanical vibrations, and air currents excite the mechanical modes of the optical configuration, degrading the stability of the fringes. Passive measures such as using a high quality optical table with pneumatic vibration isolation mounts are insufficient in this high noise environment. Previous workers have used feedback to compensate for slow drift using a mechanical servo system [17], but the audio-frequency mechanical vibrations encountered in the current system need to be attenuated as well.

In order to produce high contrast fringes, an active feedback system has been developed, as shown in Fig. 3.1. In this system a beamsplitter is placed above and behind the substrate (to be out of the way but still within the overlap of the two beams) forming a Mach-Zehnder interferometer. A pair of photodiodes is used to measure the intensity signal of both interference patterns. By power conservation, the sum of the signals measured in each

arm is proportional to the laser output power, which is approximately constant. The diodes are connected to a differential amplifier which subtracts one diode signal from the other. With this configuration, a signal proportional to the sine of the phase difference between the two interferometer arms is produced and the common mode signals such as the room lights are effectively canceled. The output of this differential amplifier modulates a high-voltage power supply which in turn drives an ADP-crystal Pockels cell. The Pockels cell modulates the phase of one of the interferometer arms thereby closing the feedback loop. The high gain of the feedback loop keeps the difference between the two photodiode signals very small resulting in a stable fringe pattern. An advantage of using two diodes and taking the difference is that the fringe pattern is largely independent of the ambient light level and the laser output power. A change in the laser output power will only produce a change in the loop gain and the fringe position is insensitive to the loop gain if it is large enough.

The active feedback system holds the fringe pattern constant during the exposure even when large external sources of mechanical disturbances are present. This greatly increases the contrast of the intensity pattern allowing a much larger process latitude in terms of exposure and development times as well as better grating profiles after development.

3.2 Details of Feedback Theory

The difference of the signals from the two photodiodes is proportional to the sine of the phase difference in the path lengths of the two interferometer arms. This phase difference as a function of time consists of two terms: a term representing the phase of the Pockels cell and a phase term due to the noise (vibration, air currents, etc) of the system.

$$\phi_{\text{Total}} = \phi_{\text{Noise}} + \phi_{\text{Pockels}} \tag{3.1}$$

Let V_a be the gain of the amplifier electronics, in order to reduce the effect of the noise our feedback equation becomes:

$$\phi_{\text{Pockels}} = -\pi \frac{V_a}{V_\pi} \sin(\phi_{\text{Pockels}} + \phi_{\text{Noise}}) \tag{3.2}$$

where V_π is the π phase shifting voltage for the Pockels cell. If the feedback system is working properly then the Pockels cell phase, ϕ_{Pockels}, will

be almost equal and opposite to the noise phase disturbance, ϕ_{Noise}. Under these conditions the sine function can be expanded in a Taylor series, keeping only the first order terms:

$$\phi_{\text{Pockels}} = -\pi \frac{V_a}{V_\pi}(\phi_{\text{Pockels}} + \phi_{\text{Noise}}). \tag{3.3}$$

Solving this equation for the total phase difference gives

$$\phi_{\text{Pockels}} + \phi_{\text{Noise}} = \frac{1}{1 + \frac{\pi V_a}{V_\pi}} \phi_{\text{Noise}}. \tag{3.4}$$

For a moderate amount of loop gain, $\pi V_a / V_\pi$, the noise term can be substantially reduced.

3.3 Experimental Configuration

Figure 3.1 shows the experimental configuration. A conventional holographic lithography configuration is modified by placing an ADP Pockels cell phase modulator in one arm. A beamsplitter is placed above and behind the substrate to be out of the way and thus not scatter light onto the substrate but still be in the overlap of the two beams. The beamsplitter forms a Mach-Zehnder interferometer whose output intensity is monitored by two photodiodes. The photodiodes are connected to a differential current amplifier to produce a signal proportional to the sine of the phase difference between the two arms. This signal is fed into a high-voltage audio-frequency-bandwidth amplifier which drives the Pockels cell, closing the feedback loop. Figure 3.2 shows the oscilloscope traces when the fringes are locked and not locked for an interferometer configuration that uses the entire 8 foot length of the optical table. The noise in the fringes without feedback is effectively larger than the grating period resulting in contrast much too small for useful grating exposure. With the fringes locked, good gratings can be generated. Figures 3.3 and 3.4 show the difference between exposed grating profiles with and without feedback respectively.

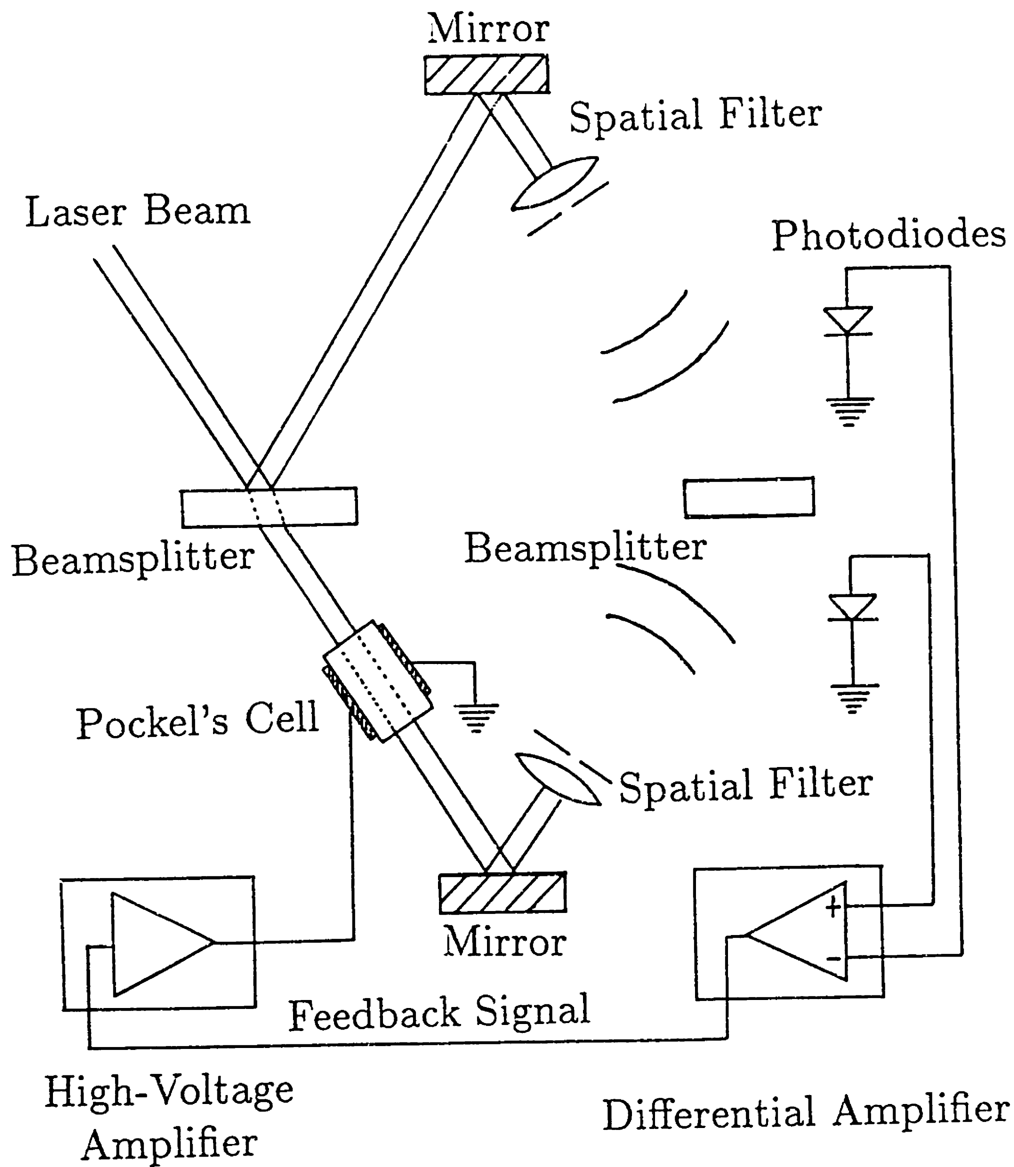

Figure 3.1: This shows the holographic configuration with feedback stabilization. A beamsplitter is placed in the overlap of the two coherent beams but out of the way of the substrate so that no spurious scattering onto the substrate will occur. Two photodiodes measure the intensity of the fringes on both sides of the beamsplitter. The difference of these two intensities is proportional to the sine of the phase difference between the two arms. This signal is amplified and used to drive the Pockels cell in one arm. The pockels cell introduces phase shift that almost completely cancels the noise introduced by mechanical vibration and other disturbances.

Figure 3.2: The top oscilloscope trace, showes a signal proportional to the sine of the phase noise, without the feedback loop for a interferometer configuration that uses the entire 4 by 8 foot area of an optics table in a clean room environment. The noise is much larger than the period of the grating to be exposed and therefore the contrast is well below a usable level. The bottom trace shows the signal with a loop gain of about 15. The residual noise is essentially zero, resulting in high contrast fringes that can be used to expose a large area grating and allow a large process latitude.

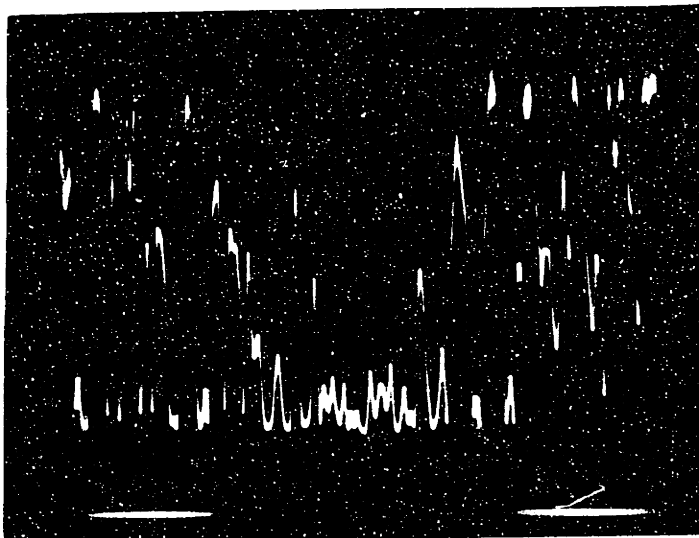

Without Feedback

|←100 msec→|

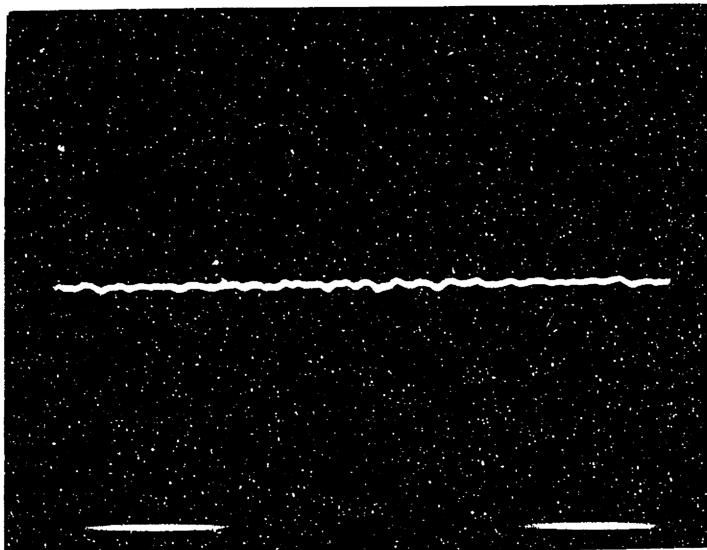

With Feedback

Fringe Phase-Error Signal

Figure 3.3: An SEM micrograph of exposed photoresist profiles using feedback. The feedback greatly increases the fringe contrast.

200nm

Photoresist Profiles Exposed
Over Anti-Reflection Layer
With Feedback-Locking of Fringes.

200nm

Photoresist Profiles Exposed
Over Anti-Reflection Layer
With Feedback-Locking of Fringes.

Figure 3.4: An SEM micrograph of exposed photoresist without using feedback. The contrast is so poor that there is no hope of producing a good grating from this exposure.

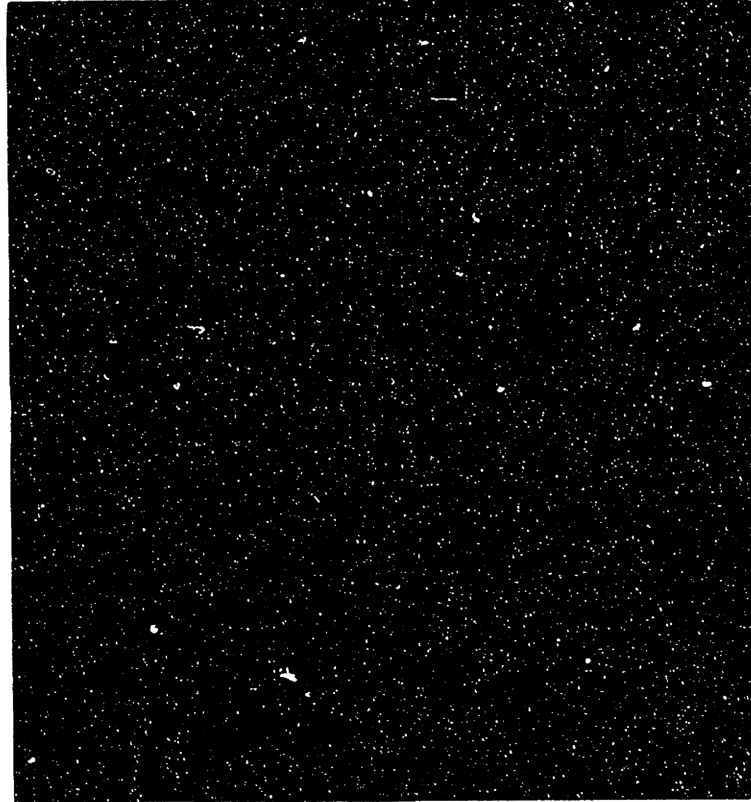

Photoresist Profiles Exposed
Over Anti-Reflection Layer
Without Feedback-Locking of Fringes.

3.4 Conclusion

When holographically fabricating gratings with submicron periods, small levels of vibration that are present with even the best optics tables and pneumatic vibration isolation mounts can seriously degrade the fringe contrast. This problem is much worse when the holographic system is in an unfavorable environment such as a clean room. In order to overcome this problem, an active feedback system has been developed to "lock" the fringes by modulating the phase in one arm of the interferometer with an ADP Pockels cell. The feedback signal is derived from a beamsplitter placed above and behind the substrate which forms a Mach-Zehnder interferometer. In the extreme case of very long interferometer arms and long exposure times this system makes possible large area gratings with excellent photoresist profiles. In the same configuration, with the feedback system turned off, no usable resist structures could be made.

The technique of active feedback holographic fringe locking should be extendable beyond grating fabrication to more general holograms. In this case, a simple beamsplitter cannot be used to generate the feedback signal. However, a poor quality transmission hologram of the desired object can be used in place of the beamsplitter and a bootstrap procedure employed to generate very high-contrast fringes over arbitrarily long exposure times.

Chapter 4

X-ray Nanolithography Masks from Electron Beam Lithography

4.1 Introduction

This chapter follows the publication "Fabrication by Tri-Level Electron Beam Lithography of X-Ray Masks with 50nm Linewidths, and Replication by X-Ray Nanolithography," given at the 1987 Microcircuit Engineering conference in Paris [18] with additional details. A process has been developed to produce x-ray nanolithography masks containing fine linewidth patterns generated by scanning-electron-beam lithography. This technology allows researchers to combine the high resolution, arbitrary-pattern-generation capability of electron-beam lithography with the parallel replication, high contrast, and large process-latitude of x-ray nanolithography. A tri-level structure was used that consisted of PMMA as the electron-sensitive material, titanium as the middle, masking layer, and polyimide as the buffer layer on top of a gold plating base. After electron-beam exposure and development, the pattern is transferred to the Ti layer by CCl_2F_2 reactive-ion etching (RIE), and then a polyimide mold is produced by O_2 RIE. Gold is then electroplated into this mold to form the x-ray absorber. X-ray masks with 100nm-period gratings and electronic device patterns of $\approx$ 100nm linewidths were fabricated by this process and replicated.

Scanning-electron-beam lithography is an essential tool for producing

patterns of arbitrary geometry with linewidths of 100nm or less. In those applications where large areas (≈mm^2) of fine-linewidth features are needed, the e-beam writing time can become extremely long. There are several reasons for this. First, the beam diameter is usually kept substantially smaller than the linewidth for improved process control. For approximately constant beam current density, the beam current falls off proportional to the square of the linewidth. Second, for a given linewidth there is an upper limit of resist sensitivity set by "shot noise" considerations [19]. This is observed in practice where high resolution e-beam resists such as PMMA are much less sensitive than other lower-resolution resists. Based on the theory described in [19], the exposure time per unit area should increase at least as rapidly as the inverse fourth power of the linewidth for fully dense patterns, and more rapidly than this for minimal line edge raggedness.

A high-resolution replication technique, in which the information is transferred in parallel, is an ideal complement to electron-beam lithography since large areas of fine linewidth patterns can be copied over and over again in a small fraction of the time needed to produce them with an e-beam system. Contact x-ray nanolithography has demonstrated minimum lines and spaces of 17.5nm [20], and with the proper resist is probably capable of ≈ 10nm linewidth. It has excellent contrast and minimal proximity effects, allowing high-aspect-ratio structures to be produced with a large process latitude. Although our x-ray nanolithography system has only a very crude alignment capability many interesting research projects have been carried out [21,22,23]. Microgap x-ray nanolithography, in which the mask and substrate are separated by a small controlled gap of a few micrometers [24], promises to be a low-distortion, high-resolution process with improved alignment capability. In order to combine the advantages of parallel replication by x-ray nanolithography and the fine linewidth, arbitrary-pattern-generation capability of electron-beam lithography a new process has been developed for making high-contrast x-ray masks. Using these masks, features as small as 50nm have been replicated.

4.2 Mask Fabrication Process

This project was a collaborative effort between MIT and Dieter Kern's electron beam lithography group at IBM's Yorktown Heights Research lab

where the electron beam patterns were written. The first step in any mask fabrication process is to design the pattern. It would be impractical for researchers at MIT to travel to IBM each time a design needed changing, a method of transferring data generated at MIT to IBM was developed. The method of sending data turned out to be rather simple since the output of the CAD tools at MIT is in the form of a CIF file [25]. The computer-aided-design program, KIC, can be instructed to use a very small subset of the CIF commands, consisting only of boxes and their coordinates. A short program then translates this output into the format used by the IBM pattern generator pre-processor programs. A data file, in the correct format, is sent by electronic mail to IBM Yorktown Heights Research lab via the ARPA and BIT net, allowing designers at MIT to easily and quickly send their designs to IBM. This ability to generate patterns at MIT and then send them automatically to IBM is a significant asset in utilizing electron beam generated x-ray nanolithography masks for research projects. The process described below shows how to make a useful x-ray nanolithography mask with features as small as 50nm from data sets generated by the CAD tools at MIT.

An x-ray nanolithography mask consists of a frame and an x-ray transparent membrane patterned with an absorber material such as gold or tungsten. An outline of the tri-level process used to make such masks with e-beam lithography is shown in Fig. 4.1. For the membrane material, 1.25μm of polyimide [26] was used. This material is quite strong and transmits 65% of the carbon-K ($\lambda = 4.5nm$) x-rays. The first step is to spin the polyimide onto a silicon wafer and cure it. Experience has shown that a high temperature bake of 400C in flowing nitrogen (to prevent carbonization) for 45 minutes produces membranes that are much stronger and less permeable to water than those baked at lower temperatures [27]. After the membranes are cured, the plating base of 10nm of Cr (for adhesion) and 15nm of Au is evaporated onto the polyimide. Next, a second layer of polyimide is spun on to give a thickness of 160nm, and cured at 250C. (Since this layer does not require mechanical strength it is not baked at 400C). After the second polyimide layer is cured, a thin 7.5nm layer of Ti is evaporated. Finally, the resist material, 80nm of PMMA, is spun onto the substrate and baked at 175C for several hours. After spinning on the PMMA, the substrates are at the state shown in Fig. 4.1 (a) and are ready to be exposed by scanning-electron-beam lithography.

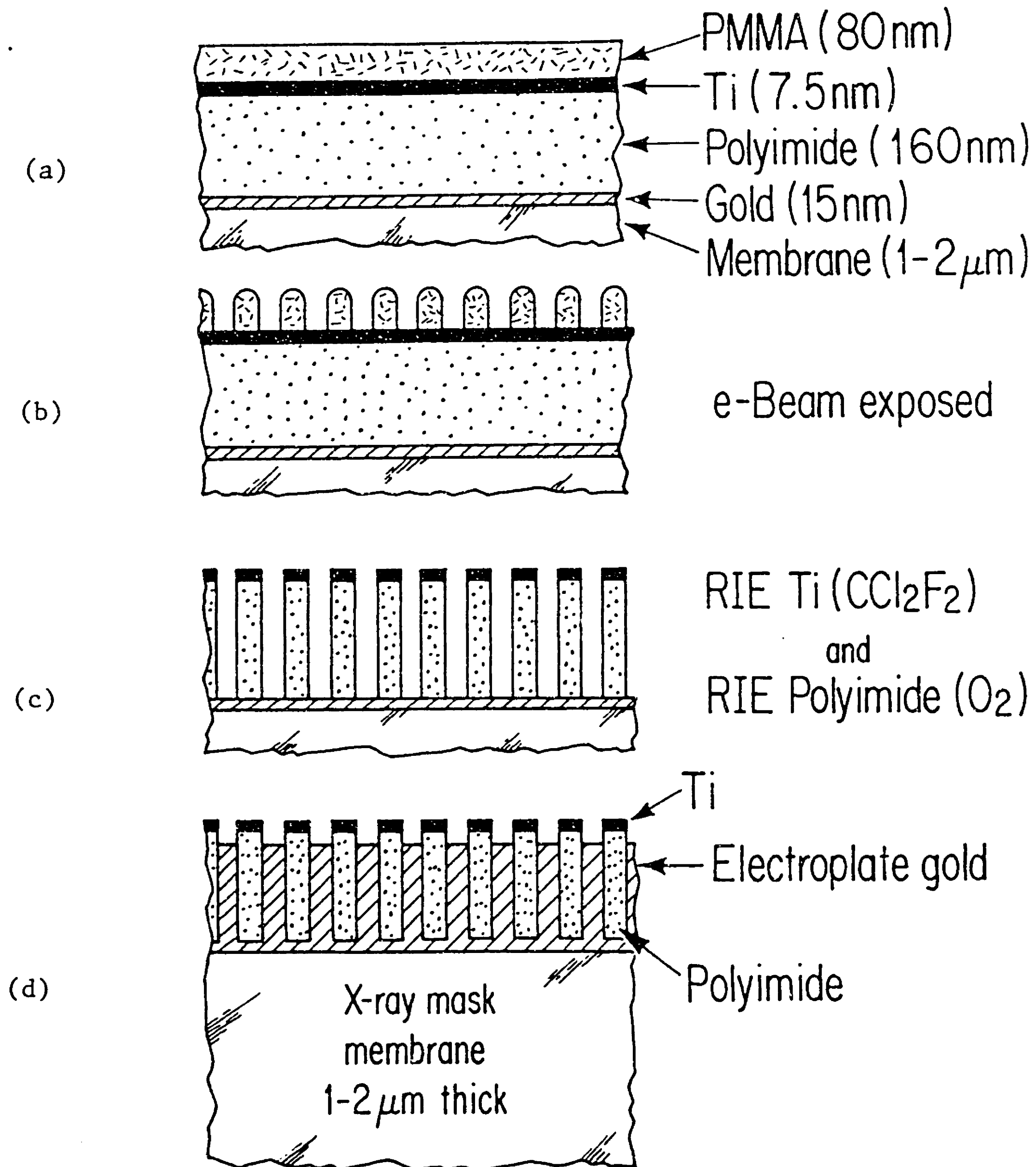

Figure 4.1: X-ray nanolithography mask fabrication process. The substrate before exposure is shown in (a). Starting from the top there is an 80nm PMMA layer followed by 7.5nm of Ti and 160nm of polyimide on top of a gold plating base (10nm Cr, 15nm Au). Another polyimide layer of 1.25μm serves as the membrane material after the silicon wafer, not shown, is etched away. After electron beam exposure and development (b), the pattern is transferred to the Ti by CCl_2F_2 RIE which then forms a tough etch mask for the O_2 RIE of the polyimide layer (c). Gold is electroplated into the polyimide mold forming the x-ray absorber (d).

Several patterns were exposed using the vector scan VS-6 electron-beam lithography system [28] at IBM's Yorktown Heights research lab: a grating with a period of 100nm and several 100nm-linewidth device patterns. The beam diameter, FWHM, was estimated from "knife edge" measurements to be about 20nm (i_b=40pA) for the device patterns having linewidths of about 100nm, and about 10nm (i_b=10pA) for the 100nm-period grating. The dose was about 100μC/cm^2 for the device patterns, and about 1nC/cm (100μC/cm^2) for the 100nm-period grating. After exposure, the samples were developed in solution of 2:1 IPA:MIBK at 21.0C (development temperature control is very important) for 45 seconds.

Next, the titanium layer must be reactive-ion etched (RIE) using the PMMA as a mask. As was reported by Unger et al., [29] the etch selectivity between PMMA and Ti is generally very poor. Because the PMMA is much thicker than the Ti this poor selectivity can be tolerated. Good results were obtained using CCl_2F_2 with a chamber pressure of 10mTorr, DC bias voltage of 600 volts and power density of about 0.23 watts/cm^2 with a quartz target. The etch rate for Ti under these conditions is about 30nm/minute. The PMMA etches at a much faster rate than the Ti, but, since the total time is so short (16 seconds), the pattern is transferred to the Ti layer without significant linewidth change. Next, the Ti is used as a mask for reactive-ion-etching the polyimide buffer layer in O_2. Since the Ti layer forms a tough oxide that is highly resistant to etching under oxygen ion bombardment, 7.5nm of Ti is a sufficient RIE mask. The RIE parameters for oxygen were similar to those for CCl_2F_2: 600 volt DC bias, 10mTorr pressure, and power density of 0.25 watts/cm^2. The etch rate of the polyimide is about 148nm/minute. One must exercise care to etch the polyimide completely down to the plating base, but at the same time avoid over etching since the 15nm gold layer will quickly sputter away. An SEM micrograph of the x-ray mask at this step of the process is shown in Fig. 4.2. After the polyimide is etched down to the plating base, gold is electroplated into the polyimide mold to form the absorber pattern. The electroplating bath, a commercially available solution [30], is maintained at 45C during the plating process. The stress of the gold film is a function of the plating bath temperature. Low stress films are obtained with bath temperatures of between 35C and 45C. The sample is periodically removed from the bath and the height difference between the polyimide mold and a monitor region is measured with a surface profilometer (Tencor) to determine the

Figure 4.2: SEM micrograph of x-ray mask after CCl_2F_2 and O_2 RIE and just before gold electroplating.

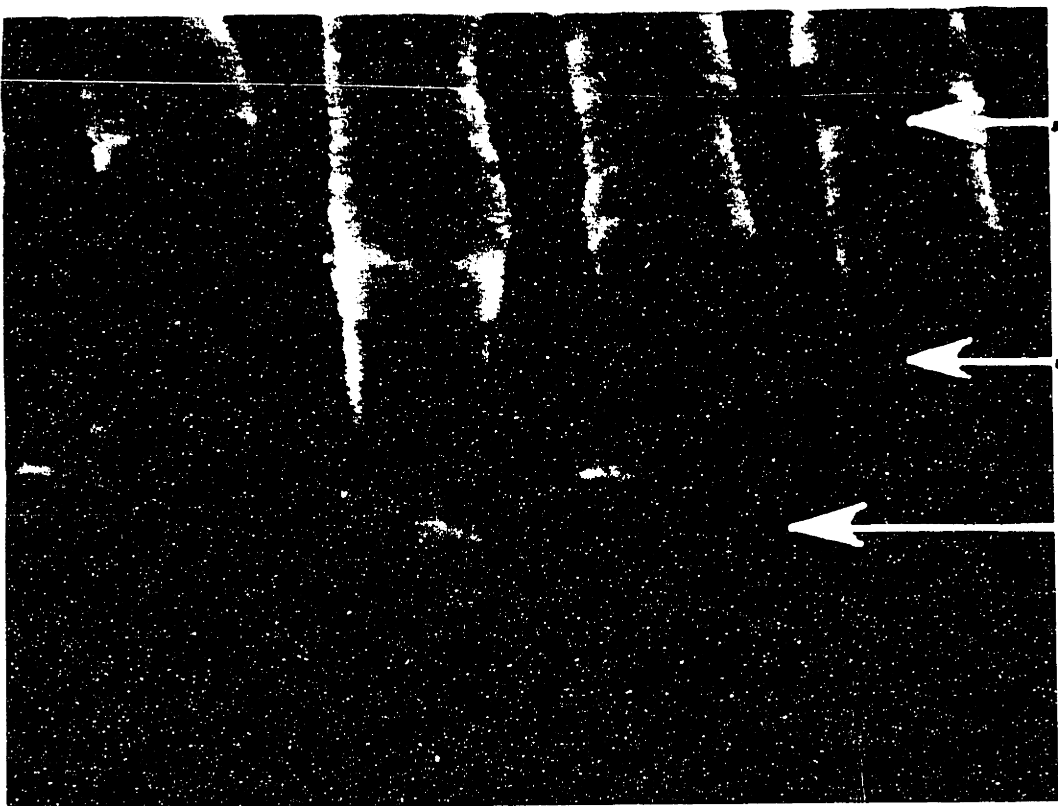

Tri-level resist structure

amount of plated gold. The plating is stopped after the thickness of the gold has reached between 100 and 120nm, a thickness which provides sufficient contrast for x-ray nanolithography.

Next, the central part of the silicon substrate is etched from the back using a mixture of 97% HF and 3% HNO_3, producing a polyimide membrane. A plastic (vespel) mounting ring is bonded to the membrane with a low viscosity, 24-hour epoxy and allowed to cure for two days. The plastic ring is cut free from the Si substrate and 30nm of aluminum evaporated on the back side. The Al is used for electrostatic clamping of the mask to the substrate.

4.3 Experimental Results

Several different patterns have been written using e-beam lithography and made into high contrast x-ray masks. For electron device research applications two patterns were written: one consisting of interdigitated fingers connected to pads, the other a narrow line with a small gap is connected to two pads. Figure 4.3 and Fig. 4.4 show SEM micrographs of the interdigitated finger pattern while Fig. 4.5 and Fig. 4.6 show the line-with-gap pattern, both replicated in 300nm of PMMA by x-ray nanolithography.

A right angle chevron pattern was written to help evaluate lithographic performance. SEM micrographs of this sub-100nm-linewidth pattern are shown in Fig. 4.7 and Fig. 4.8.

A 100nm-period grating with a nominal 50nm linewidth, is shown in Fig. 4.9. These 100nm-period gratings are of great interest for x-ray spectroscopy and quantum-effect device applications. For x-ray spectroscopy, the fine linewidth pattern must be exposed over large areas (10's of mm^2) to be useful which is not feasible by electron beam lithography.

4.4 Conclusion

A process for fabricating high-contrast x-ray-nanolithography masks has been developed to combine the high resolution, arbitrary-pattern-generation capability of scanning-electron-beam lithography with the parallel replication technique of x-ray nanolithography. A procedure for designing the

Figure 4.3: SEM micrograph of interdigitated fingers connected to pads replicated in 300nm of PMMA by x-ray nanolithography.

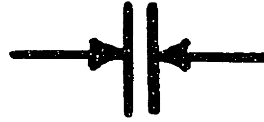

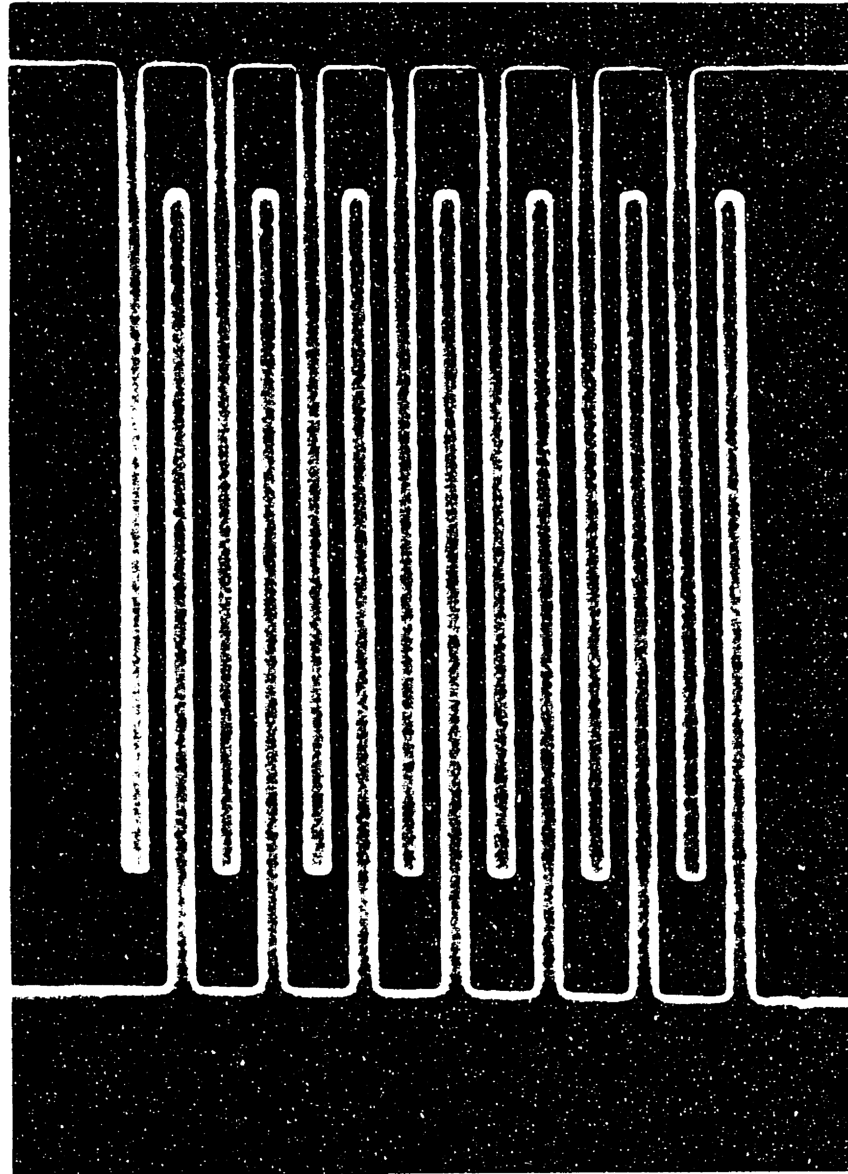

X-Ray Lithography using
E-Beam Generated Mask

Figure 4.4: Another SEM micrograph of interdigitated fingers connected to pads replicated in 300nm of PMMA by x-ray nanolithography.

X-Ray Lithography using
E-Beam Generated Mask

Figure 4.5: SEM micrograph of a narrow line with gap pattern replicated in 300nm of PMMA by x-ray nanolithography.

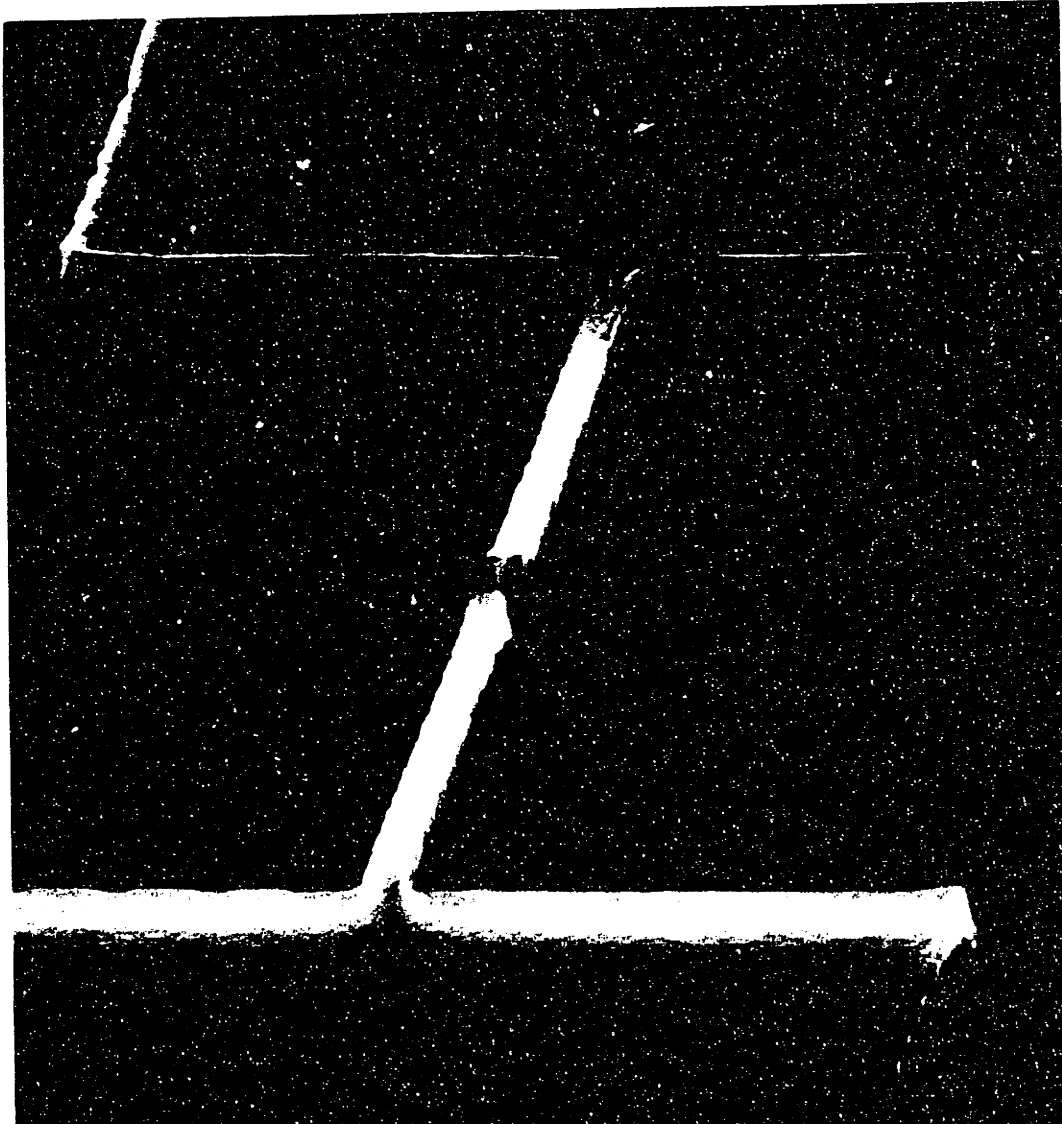

X-Ray Lithography using E-Beam Generated Mask

Figure 4.6: Another SEM micrograph of a narrow line with gap pattern replicated in 300nm of PMMA by x-ray nanolithography.

X-Ray Lithography using
E-Beam Generated Mask

Figure 4.7: SEM micrograph of 85nm linewidth chevron structure with a pitch of 200nm replicated in 300nm of PMMA using x-ray nanolithography.

1.0μm

X-Ray Lithography using
E-Beam Generated Mask

Figure 4.8: Another SEM micrograph of 85nm linewidth chevron structure with a pitch of 200nm replicated in 300nm thick PMMA using x-ray nanolithography.

85nm

X-Ray Lithography using E-Beam Generated Mask

Figure 4.9: SEM micrograph of 100nm-period grating (50nm nominal linewidth) replicated by x-ray nanolithography in 80nm of PMMA.

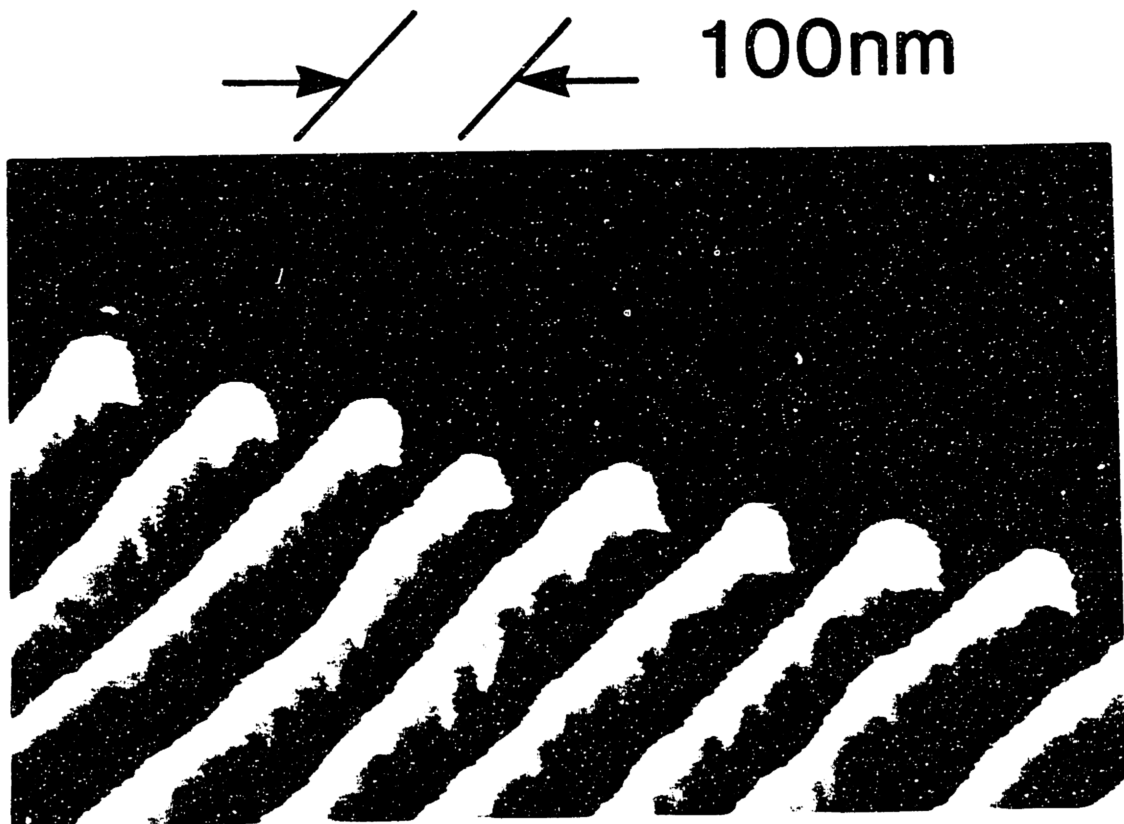

X-ray exposed 100nm period grating in PMMA

patterns at MIT and transferring these data sets to IBM, where the electron beam patterns are written, has been worked out. A working process for transferring the pattern from a thin layer of PMMA into a thick electroplated gold structure for suitable for x-ray nanolithography masks has been developed. This process uses a tri-level resist structure and gold electroplating to produce sufficient absorber thickness at fine linewidths to make a high contrast mask. Patterns for electron device research with linewidths $\approx$ 100nm, and a grating pattern with a nominal 50nm linewidth (100nm period) have been replicated by x-ray nanolithography. The combination of electron-beam lithography and x-ray nanolithography gives researchers the best of both technologies, providing additional flexibility to nanostructure research.

Chapter 5

Alignment of X-ray Gratings

A high resolution alignment technique that utilizes the partial polarization property of fine period transmission gratings has been developed. It is especially useful when the grating period is sufficiently small such that there are no visible diffracted orders. This technique uses a photoelastic modulator (PEM) to produce an intensity signal that is proportional to the sine of twice the angle between the grating lines and the PEM crystal axis. The experimentally demonstrated resolution of this technique on 200nm period gold transmission gratings is better than 1 arc-second. This technique was developed to align x-ray transmission gratings for spectroscopy and interferometry applications.

5.1 Introduction

This chapter follows the paper "Transmission X-Ray Diffraction Grating Alignment Using a Photoelastic Modulator" recently accepted for publication in *Applied Optics* with my coauthors Alan M. Levine and Mark Schattenburg [31]. For applications such as x-ray spectroscopy and interferometry, the grating period is made much smaller than the wavelength of visible light. For example, 200nm period transmission gratings are currently being used in x-ray spectrometers [32], will be used as dispersion elements on the Advanced X-ray Astrophysics Facility (AXAF) satellite for x-ray astronomy to be launched in the 1990's [33], and will be incorporated into a soft x-ray interferometer now under construction [34]. For each of these applications the grating lines must be oriented to other components of the

system within a very small angular tolerance. However, because of the fine period, the grating does not diffract visible light and therefore standard optical techniques such as using an autocollimator to measure a diffracted beam are more difficult or impossible to use.

A sensitive technique to orient a fine period grating using its partial polarization property has been demonstrated. The technique uses a photoelastic modulator (PEM) to modulate the polarization state of a visible light beam and produces a signal proportional to the sine of twice the angle between the grating lines and the axis of the PEM. By using a lock-in amplifier to measure this signal, a very high resolution alignment system can be built. The experimentally determined resolution for 200nm period gold transmission gratings has been found to be less than 1 arc-second, and straightforward modifications should result in even better resolution.

This technique incorporates a modification of the alignment polarimeter [35]. The present work differs in the use of the photoelastic modulator in place of other types of polarization modulators and describes the application of high resolution polarimetry to transmission diffraction grating alignment.

5.2 Alignment Using the Partial Polarization of a Grating.

Fine period gratings, where the period is comparable to or smaller than the wavelength of the incident radiation, act as partial polarizers. For transmission gratings the linear polarization component of the radiation with the electric field vector perpendicular to the grating lines is usually transmitted with less attenuation or reflection than the component with the electric field parallel to the grating lines. This property of a grating can be characterized by $|\alpha_{TM}| > |\alpha_{TE}|$, where the two complex numbers α_{TE} and α_{TM} are the transmission amplitudes for an electric field vector parallel and perpendicular to the grating lines, respectively.

This property can be used directly to align a fine period grating to an axis of a reference linear polarizer. If the light incident on the grating has an intensity, I_{in}, polarized in the y direction, and the grating is oriented with the lines at an angle θ with respect to the y axis, then the intensity

of the transmitted light is given by

$$I_{out} = I_{in}\left(|\alpha_{TE}|^2 \cos^2\theta + |\alpha_{TM}|^2 \sin^2\theta\right). \tag{5.1}$$

To align the grating it is rotated until the transmitted intensity is either minimized or maximized. Near an extremum the transmitted intensity varies as $\delta\theta^2$. Thus to align the grating to 1 μradian the transmitted intensity must be measured with an accuracy of about one part in 10^{12} of the maximum possible transmitted intensity. Since there will always be noise from the photodetector and amplifier this technique is impractical for high resolution alignment.

To overcome these limitations, the following technique produces a signal that is *first order* in θ. In this technique the polarization of the light source is modulated using a PEM [36]. A PEM is basically a vibrating optical element whose strain-induced birefringence enables it to act as a time-varying "retardation plate."

Consider a monochromatic plane wave of light linearly polarized at 45 degrees to the axes of the strain field of the PEM's optical element (see Figure 5.1). The electric field of this wave has the form

$$\mathbf{E} = \frac{E_0}{\sqrt{2}}(\mathbf{x}+\mathbf{y}), \tag{5.2}$$

where the usual time dependence, $e^{i\omega_0 t}$, and spatial dependence, $e^{-ik_0 z}$, have been suppressed, and where $\mathbf{x}$ and $\mathbf{y}$ are unit vectors representing the orthogonal strain-field axes. The electric field of the wave transmitted by the PEM and incident on the grating has the form

$$\mathbf{E} = \frac{E_0}{\sqrt{2}}\left(\mathbf{x}+\mathbf{y}e^{i\phi(t)}\right), \tag{5.3}$$

where $\phi(t)$ is the periodically varying retardation phase. The electric field of the wave, after passing through a grating with its lines oriented at an angle θ with respect to the y axis, is given by

$$\mathbf{E}_{out} = \alpha_{TE}(\mathbf{E}\cdot\mathbf{u})\mathbf{u} + \alpha_{TM}(\mathbf{E}\cdot\mathbf{v})\mathbf{v}, \tag{5.4}$$

where $\mathbf{u}$ and $\mathbf{v}$ are the orthogonal unit vectors parallel and perpendicular to the grating lines given by

$$\mathbf{v} = \mathbf{x}\cos\theta + \mathbf{y}\sin\theta \tag{5.5}$$

$$\mathbf{u} = -\mathbf{x}\sin\theta + \mathbf{y}\cos\theta. \tag{5.6}$$

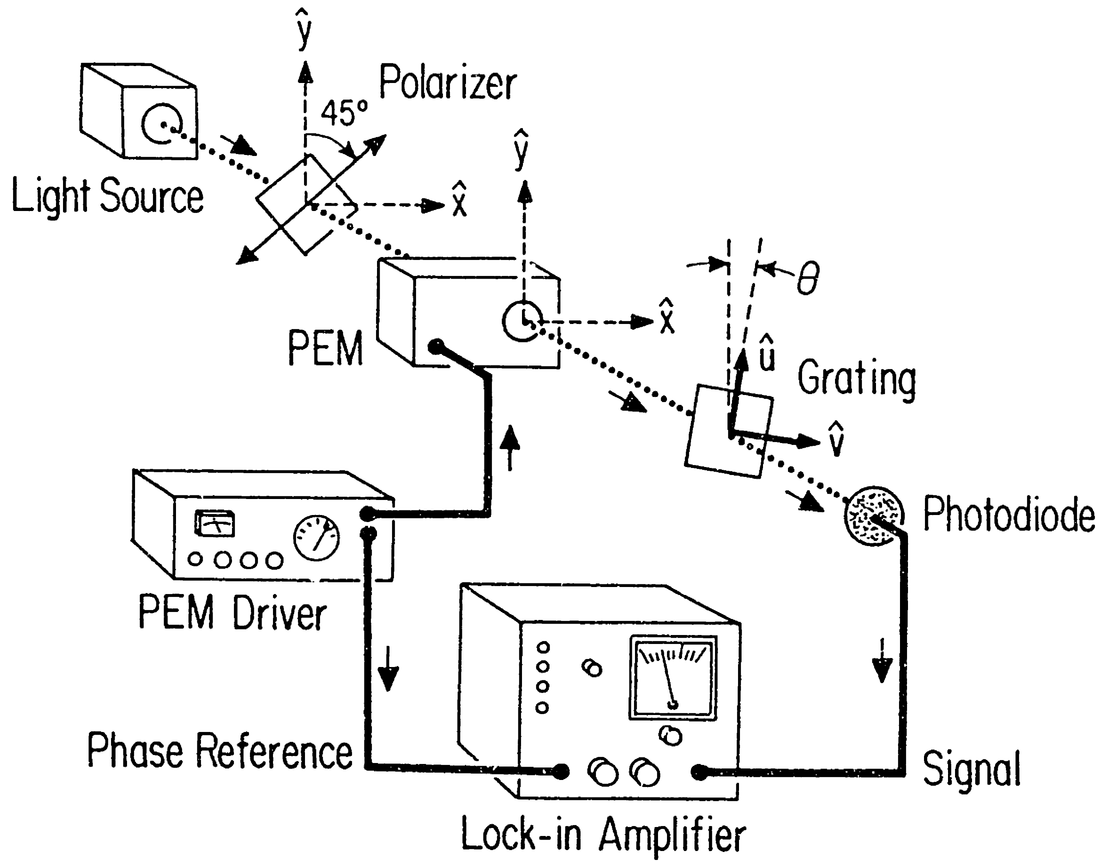

Figure 5.1: Unpolarized light from a lamp is polarized at 45 degrees to the axis of the PEM. In the PEM a bar of fused silica is periodically stressed which produces a time variable "retardation plate". The grating acts as a partial polarizer and the modulated signal is measured with a photodiode detector.

The time averaged intensity of the wave incident on the photodetector is given by

$$\frac{I}{\frac{1}{2}\sqrt{\frac{\mu_0}{\epsilon_0}}|E_0|^2} = \frac{|\alpha_{TM}|^2 + |\alpha_{TE}|^2}{2} + \left(\frac{|\alpha_{TM}|^2 - |\alpha_{TE}|^2}{2}\right) \sin 2\theta \ \cos\phi(t). \quad (5.7)$$

The retardation phase, $\phi(t)$, is approximately given by

$$\phi(t) = \Phi_0 \sin(\omega_m t), \quad (5.8)$$

where Φ_0 is an adjustable retardation amplitude and $\omega_m/2\pi$ is the vibration frequency of the optical element of the PEM. The time dependent term in equation 5.7 can be expanded in a Fourier series in which the coefficients are Bessel functions [37]:

$$\cos[\Phi_0 \sin(\omega_m t)] = J_0(\Phi_0) + 2J_2(\Phi_0)\cos(2\omega_m t) + 2J_4(\Phi_0)\cos(4\omega_m t) + \cdots . \quad (5.9)$$

Using this expression, the second harmonic component of the intensity is

$$\frac{I(2\omega_m)}{\frac{1}{2}\sqrt{\frac{\mu_0}{\epsilon_0}}|E_0|^2} = 2J_2(\Phi_0)\left(\frac{|\alpha_{TM}|^2 - |\alpha_{TE}|^2}{2}\right) \sin 2\theta \ \cos 2\omega_m t. \quad (5.10)$$

$J_2(\Phi_0)$ is maximized for $\Phi_0 \approx \pi$ (half-wave retardation). By measuring the strength of the second harmonic signal the orientation of the grating can be determined. Furthermore, to align the grating so that $\theta = 0$ the grating is rotated so as to reduce the amplitude of the second harmonic component to zero.

There are several points to be noted. The signal component, modulated at a frequency of $2\omega_m$, is proportional to the sine of twice the angle between the PEM axis and the grating lines. Therefore the signal is *first order* in θ for small angles. This is essential for high-resolution alignment. Further, the grating does not need to be a very effective polarizer since the signal amplitude depends only on the difference $|\alpha_{TM}|^2 - |\alpha_{TE}|^2$. Although this analysis assumes a monochromatic light source, similar results are obtained with a broadband source. The amplitude of the signal component is somewhat reduced for a broadband light source because the retardation amplitude, Φ_0, is a function of the wavelength of the light [36]. Also, the analysis assumes that the light incident on the PEM optical element is polarized at exactly 45 degrees to the strain field axis. A more detailed analysis shows that the above results are not sensitive to this angle.

5.3 System Resolution

The resolution of this system is ultimately limited by the Poisson statistics of the photons collected at the detector. Although the conclusions are essentially the same for any type of photodetector, the photon statistics are assumed to manifest themselves in the form of shot noise, where each photon absorbed produces a discrete current pulse. In the case of a photodiode detector, in which a photon produces an electron-hole pair, the time integral of this current pulse is just the charge of the electron. In this case, the variance due to shot noise of the current is simply related to the magnitude of the current [38] by

$$(\Delta i_{RMS})^2 = 2ei_{DC}B, \tag{5.11}$$

where $(\Delta i_{RMS})^2$ is the variance of the current signal, e is the charge on an electron, i_{DC} is the average current through the diode, and B is the bandwidth of the detection system.

The root-mean-square uncertainty in the measured angle due to the statistical fluctuations in current is then

$$\Delta\theta_{RMS} = \left(\frac{di(2\omega_m)}{d\theta}\right)^{-1}_{\theta=0} \frac{\Delta i_{RMS}}{\sqrt{2}}, \tag{5.12}$$

where $di(2\omega_m)/d\theta$ is the derivative of the amplitude of the second-harmonic component of the current with respect to θ evaluated at $\theta = 0$ and the factor of $1/\sqrt{2}$ is included since the phase of the signal is known (see eqn. 5.10). If I_0 is the power of a narrow spectral-band beam of light incident on the grating, $h\nu$ is the average photon energy, and η is the quantum efficiency of the photodiode detector, equations 5.7 and 5.10 give

$$i_{DC} = \left(\frac{|\alpha_{TM}|^2 + |\alpha_{TE}|^2}{2}\right)\frac{e\eta}{h\nu}I_0 \tag{5.13}$$

$$\left(\frac{di(2\omega_m)}{d\theta}\right)_{\theta=0} = 4J_2(\Phi_0)\left(\frac{|\alpha_{TM}|^2 - |\alpha_{TE}|^2}{2}\right)\frac{e\eta}{h\nu}I_0\,. \tag{5.14}$$

Let us define the parameter β as

$$\beta = \frac{1}{i_{DC}}\left(\frac{di(2\omega_m)}{d\theta}\right)_{\theta=0} \tag{5.15}$$

$$= 4J_2(\Phi_0)\left(\frac{|\alpha_{TM}|^2 - |\alpha_{TE}|^2}{|\alpha_{TM}|^2 + |\alpha_{TE}|^2}\right)\,. \tag{5.16}$$

For $\Phi_0 \approx \pi$, $J_2(\Phi_0) \sim 0.5$. Therefore,

$$\beta \approx 2\left(\frac{|\alpha_{TM}|^2 - |\alpha_{TE}|^2}{|\alpha_{TM}|^2 + |\alpha_{TE}|^2}\right) . \tag{5.17}$$

Combining the above equations to obtain

$$\Delta\theta_{RMS} = \frac{1}{\beta}\sqrt{\frac{eB}{i_{DC}}}. \tag{5.18}$$

It is quite easy to reduce $\Delta\theta_{RMS}$ to a very small value. For example, if $B = 1$ Hz, $I_0 = 10^{-3}$ watts, $h\nu = 3.0 \times 10^{-19}$ joules, $\eta = 0.8$, $|\alpha_{TM}|^2 = 0.03$ and $|\alpha_{TE}|^2 = 0.001$ then $\Delta\theta_{RMS} = 0.1$ μradian.

5.4 Experimental Results

An apparatus was constructed to demonstrate this alignment technique for alignment of x-ray interferometer gratings and future use in aligning a large ($\approx$ 250) array of 200nm period gratings which will form the High Energy Transmission Grating for the Advanced X-Ray Astrophysics Facility satellite [33]. The configuration is shown in Figure 5.1.

A steady, quiet light source is needed to produce a strong signal. An excellent light source for this experiment was a small, (50 watt), tungsten-halogen lamp powered by a DC supply. The spectral band was limited to roughly $\pm$100nm around 680nm with an infrared blocking filter (3mm thick Schott KG-3 glass [39]). The light is collimated by a 200mm focal length 50mm diameter lens and is linearly polarized at 45 degrees to the strain axes of the PEM by dichroic plastic (Polaroid$^{\text{TM}}$) sheet. The photoelastic modulator consists of a fused silica bar that is stressed by a crystalline quartz piezoelectric driver at a frequency of 50kHz [40]. The amplitude of the vibration of the fused silica bar is adjusted to give half-wave retardation at a wavelength of 680nm, which is near the center of the filter passband and is in the region in which the photodiode detector is highly sensitive.

The modulated light beam then passes through the grating under test. This grating has a period of 200nm, is made of gold electroplated to a thickness of $\approx$ 1 μm, and is supported on a 1 μm thick polyimide film. Figure 5.2 shows a SEM micrograph cross-section of this x-ray grating. The light intensity is converted to an electrical signal by a silicon photodiode

Figure 5.2: SEM micrograph of a 200nm period x-ray transmission grating with Au lines electroplated to about 1μm and supported on a 1μm polyimide membrane.

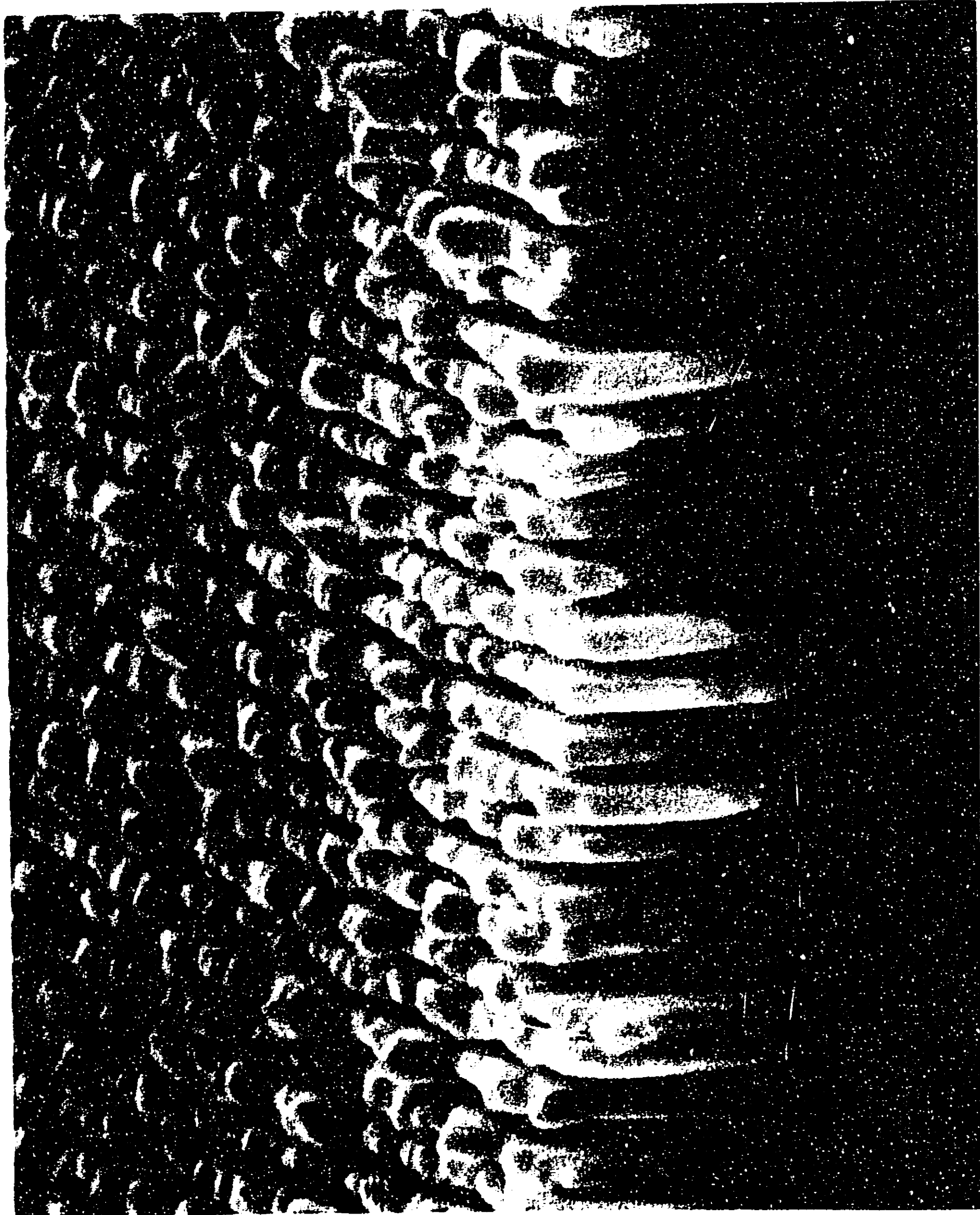
1.0 μm

and displayed on an oscilloscope. The amplitude of the in-phase 100kHz component is measured with a lock-in amplifier.

To measure small changes in the grating rotation angle, θ, a mirror was mounted on the grating holder so that its normal was perpendicular to the optical axis. A 50mm diameter, $\approx$ 1 arc-second resolution autocollimator [41] was used to measure the small changes in the tilt of the mirror and therefore the rotation angle of the grating.

A series of measurements were made to determine the repeatability of this technique, which is an upper bound of the resolution. The orientation of the grating was first adjusted to null the amplitude of the 100kHz signal measured using the lock-in amplifier. Then, a number of measurements were made in which the grating was first rotated through a large angle ($> 90^o$) and then back to close to its original position. For each of these measurements, the signal on the lock-in amplifier was again nulled by careful adjustment of a micrometer which could rotate the grating within a limited range, and the angular orientation of the grating was measured using the autocollimator. The standard deviation of a set of grating rotation angles resulting from these measurements is an estimate of the repeatability of this technique.

After removing several sources of mechanical drift, stable and repeatable measurements were obtained. The PEM itself was found to have a long warm-up period in which there was significant drift, perhaps due to thermal changes in the mounting of the optical element. However, after about an hour of warm up, the drift was well below the limits which detectable using the autocollimator. The standard deviation of a set of ten measurements was 0.6 arc-seconds or $\approx 3\ \mu$rad.

The measured peak-to-peak photodiode signal amplitude, with $\theta = \pi/4$, with this development AXAF grating as a sample was 15 μamp and the DC current level was about 20 μamp. (The DC current contained a dark current contribution of $\sim$ 10 μamp.) Using these numbers and a lock-in amplifier integration time of 1 second (i.e., B = 1 Hz) give

$$\Delta i_{RMS} = \sqrt{2 e i_{DC} B} \tag{5.19}$$

$$= 3\ p\text{amp} \tag{5.20}$$

and

$$\left(\frac{di(2\omega_m)}{d\theta}\right)_{\theta=0} = 30\ \mu\text{amp rad}^{-1}. \tag{5.21}$$

Therefore the shot noise limited resolution from equation 12 is

$$\Delta\theta \;=\; 0.07\,\mu\text{rad}\,. \tag{5.22}$$

The measurement of the resolution by this experimental set up was limited to about 1 arc-second by our ability to adjust the grating orientation, the accuracy of the autocollimator, and possibly, other mechanical effects. The angular resolution of the experiment was apparently not yet shot noise limited.

5.5 Conclusion

A very sensitive technique has been developed to align fine period diffraction gratings where standard techniques, using visible light, cannot be used. This technique takes advantage of the partial polarization property of gratings and will work even when the partial polarization is weak. The signal, measured with a lock-in amplifier, is proportional to the sine of twice the angle between the grating lines and the PEM axis as well as the difference between the transmission of light polarized normal and perpendicular to the grating lines. The repeatability statistics show a resolution better than 1 arc-second for the experimental system using a development AXAF x-ray transmission grating. The high inherent resolution of this technique suggests that it may be useful in other new applications.

Chapter 6

Electromagnetic Grating Theory and Calculations

6.1 Introduction

The analysis of diffraction by gratings has a long and rich history. Since 1930 there have been over 400 technical papers on the subject of grating diffraction [42]. There are a large number of methods utilizing different sets of assumptions to solve the diffraction problem in periodic structures. With the development of computer technology it has been possible to use sophisticated numerical methods to solve Maxwell's equations in periodic grating structures in a rigorous fashion. There are two basic approaches to this problem, the coupled-wave approach [43]-[48] and the modal approach [49]-[56]. The modal method is also know as the eigenmode, characteristic-mode, Floquet, Floquet-Bloch, and (confusingly) the coupled-mode approach a name also given to the coupled-wave technique. Both approaches can be used to solve Maxwell's equations in periodic structures and the equivalence of the two techniques in a full rigorous formulation has been demonstrated [57]. A review of these two theories is given in [58].

The technique that has been implemented in this work uses the coupled-mode approach and makes the assumption that the grating consists of a "square wave" (lamellar) structure. This assumption limits the shape of gratings that can be analyzed. However, almost all the very fine-period gratings made in our laboratory have essentially a square wave profile. Also, more general structures can be constructed from many layers of square

wave gratings. The assumption that the grating consists of a rectangular profile greatly simplifies the electromagnetic equations and the technique of separation of variables can be used. A detailed look at the theory and computation methods are given in the next section and an overview is given below.

There are two different techniques that can be used to find the coupled-mode eigenvalues for a square wave structure. The first technique, used by Burckhardt [52] for sinusoidally modulated gratings, extended by Kaspar [54] to include nonsinusoidal and complex refractive index modulations, and used by Knop [53] to study deep rectangular groove gratings for storing color pictorial information, involves expressing the field quantities inside the grating and the position dependent index of refraction in terms of a Fourier series. When the terms are substituted into the general wave equation an infinite set of coupled linear equations results. When this set of equations is truncated the resulting problem is then an ordinary matrix eigenvalue problem. The other approach has been extensively studied by Botten et al. [59], [60], [61] as well as Tayeb and Petit [62]. This approach makes use of the fact that inside each region of different refractive index the solutions are simple, consisting of linear combinations of the functions $\sin\beta x$, $\cos\beta x$ in one region and $\sin\Gamma x$, $\cos\Gamma x$ in the other. The complex coefficients β and Γ are simply related to the grating parameters and the grating eigenvalue. An algebraic equation is derived from the boundary conditions and the pseudo-periodicity requirement. The roots of this transcendental equation are the required eigenvalues. There is an interesting analogy between this electromagnetics eigenvalue problem and quantum mechanics problems. In quantum mechanics the matrix method corresponds, of course, to matrix mechanics where the possible solutions are represented as vectors in a Hilbert space of ortho-normal functions. For the grating problem, the ortho-normal functions are the complex exponentials of the Fourier expansion. In quantum mechanics, the operators are represented as matrices and are very often truncated to finite size for actual computation. The eigenvalues and eigenvectors are determined from the matrix equation by numerical routines, although real observables have Hermitian matrices which are easier to process than the general complex matrix that the electromagnetic grating problem has. The algebraic method is analogous to the solution of a quantum mechanics problem by solving the Schrodinger wave equation. The algebraic eigenvalue equation results from solving the

grating differential equation, and then applying the boundary conditions to derive a constraint on the eigenvalue. This is very similar to the procedure needed to solve the Schrodinger wave equation.

An approach that combines these two techniques has been implemented and found to provide accurate results in every instance where other published calculations are available for checking. Further, the calculations have been checked in a number of limiting cases and found to be correct. The idea is to combine the best parts of both the matrix and transcendental equation methods. This approach is conceptually simple and algorithmically safe, but consumes considerable CPU resources for each grating solution. The first step is to set up the coupled-mode equations in matrix form. When the index of refraction is real, the resulting matrix is both real and symmetric. However, when the grating material is lossy (i.e. ϵ has an imaginary part) the matrix elements become complex while maintaining the symmetry of the matrix. A symmetric matrix with complex coefficients is not Hermitian. Therefore, the special routines that work so well with Hermitian matrices cannot be used and a general complex eigenvalue routine is needed. Fortunately, the "EISPACK" public-domain software is available to solve this problem [63]. The eigenvalues and eigenvectors of the matrix are determined using the EISPACK routines. Because the eigenvalue matrix is a truncation of the infinite set of equations, the matrix eigenvalues will be slightly different from the true grating eigenvalues. Because the matrix eigenvalues, derived from the EISPACK routines, are usually within a few percent of the grating eigenvalues they are used as the starting point for numerically finding the roots of the algebraic eigenvalue equation. Newton's method, is notoriously bad at searching for a root but rapidly converges when near the root [64]. Newton's method is used to find the exact algebraic eigenvalues since the matrix eigenvalues are generally very close to the real eigenvalues and the derivative of the transcendental equation can be calculated analytically. Care must be taken to properly normalize the eigenvalue equation and keep track of the previously found eigenvalues so that the same eigenvalue is not found more than once. After all the eigenvalues are determined, the boundary conditions of continuous tangential electric and magnetic fields are imposed at the front and back boundaries of the grating. These boundary conditions impose constraints that result in a large set of linear equations. These equations can become ill-conditioned for deep gratings if solved in a routine manner. The rea-

son for this is that the boundary condition matrix contains terms, some of which grow exponentially with depth and others that decay exponentially. A linear equation routine (i.e. Gaussian elimination) does not know what terms are significant and which are not. However, with proper care and normalization the boundary condition equations can be written in a stable and well conditioned form, independent of the grating depth. These linear equations are solved using a modification of the public domain LINPACK routines [65], essentially Gaussian elimination with partial pivoting for "LU" factorization followed by back substitution. After the boundary condition equations are solved the electric and magnetic fields are known everywhere, inside the grating as well as outside. The diffracted intensities are calculated and stored in an output file.

The matrix method is simple and reliable. The "hard" part of this technique is finding the eigenvalues of a general complex matrix, a problem that has been solved through years of effort by others. Unfortunately, for square wave grating profiles the dielectric constant as a function of position is discontinuous and the Fourier series of this function converges very slowly, particularly near the discontinuity. Under some circumstances, when the period is comparable to the wavelength and the modulus of the dielectric constant is large, the error in the matrix determined eigenvalues is large enough to effect the accuracy of the calculated diffraction intensities, especially for deep gratings. On the other hand, the roots of the transcendental equation give the exact eigenvalues, to 12 or more significant figures, but these roots reside in a large region of the two dimensional complex plane. Searching for these roots can be a CPU consuming process. Both Botten et al [61] and Tayeb and Petit [62] have found clever methods to search for the roots that take advantage of the fact that the transcendental equation is analytic. Both of these methods are more complicated than the matrix technique and may in fact consume more CPU cycles. Therefore the combination of the matrix method and the transcendental equation method complement each other very well. The matrix calculation does the "searching" and the transcendental equation is used to "polish" the eigenvalues. In each instance where comparisons can be made, the results of this combination have been both reliable and accurate. The details of the equations and calculations follow in the next section.

6.2 Basic Equations

For the electromagnetic theory of gratings, as well as everything else, the starting point is Maxwell's equations. The sinusoidal steady state, with time dependence $e^{i\omega t}$ is assumed. Further, the dielectric function, ϵ, is assumed to be a smooth function. Maxwell's equations are:

$$\nabla \cdot \epsilon \mathbf{E} = 0 \tag{6.1}$$

$$\nabla \cdot \mu_0 \mathbf{H} = 0 \tag{6.2}$$

$$\nabla \times \mathbf{H} = -i\omega\epsilon \mathbf{E} \tag{6.3}$$

$$\nabla \times \mathbf{E} = i\omega\mu_0 \mathbf{H} \tag{6.4}$$

Suppose that the grating is oriented with respect to the coordinate system so that the lines run parallel to the x_2 axis and the grating plane is normal to the x_3 axis. This geometry is shown in fig. 6.1.

First, consider the TE case where the electric field is in the x_2 direction, parallel to the grating lines. The electric field is given by:

$$\mathbf{E} = E_2(x_1, x_3)\hat{\mathbf{x}}_2. \tag{6.5}$$

Taking the curl of this gives:

$$\nabla \times \mathbf{E} = \frac{\partial E_2}{\partial x_1}\hat{\mathbf{x}}_3 - \frac{\partial E_2}{\partial x_3}\hat{\mathbf{x}}_1 \tag{6.6}$$

From Faraday's equation, $\mathbf{E}$ and $\mathbf{H}$ are related by:

$$\mathbf{H} = \frac{1}{i\omega\mu_0}\left(\frac{\partial E_2}{\partial x_1}\hat{\mathbf{x}}_3 - \frac{\partial E_2}{\partial x_3}\hat{\mathbf{x}}_1\right) \tag{6.7}$$

Taking the curl of $\mathbf{H}$ gives

$$\begin{aligned} -i\omega\epsilon\mathbf{E} &= \nabla \times \mathbf{H} \\ &= -\frac{1}{i\omega\mu_0}\left(\frac{\partial^2 E_2}{\partial x_1^2} + \frac{\partial^2 E_2}{\partial x_3^2}\right). \end{aligned} \tag{6.8}$$

Therefore the master equation to solve for the TE polarization case is:

$$\frac{\partial^2 E_2}{\partial x_1^2} + \frac{\partial^2 E_2}{\partial x_3^2} + \omega^2\mu_0\epsilon(x_1, x_3)E_2 = 0. \tag{6.9}$$

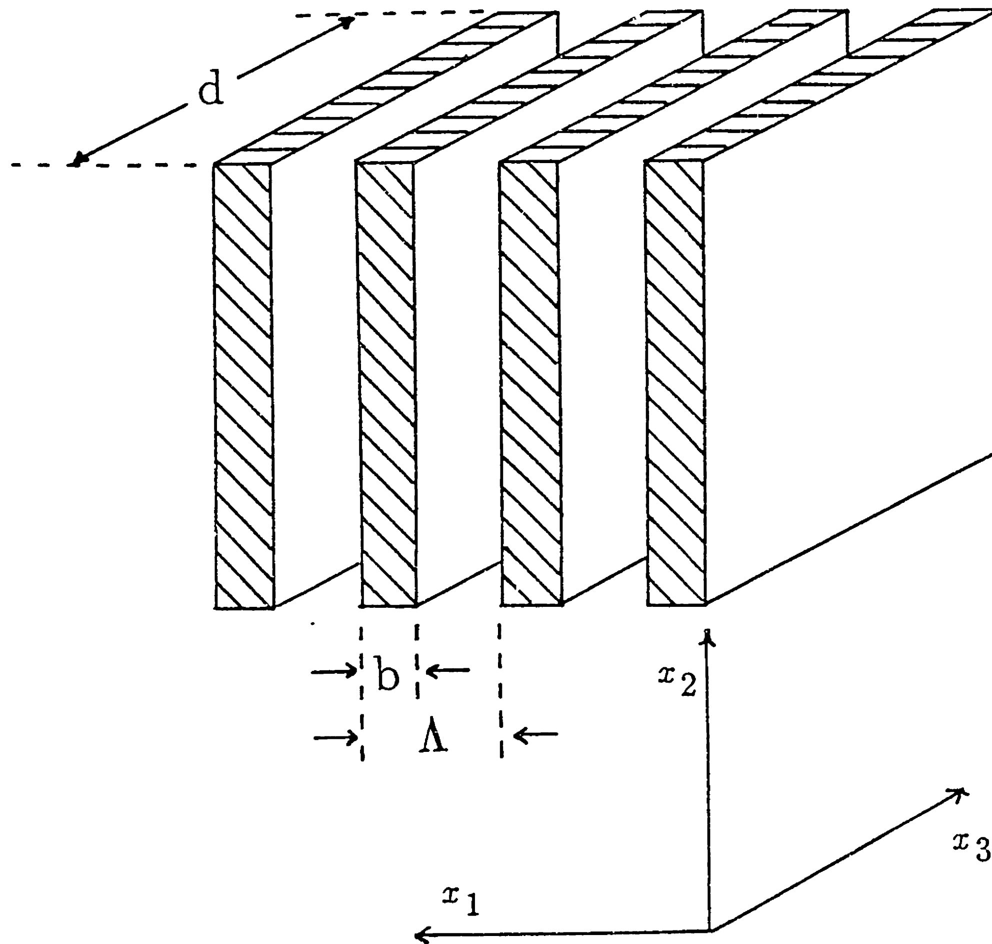

Figure 6.1: This shows the orientation of the grating with respect to the coordinate system. The grating lines run parallel to the x_2 axis and the normal of the grating is parallel to the x_3 axis. Inside the grating the dielectric constant is a function of x_1 and outside the grating it is a constant, perhaps a different constant in front than in back of the grating.

Once this equation is solved for E_2 the complete fields are given by:

$$\mathbf{E} = E_2 \hat{\mathbf{x}}_2 \tag{6.10}$$

$$\mathbf{H} = \frac{1}{i\omega\mu_0}\left(\frac{\partial E_2}{\partial x_1}\hat{\mathbf{x}}_3 - \frac{\partial E_2}{\partial x_3}\hat{\mathbf{x}}_1\right) \tag{6.11}$$

When the **H** field is parallel to the grating lines, TM case, the general wave equation is similar but not quite the same. In this case

$$\mathbf{H} = H_2 \hat{\mathbf{x}}_2 \tag{6.12}$$

from which **E** is found to be

$$\mathbf{E} = \frac{1}{-i\omega\epsilon}\left(\frac{\partial H_2}{\partial x_1}\hat{\mathbf{x}}_3 - \frac{\partial H_2}{\partial x_3}\hat{\mathbf{x}}_1\right) \tag{6.13}$$

Taking the curl of **E** and relating it to **H** gives

$$i\omega\mu_0 H_2 = \left[\frac{\partial}{\partial x_1}\left(\frac{1}{i\omega\epsilon}\frac{\partial H_2}{\partial x_1}\right) + \frac{\partial}{\partial x_3}\left(\frac{1}{i\omega\epsilon}\frac{\partial H_2}{\partial x_3}\right)\right] \tag{6.14}$$

For the TM polarization case the generalized wave equation is

$$\frac{\partial}{\partial x_1}\left(\frac{1}{i\omega^2\mu_0\epsilon}\frac{\partial H_2}{\partial x_1}\right) + \frac{\partial}{\partial x_3}\left(\frac{1}{i\omega^2\mu_0\epsilon}\frac{\partial H_2}{\partial x_3}\right) + H_2 = 0. \tag{6.15}$$

The complete field solution is then given by

$$\mathbf{H} = H_2 \hat{\mathbf{x}}_2 \tag{6.16}$$

$$\mathbf{E} = \frac{1}{-i\omega\epsilon}\left(\frac{\partial H_2}{\partial x_1}\hat{\mathbf{x}}_3 - \frac{\partial H_2}{\partial x_3}\hat{\mathbf{x}}_1\right). \tag{6.17}$$

6.2.1 Solving the Basic Equations with the Matrix method

The partial differential equations for the TE and TM case must now be solved. In each case the mathematical technique of "separation of variables" is used to reduce the *partial* differential equation down to two ordinary differential equations. Because of the assumption that ϵ is constant in the x_3 direction, one of these two differential equations will be easy to solve

and the other will be an eigenvalue problem. First, consider the TE case. The general wave equation for E_2 is

$$\frac{\partial^2 E_2}{\partial x_1^2} + \frac{\partial^2 E_2}{\partial x_3^2} + \omega^2 \mu_0 \epsilon(x_1, x_3) E_2 = 0. \tag{6.18}$$

Assuming that E_2 has the form

$$E_2 = A(x_1) B(x_3) \tag{6.19}$$

and is substituted this into equation 6.18 the result is

$$B\frac{d^2 A}{dx_1^2} + A\frac{d^2 B}{dx_3^2} + \omega^2 \mu_0 \epsilon(x_1) AB = 0. \tag{6.20}$$

Dividing both sides by the product $A(x_1)B(x_3)$ gives

$$\left[\frac{1}{A}\frac{d^2 A}{dx_1^2} + \omega^2 \mu_0 \epsilon(x_1)\right] + \frac{1}{B}\frac{d^2 B}{dx_3^2} = 0. \tag{6.21}$$

This equation can be separated into two parts, one part that depends only on x_1 and the other part that depends only on x_3 therefore these two parts must be equal to a constant which chosen to be γ^2. The first equation, a function of x_3 only, is given by 6.22.

$$\frac{1}{B}\frac{d^2 B}{dx_3^2} = -\gamma^2 \tag{6.22}$$

Where γ^2 is the separation of variables constant. The second equation is then 6.23.

$$\frac{1}{A}\frac{d^2 A}{dx_1^2} + \omega^2 \mu_0 \epsilon(x_1) = \gamma^2 \tag{6.23}$$

The partial differential equation has been reduced to two ordinary differential equations. Further, the first equation, 6.22, is easy to solve. The solution is given by

$$B(x_3) = B_0 e^{i\gamma x_3}. \tag{6.24}$$

The second equation is more difficult but at least it is only an ordinary differential equation; the master equation for the TE case.

$$\frac{d^2 A}{dx_1^2} + (\omega^2 \mu_0 \epsilon(x_1) - \gamma^2) A = 0 \tag{6.25}$$

The function, $A(x_1)$, will be periodic up to a phase factor which is determined by the incident plane wave angle. The function will take the form of

$$A(x_1) = U(x_1)e^{i\Phi x_1} \tag{6.26}$$

where Φ is the x_1 component of the incident wavevector, with angle ϕ with respect to the x_3 axis given by

$$\Phi = \frac{2\pi}{\lambda}\sin\phi \tag{6.27}$$

and $U(x_1)$ is a periodic function with the same period, Λ, as the grating. Since $U(x_1)$ is periodic it can be expanded in a Fourier series, resulting in equations 6.28 and 6.29.

$$A(x_1) = \sum_{n=-\infty}^{\infty} a_n e^{i(n\frac{2\pi}{\Lambda}+\Phi)x_1} \tag{6.28}$$

$$\frac{d^2A}{dx_1^2} = \sum_{n=-\infty}^{\infty} \left(i\frac{2\pi}{\Lambda}n + i\Phi\right)^2 a_n e^{i(n\frac{2\pi}{\Lambda}+\Phi)x_1}. \tag{6.29}$$

Likewise the periodic square wave function $\epsilon(x_1)$ is expanded in a Fourier series,

$$\epsilon(x_1) = \epsilon_0 \sum_{m=-\infty}^{\infty} u_m e^{i\frac{2\pi}{\Lambda}mx_1}, \tag{6.30}$$

and the closed form expression for the coefficients is given by

$$u_0 = \frac{b}{\Lambda}\left(\frac{\epsilon}{\epsilon_0} - \frac{\epsilon^{II}}{\epsilon_0}\right) + \frac{\epsilon^{II}}{\epsilon_0} \tag{6.31}$$

$$u_m = \left(\frac{\epsilon}{\epsilon_0} - \frac{\epsilon^{II}}{\epsilon_0}\right)\frac{1}{m\pi}\sin\left(m\pi\frac{b}{\Lambda}\right)$$

Substituting the Fourier expansion equations 6.28, 6.29, and 6.30 into the master wave equation, 6.25 gives

$$\sum_{n=-\infty}^{\infty} a_n \left(i\frac{2\pi}{\Lambda}n + i\Phi\right)^2 e^{i(\frac{2\pi}{\Lambda}nx+\Phi x)} +$$

$$\left(\omega^2\mu_0\epsilon_0 \sum_{m=-\infty}^{\infty} u_m e^{i\frac{2\pi}{\Lambda}mx} - \gamma^2\right)\left(\sum_{l=-\infty}^{\infty} a_l e^{i(\frac{2\pi}{\Lambda}lx+\Phi x)}\right) = 0. \tag{6.32}$$

Multiplying the above equation by $e^{-i(\frac{2\pi}{\Lambda}kx+\Phi x)}$ and integrating over a period, Λ, gives an infinite set of linear equations in the coefficients.

$$-a_k\left(\frac{2\pi}{\Lambda}k+\Phi\right)^2+\omega^2\mu_0\epsilon_0\sum_{r=-\infty}^{\infty}u_{k-r}a_r=\gamma^2 a_k \tag{6.33}$$

Upon careful inspection, this set of equations is in the form of a matrix eigenvalue problem with the matrix elements given by 6.34.

$$M_{m,n}=\omega^2\mu_0\epsilon_0\left[u_{m-n}-\frac{1}{\omega^2\mu_0\epsilon_0}\left(\frac{2\pi}{\Lambda}n+\Phi\right)^2\delta_{m,n}\right] \tag{6.34}$$

After truncating this set of equations to a finite size, the eigenvalues and eigenvectors can be found with published general matrix eigenvalue routines [63].

$$Ma=\gamma^2 a \tag{6.35}$$

After finding the eigenvalues, γ_i^2, of the matrix M the coefficients multiplying the eigenvectors are found by using the boundary conditions, that both the tangential electric and magnetic fields must be continuous, imposed at the front and back of the grating structure. Details of the boundary condition equations are given latter.

Now, consider the TM case where the master TM equation is given by

$$\frac{\partial}{\partial x_1}\left(\frac{1}{\omega^2\mu_0\epsilon}\frac{\partial H_2}{\partial x_1}\right)+\frac{\partial}{\partial x_3}\left(\frac{1}{\omega^2\mu_0\epsilon}\frac{\partial H_2}{\partial x_3}\right)+H_2=0 \tag{6.36}$$

The same technique of separation of variables is used to reduce this partial differential equation into two ordinary differential equations. As in the TE case, one of the equations will be simple to integrate and the other can be written in the form of a matrix eigenvalue problem. Assume that H is in the form of

$$H_2=A(x_1)B(x_3). \tag{6.37}$$

Substituting equation 6.37 into equation 6.36, and dividing both sides by $A(x_1)B(x_3)$ to get

$$\frac{1}{A}\frac{d}{dx_1}\left(\frac{1}{\omega^2\mu_0\epsilon}\frac{dA}{dx_1}\right)+\frac{1}{\omega^2\mu_0\epsilon}\frac{1}{B}\frac{d^2B}{dx_3^2}+1=0. \tag{6.38}$$

The left hand term depends only on x_1 while the right hand side depends only on x_3 so that this equation separates into two parts. The two equations are as follows:

$$\frac{1}{B}\frac{d^2B}{dx_3^2} = -\gamma^2 \tag{6.39}$$

$$\omega^2\mu_0\epsilon(x_1)\frac{d}{dx_1}\left(\frac{1}{\omega^2\mu_0\epsilon(x_1)}\frac{dA}{dx_1}\right) + (\omega^2\mu_0\epsilon(x_1) - \gamma^2)A = 0. \tag{6.40}$$

The first term on the left hand side of the equation can be expanded to give

$$\omega^2\mu_0\epsilon(x_1)\frac{d}{dx_1}\left(\frac{1}{\omega^2\mu_0\epsilon(x_1)}\frac{dA}{dx_1}\right) = \frac{d^2A}{dx_1^2} - \frac{1}{\epsilon(x_1)}\frac{d\epsilon}{dx_1}\frac{dA}{dx_1} \tag{6.41}$$

In the above equation the first term or the right hand side is also found in the TE polarization case. The second term represents a highly singular function, the derivative of a step function, which forces the proper boundary condition on the TM eigenvectors. The tangential electric and magnetic fields must both be continuous as a consequence of Maxwell's equations. However for the TM polarization, the magnetic field is given by $A(x_1)B(x_3)$, both continuous functions but the electric field is given by

$$\mathbf{E} = \frac{1}{-i\omega\epsilon}\left(\frac{\partial H_2}{\partial x_1}\hat{\mathbf{x}}_3 - \frac{\partial H_2}{\partial x_3}\hat{\mathbf{x}}_1\right) \tag{6.42}$$

Since E_3 must be continuous and there is a step change in the ϵ function it follows that the derivative, $dA(x_1)/dx_1$, must be zero at the points where ϵ jumps. To formulate the TM polarization eigenvalue matrix the TE polarization matrix is added to another matrix which represents the singular function. What this matrix does is to modify the eigenvalues so that the eigenvector representing the field solutions forbidden by the TM boundary conditions has a very large (infinitely large for the untruncated matrix) negative (i.e. attenuated) eigenvalue. In practice the eigenvalues for the TE matrix are much more accurate than the TM case since the convergence of a Fourier series to a *singular* function is very slow. The Fourier coefficients for this singular function are approximated by:

$$\frac{1}{\epsilon(x)}\frac{d\epsilon}{dx} = \frac{1}{\epsilon(x)}(\epsilon - \epsilon^{II})\left[\delta(x+\frac{b}{2}) - \delta(x-\frac{b}{2})\right] \tag{6.43}$$

$$= \frac{1}{\epsilon(x)}(\epsilon - \epsilon^{II}) \sum_m \frac{2i}{\Lambda} \sin(\pi m \frac{b}{\Lambda}) e^{i\frac{2\pi}{\Lambda}mx} \quad (6.44)$$

$$= \frac{2(\epsilon - \epsilon^{II})}{\epsilon + \epsilon^{II}} \sum_m \frac{2i}{\Lambda} \sin(\pi m \frac{b}{\Lambda}) e^{i\frac{2\pi}{\Lambda}mx}. \quad (6.45)$$

To find the eigenvalue matrix for the TM case the dA/dx term is expanded to get

$$\frac{dA}{dx} = \sum_m i\left(\frac{2\pi}{\Lambda}m + \Phi\right) a_m e^{i\frac{2\pi}{\Lambda}mx + i\Phi x}. \quad (6.46)$$

After substituting each of these Fourier expansions into 6.40 the eigenvalue matrix is found to be:

$$M^{TM}_{m,n} = M^{TE}_{m,n} + N_{m,n} \quad (6.47)$$

$$N_{m,n} = \omega^2 \mu_0 \epsilon_0 \left[\frac{(\epsilon - \epsilon^{II})}{(\epsilon + \epsilon^{II})} \frac{2\lambda}{\pi\Lambda} \left(\frac{\lambda}{\Lambda} m + \sin(\phi) \right) \sin(\pi(n-m)\frac{b}{\Lambda}) \right].$$

The resulting eigenvalue problem is then

$$M^{TM} a = \gamma^2 a \quad (6.48)$$

and is numerically solved by the general, complex eigenvalue routine. After solving the eigenvalue problem, the boundary conditions at the edges of the grating, $x_3 = 0$, and $x_3 = d$ are used to find the field amplitudes in almost the identical fashion as for the TE polarization case.

6.2.2 Solving the Boundary Conditions

Solving the boundary condition equations of continuous electric and magnetic tangential fields requires a little insight and a lot of algebra. The idea is to write down the electric and magnetic fields in terms of the unknown Fourier amplitude coefficients outside the grating region, both front and back, and the electric and magnetic fields inside the grating in terms of unknown eigenfunction amplitudes. The condition that both the tangential magnetic and electric fields must be continuous at both interfaces provides enough constraints to solve for the unknown amplitudes. These constraints take the form of coupled linear equations and can be solved by standard linear algebra techniques, although the equations must be properly normalized and formulated so that they are well conditioned. The gory details of this process follow.

Figure 6.2 shows the three regions of the grating and the corresponding wavevectors. For the TE case the tangential H_1 field is given by

$$H_1 = -\frac{1}{i\omega\mu_0}\frac{\partial E_2}{\partial x_3} \tag{6.49}$$

and in the TM case the E_1 field is given by

$$E_1 = \frac{1}{i\omega\epsilon}\frac{\partial H_2}{\partial x_3} \tag{6.50}$$

The difference between these two cases is that in the TE case the function μ_0 is constant both inside the grating and out while in the TM case an additional $1/\epsilon$ factor must be included. The propagation wavevectors are given by 6.51 for region I, and 6.52 for region III.

$$\begin{aligned} k_{x_1}^I(m) &= \frac{2\pi}{\Lambda}m + \Phi & (6.51)\\ k_{x_3}^I(m) &= -\sqrt{\omega^2\mu_0\epsilon^I - (k_{x_1}^I(m))^2} & \\ k_{x_1}^{III}(m) &= \frac{2\pi}{\Lambda}m + \Phi & (6.52)\\ k_{x_3}^{III}(m) &= +\sqrt{\omega^2\mu_0\epsilon^{III} - (k_{x_1}^{III}(m))^2} & \end{aligned}$$

where

$$\Phi = \omega\sqrt{\mu_0\epsilon_0}\sin\phi. \tag{6.53}$$

In region I, the electric or magnetic field is of the form

$$f(x_1, x_3) = \sum_m a_m e^{ik_{x_3}^I x_3} e^{i(\frac{2\pi}{\Lambda}m+\Phi)x_1} \tag{6.54}$$

To make the notation compact and easy to understand this function can be written in the form of the product of a covector and a vector. At $x_3 = 0$ the function is given by

$$f = \begin{bmatrix} \ldots & e^{i(\frac{2\pi}{\Lambda}(-1)+\Phi)x_1} & e^{i(\frac{2\pi}{\Lambda}(0)+\Phi)x_1} & e^{i(\frac{2\pi}{\Lambda}1+\Phi)x_1} & \ldots \end{bmatrix} \begin{bmatrix} \cdot \\ a_{-1} \\ a_0 \\ a_1 \\ \cdot \end{bmatrix} \tag{6.55}$$

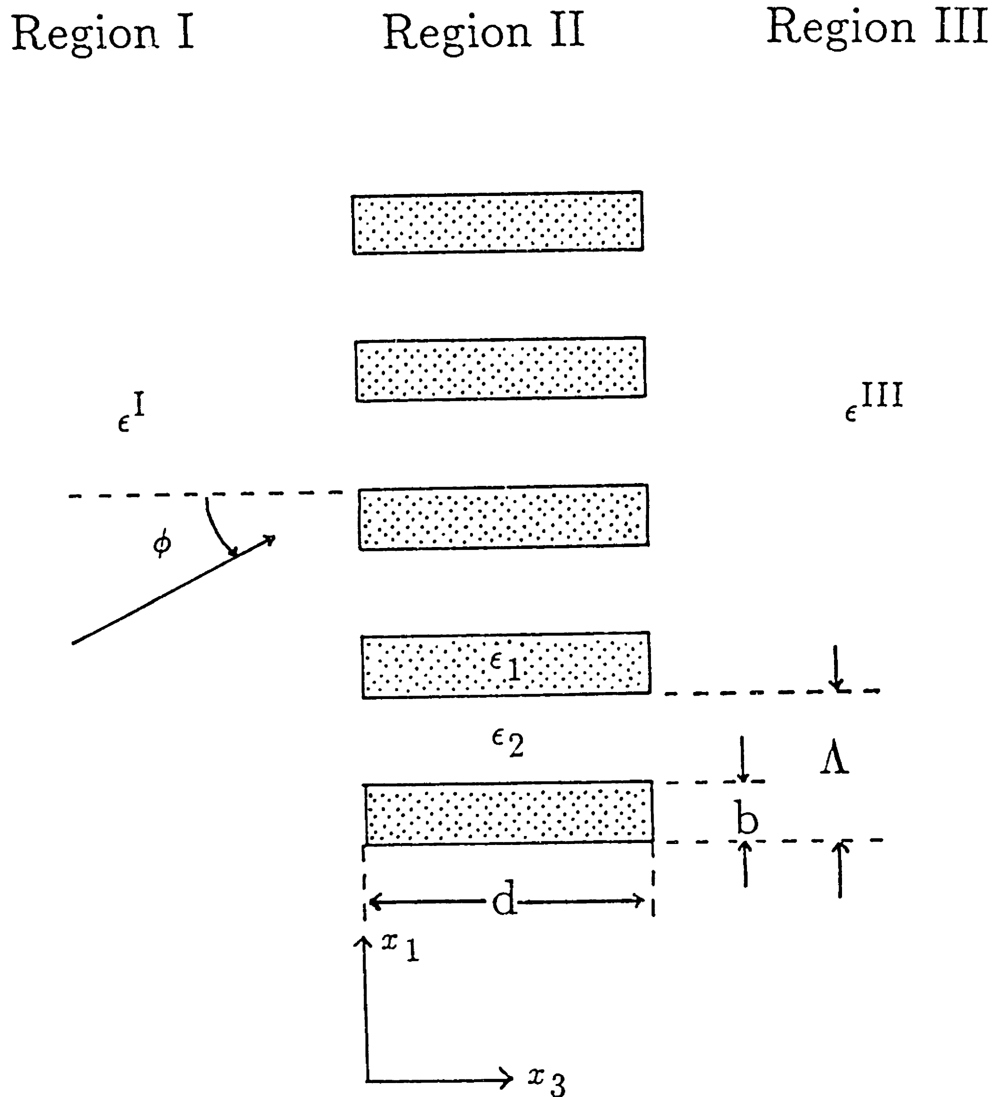

Figure 6.2: This figure shows the three regions of interest: region I with the incident field, region II inside the grating, and region III where the transmitted waves propagate. Inside the grating, in region II, is further divided into a region 1 with dielectric constant ϵ_1 and region 2 with dielectric constant ϵ_2.

The covector depends on the position x_1 while the vector depends only on the unknown coefficients of the Fourier series. If the field amplitudes are written in this form at each boundary it is easy to derive the boundary condition linear equations. Since the boundary conditions must be met at *each* point x_1 then the boundary conditions imply equality between the vector components. In other words, if two functions are equal at each point then their Fourier series coefficients must be equal. In order to write down the boundary condition equations some terms and matrix elements must be defined. The α term takes care of the differences between the TM and the TE polarization cases accounting for the $1/\epsilon$ factor.

$$\alpha^I = \begin{cases} \epsilon_0/\epsilon^I & \text{TM case} \\ 1 & \text{TE case} \end{cases} \tag{6.56}$$

$$\alpha^{III} = \begin{cases} \epsilon_0/\epsilon^{III} & \text{TM case} \\ 1 & \text{TE case} \end{cases} \tag{6.57}$$

Where ϵ^I is the dielectric constant in front of the grating and ϵ^{III} is the constant in back of the grating. The A and B matrices multiply the unknown Fourier coefficients to give the field values in regions I and III while A' and B' give the derivative of the field, corrected with the factor α to account for the TE and TM polarization cases.

$$A_{n,m} = e^{ik_m^I x_3}\delta_{n,m} \tag{6.58}$$

$$A'_{n,m} = \alpha^I ik_m^I e^{ik_m^I x_3}\delta_{n,m} \tag{6.59}$$

$$B_{n,m} = e^{ik_m^{III}(x_3-d)}\delta_{n,m} \tag{6.60}$$

$$B'_{n,m} = \alpha^{III} ik_m^{III} e^{ik_m^{III}(x_3-d)}\delta_{n,m} \tag{6.61}$$

The C matrix is only used to account for the $1/\epsilon$ factor in the TM polarization case and contains the Fourier coefficients necessary to multiply by this factor inside the grating region. For TE polarization it is just the identity matrix

$$C_{n,m} = \begin{cases} \delta_{n,m} & \text{TE case} \\ c_{n-m} & \text{TM case} \end{cases} \tag{6.62}$$

where c_k are the Fourier coefficients for the square wave function $\epsilon_0/\epsilon(x_1)$. The D^+ and D^- matrices multiply the eigenvector matrix to give the field inside the grating region propagating in the positive and negative x_3 direction respectively. The D'^+ and D'^- multiply to eigenvector matrix to

give the derivative. Note that these matrices must be multiplied by the C matrix to give the correct factor for the TM case.

$$D^{+}_{n,m} = e^{i\gamma_m x_3}\delta_{n,m} \quad (6.63)$$

$$D'^{+}_{n,m} = i\gamma_m e^{i\gamma_m x_3}\delta_{n,m} \quad (6.64)$$

$$D^{-}_{n,m} = e^{-i\gamma_m x_3}\delta_{n,m} \quad (6.65)$$

$$D'^{-}_{n,m} = -i\gamma_m e^{-i\gamma_m x_3}\delta_{n,m} \quad (6.66)$$

The R and R' vectors give the incident plane wave and it's derivative corrected by α to account for the TM case.

$$R_n = e^{-ik_0^I x_3}\delta_n \quad (6.67)$$

$$R'_n = -\alpha^I ik_0^I e^{-ik_0^I x_3}\delta_n \quad (6.68)$$

The following are the unknown Fourier coefficient vectors:

- "a" is the reflected amplitude vector.
- "b" is the transmitted amplitude vector.
- "c^+" is the forward propagating eigenvector amplitude array and must be multiplied by E, the eigenvector matrix, to give the Fourier coefficients of the field inside the grating.
- "c^-" is the backward propagating eigenvector amplitude array.

and the known incident plane wave

- "R" is the incident plane wave amplitude.

The boundary equations are then given by

$$a + R = Ec^+ + E^- c^- \quad (6.69)$$

$$b = ED^+(d)c^+ + ED^-(d)c^- \quad (6.70)$$

which is the constraint that the field be continuous at $x_3 = 0$ and $x_3 = d$ respectively. The requirement that the derivative of the field with respect to x_3, corrected for the $1/\epsilon$ factor, is given by

$$A'a + R' = CED'^+(0)c^+ + CED'^-(0)c^- \quad (6.71)$$

$$B'b = CED'^+(d)c^+ + CED'^-(d)c^-. \quad (6.72)$$

From these four matrix equations the vectors a and b can be eliminated resulting in two equations with two unknown vectors, c^+ and c^-. The resulting equation is

$$\begin{bmatrix} A'E - CED'^+(0) & A'E - CED'^-(0) \\ B'ED^+(d) - CED'^+(d) & B'ED^-(d) - CED'^-(d) \end{bmatrix} \begin{bmatrix} c^+ \\ c^- \end{bmatrix} = \begin{bmatrix} A'R - R' \\ 0 \end{bmatrix} \tag{6.73}$$

After evaluating the following matrix elements

$$M^+_{n,m} = A'E - CED'^+(0) \tag{6.74}$$
$$M^-_{n,m} = A'E - CED'^-(0) \tag{6.75}$$
$$N^+_{n,m} = B'ED^+(d) - CED'^+(d) \tag{6.76}$$
$$N^-_{n,m} = B'ED^-(d) - CED'^-(d). \tag{6.77}$$

the task is to solve the set of equations

$$\begin{bmatrix} M^+ & M^- \\ N^+ & N^- \end{bmatrix} \begin{bmatrix} c^+ \\ c^- \end{bmatrix} = \begin{bmatrix} A'R - R' \\ 0 \end{bmatrix} \tag{6.78}$$

The above matrix is not well conditioned and if it is solved with a standard linear algebra program there may be serious numerical errors introduced in problems with deep gratings. The problem results from the fact that the N^+ matrix contains elements that decay exponentially with grating depth and the N^- matrix has elements that grow exponentially with depth. To circumvent this problem, the system of equations is solved in two steps. Consider the equation

$$N^+c^+ + N^-c^- = 0. \tag{6.79}$$

Finding c^- in terms of c^+ gives

$$c^- = (-(N^-)^{-1}N^+)c^+ \tag{6.80}$$
$$= \Delta c^+ \tag{6.81}$$
$$\Delta = (D'^-)^{-1}E^{-1}C^{-1}B'ED^+ + (D^-)^{-1}E^{-1}B'^{-1}CED'^+ - (D'^-)^{-1}D^+ - (D^-)^{-1}D^+ \tag{6.82}$$

resulting in the following equation:

$$(M^+ + M^-\Delta)c^+ = r. \tag{6.83}$$

This equation is well conditioned because the matrix Δ is small compared to M which does not depend on the grating depth. Other workers have observed this problem without solving it. For example in Knop [53] the following quotation appears:

> For large grating depths the matrices .... tend to become indefinite and thus cause problems in the numerical inversion.

Once the linear equation routine returns the arrays c^+ and c^- the output vector, b, and the reflected vector a follow from the boundary condition equations

$$a = Ec^+ + Ec^- - R \tag{6.84}$$

$$b = ED^+(d)c^+ + ED^-(d)c^-. \tag{6.85}$$

The power flow in the x_3 direction is derived from the complex form of Pointing's theorem, where the time average power is given by

$$< S >= \frac{1}{2}\mathbf{Re}(\mathbf{E} \times \mathbf{H}^*) \tag{6.86}$$

where $\mathbf{E}$ is the electric field vector and $\mathbf{H}$ is the magnetic field vector. The efficiency equations are derived from this expression. For the TE case the equations are

$$\frac{I_m}{I_0} = a_m a_m^* \frac{\mathbf{Re}\left(k_{x_3}^{III}(m)\right)}{\mathbf{Re}\left(k_{x_3}^{I}(0)\right)} \tag{6.87}$$

and for the TM case they are

$$\frac{I_m}{I_0} = a_m a_m^* \frac{\mathbf{Re}\left(\frac{k_{x_3}^{III}(m)}{\epsilon^{III}}\right)}{\mathbf{Re}\left(\frac{k_{x_3}^{I}(0)}{\epsilon^{I}}\right)}. \tag{6.88}$$

6.3 Solving the Equations with the Algebraic Method

Consider first the TE polarization case where the master differential equation is given by

$$\frac{d^2 E_2}{dx_1^2} + (\omega^2 \mu_0 \epsilon(x_1) - \gamma^2) E_2 = 0. \tag{6.89}$$

If the eigenvalue, γ^2 were already known then the solution to this equation would be simple. In region 1, (see Fig. 6.2) with $\epsilon = \epsilon_1$, and in region 2 where $\epsilon = \epsilon_2$ this is just a constant coefficient linear differential equation whose solution is determined almost by inspection. The difficulty is to patch the solutions in region 1 and region 2 together so that the tangential electric and magnetic fields are continuous. Since the **H** vector is given by

$$\mathbf{H} = \frac{1}{i\omega\mu_0}\left(\frac{\partial E_2}{\partial x_1}\hat{\mathbf{x}}_3 - \frac{\partial E_2}{\partial x_3}\hat{\mathbf{x}}_1\right) \tag{6.90}$$

the derivative of E_2 with respect to x_1 must be continuous across the boundary where ϵ changes abruptly. Defining the constants β and Γ to be

$$\beta = \sqrt{\omega^2\mu_0\epsilon_1 - \gamma^2} \tag{6.91}$$

$$\Gamma = \sqrt{\omega^2\mu_0\epsilon_2 - \gamma^2} \tag{6.92}$$

the solutions for the field E_2 are linear combinations of the following functions:

$$\theta = \begin{cases} \cos(\beta x_1) & 0 \le x_1 \le c_1 \\ \cos(\beta c_1)\cos(\Gamma(x_1 - c_1)) - \frac{\beta}{\Gamma}\sin(\beta c_1)\sin(\Gamma(x_1 - c_1)) & c_1 \le x_1 \le \Lambda \end{cases}$$

$$\psi = \begin{cases} \frac{1}{\beta}\sin(\beta x_1) & 0 \le x_1 \le c_1 \\ \frac{1}{\beta}\sin(\beta c_1)\cos(\Gamma(x_1 - c_1)) + \frac{1}{\Gamma}\cos(\beta c_1)\sin(\Gamma(x_1 - c_1)) & c_1 \le x_1 \le \Lambda. \end{cases}$$

These functions have the following properties:

$$\begin{array}{ll} \theta(0) = 1 & \psi(0) = 0 \\ \theta'(\Lambda) = 0 & \psi'(\Lambda) = 1. \end{array} \tag{6.93}$$

The solutions must not only satisfy the continuity requirement at $x_1 = c_1$ but also satisfy the pseudo-periodicity condition. If

$$u(x_1) = a\theta(x_1) + b\psi(x_1) \tag{6.94}$$

then

$$e^{i\frac{2\pi}{\lambda}\sin\phi}u(0) = u(\Lambda) \tag{6.95}$$

and also for the derivative

$$e^{i\frac{2\pi}{\lambda}\sin\phi}u'(0) = u'(\Lambda). \tag{6.96}$$

In terms of the functions these two equations become:

$$\Phi = \frac{2\pi}{\lambda}\sin\phi \tag{6.97}$$

$$e^{i\Phi\Lambda}a = a\theta(\Lambda) + b\psi(\Lambda) \tag{6.98}$$

$$e^{i\Phi\Lambda}b = a\theta'(\Lambda) + b\psi'(\Lambda) \tag{6.99}$$

so that a non-trivial solution will result when the "determinate" is zero or

$$(\theta(\Lambda) - e^{i\Phi\Lambda})(\psi'(\Lambda) - e^{i\Phi\Lambda}) - \theta'(\Lambda)\psi(\Lambda) = 0 \tag{6.100}$$

Expanding this equation shows that the eigenvalues are the roots of

$$f(\gamma) = \cos(\Phi\Lambda) - \cos(\beta c_1)\cos(\Gamma c_2) + \frac{1}{2}\left(\frac{\beta}{\Gamma} + \frac{\Gamma}{\beta}\right)\sin(\beta c_1)\sin(\Gamma c_2) \tag{6.101}$$

where

$$\beta = \sqrt{\omega^2\mu_0\epsilon_1 - \gamma^2} \tag{6.102}$$

$$\Gamma = \sqrt{\omega^2\mu_0\epsilon_2 - \gamma^2} \tag{6.103}$$

$$c_1 = b\Lambda \tag{6.104}$$

$$c_2 = (1-b)\Lambda \tag{6.105}$$

$$b = \text{linewidth fraction} \tag{6.106}$$

The equations for the TM polarization case are almost identical except for an extra factor called q which accounts for the different boundary conditions.

$$q = \begin{cases} 1 & \text{TE polarization} \\ \epsilon_2/\epsilon_1 & \text{TM polarization} \end{cases} \tag{6.107}$$

$$\theta = \begin{cases} \cos(\beta x_1) & 0 \le x_1 \le c_1 \\ \cos(\beta c_1)\cos(\Gamma(x_1 - c_1)) - q\frac{\beta}{\Gamma}\sin(\beta c_1)\sin(\Gamma(x_1 - c_1)) & c_1 \le x_1 \le \Lambda \end{cases}$$

$$\psi = \begin{cases} \frac{1}{\beta}\sin(\beta x_1) & 0 \le x_1 \le c_1 \\ \frac{1}{\beta}\sin(\beta c_1)\cos(\Gamma(x_1 - c_1)) + q\frac{1}{\Gamma}\cos(\beta c_1)\sin(\Gamma(x_1 - c_1)) & c_1 \le x_1 \le \Lambda. \end{cases}$$

The master eigenvalue equation is thus

$$f(\gamma) = \cos(\Phi\Lambda) - \cos(\beta c_1)\cos(\Gamma c_2) + \frac{1}{2}\left(q\frac{\beta}{\Gamma} + \frac{1}{q}\frac{\Gamma}{\beta}\right)\sin(\beta c_1)\sin(\Gamma c_2) \tag{6.108}$$

This is the equation that is used to find the grating eigenvalues to high accuracy after the matrix method determines the approximate roots. Newton's method quickly converges to the exact eigenvalues given good starting points. In the actual implementation of this function care must be exercised to insure proper normalization since large negative values of ϵ (such as for Aluminum or Gold gratings in the IR) cause the sine and cosine arguments to be large imaginary numbers which will overflow the computer's dynamic range. Renormalization is performed at each iteration step and the function converges to the correct eigenvalue even for large negative values of ϵ.

Another problem that can occur in the polishing of the eigenvalue roots is that Newton's method converges to a root that has already been found. For a large range of grating parameters, the roots tend to come in pairs. The program makes sure that each root is unique by keeping track of the last root found and polishing the roots in decreasing order. The last root found is "divided out" of the function so that the roots of

$$G(z) = \frac{f(z)}{z - z_{i-1}} \tag{6.109}$$

where z_{i-1} is the last root found are are determined. Special care is taken in evaluating the function $G(z)$ and its derivative $G'(z)$ so that they are correct and smooth near and even at $z = z_{i-1}$.

6.4 Sample Calculation Results

In order to optimize the parent gratings used in the achromatic holographic configuration, a set of calculations were performed. The period is determined by the desired final grating period, 200nm, and the wavelength is fixed by the source, λ =193nm. When using a pure phase grating in quartz the only parameters that can be varied are the linewidth, b, and the etched depth, d. Figure 6.3 shows the first order efficiency as a function of depth and linewidth for both the TE and TM polarizations. The contours are at 10% levels. Notice the large area of parameter space that has an efficiency of over 20%. The maximum efficiency of the TE polarization, 29.9%, occures with a linewidth of b=0.3 at a depth of 140nm and for the TM polarization the maximum first order efficiency is 26.3% at a depth of 210nm with a

linewidth of 0.6. A simple scalar theory calculation would suggest that the maximum would be 50% and would occur at a linewidth of 0.5 and a depth of 161nm. For the recombiner grating in the achromatic holography system the minus second diffracted order is used. A calculation of the -2 order with an incident beam angle of 75 degrees is shown in 6.4. A intriguing result is that the minus second order efficiency can be very high. In the TE polarization the maximum second order efficiency is an astonishing 83.7% at a linewidth of 0.2 and depth of 350nm. The results for the TM polarization are equally impressive: 90.2% into the -2 order at a linewidth of 0.15 and a depth of 475nm. Although it is not always possible to precisely control the linewidth and etched depth, knowing the optimum parameters to shoot for can make a tremendous improvement in the throughput of an instrument such as the achromatic holographic system, especially since the overall efficiency is a product of two or more grating efficiencies.

Conducting transmission gratings with a period that is much *smaller* than the wavelength of the incident radiation transmit light polarized with the electric field perpendicular to the grating lines with less attenuation and reflection than light polarized parallel to the grating lines. Therefore these gratings can act as polarizers. This effect is exploited in the alignment system described in chapter 5. There are also several applications where fine period gratings are the polarizer of choice. Although dichroic plastic (polaroid) material makes an excellent polarizer in the near IR, it cannot be used in a cryogenic environment. However, grating polarizers made with Au or Al lines on quartz or sapphire substrates can be used. The calculated zero order transmission for a 200nm period Au grating is plotted for both polarizations in Fig. 6.5 and Al grating in Fig. 6.6 as a function of depth. The wavelength is 0.95μm and the optical constants for Au ($n = 0.174 + i5.691$) and Al ($n = 1.75 + i8.5$) were taken from [67]. An interesting effect is observed in Fig. 6.7 where the transmitted zero order efficiency of Au and Al gratings are plotted together. As the depth is varied, "thin-film" interference effects are observed.

Several sample calculations have been presented to illustrate the abilities of the electromagnetic theory calculation program. In the phase grating case, the wavelength and the grating period were almost the same making simple scalar analysis inadequate, and in the polarizer case the vector nature of light is an essential part of the calculated effect.

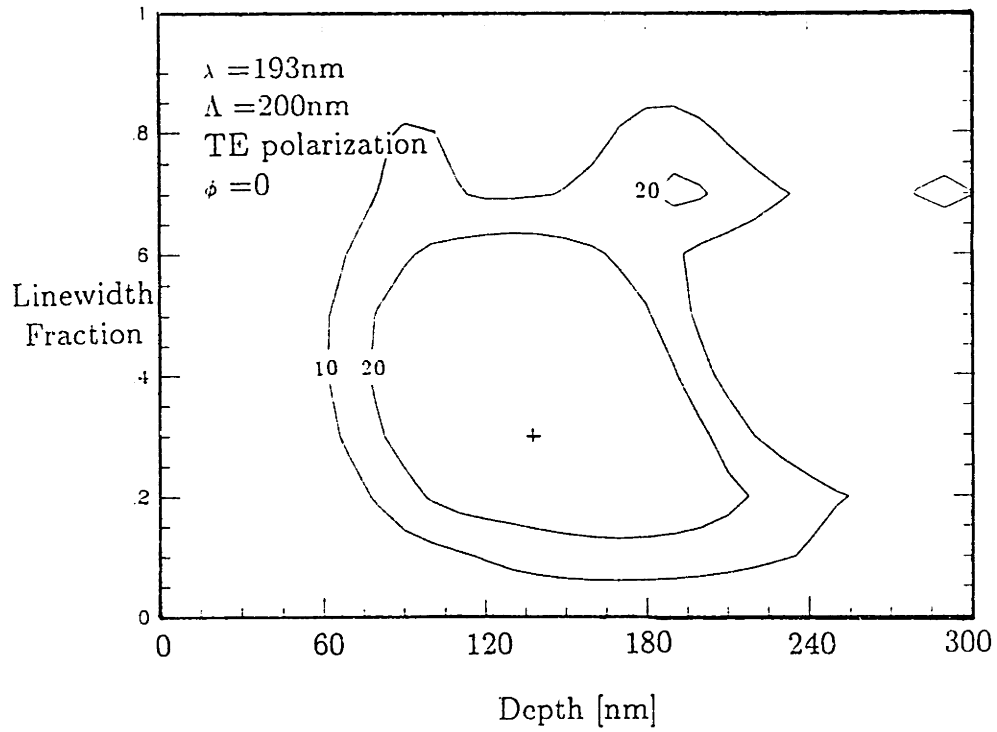

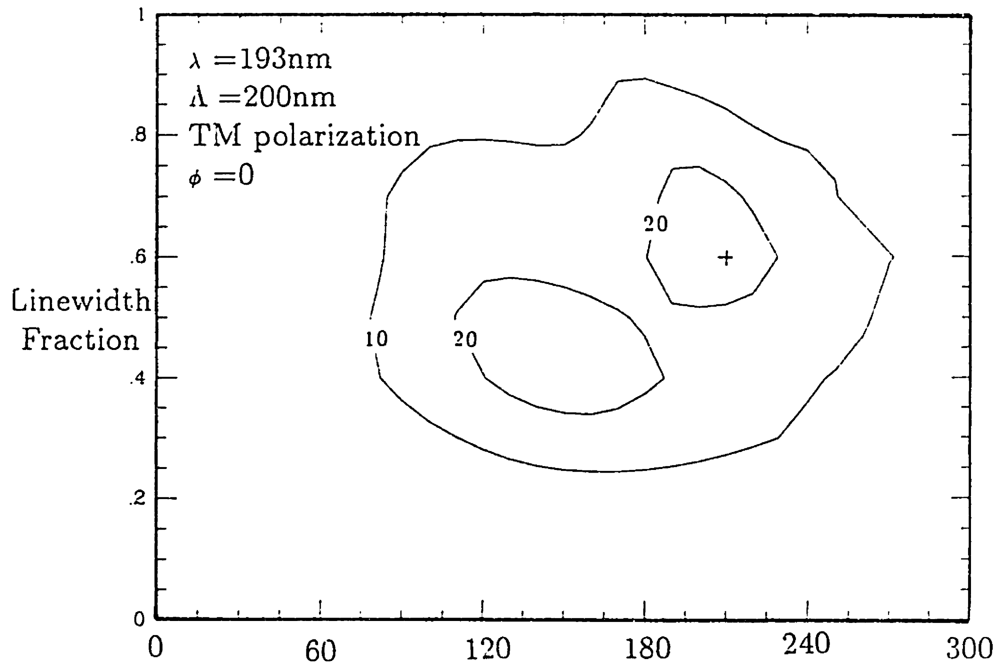

Figure 6.3: This shows the calculated first order efficiency for both the TE and TM polarization of a 200nm period pure phase grating etched in quartz (n=1.6) with a λ =193nm source as a function of depth and linewidth. The contours are at 10% levels. The maximum TE efficiency occures for a linewidth of 0.3 and a etched depth of 140nm and for the TM polarization at a linewidth of 0.6 and depth of 300nm.

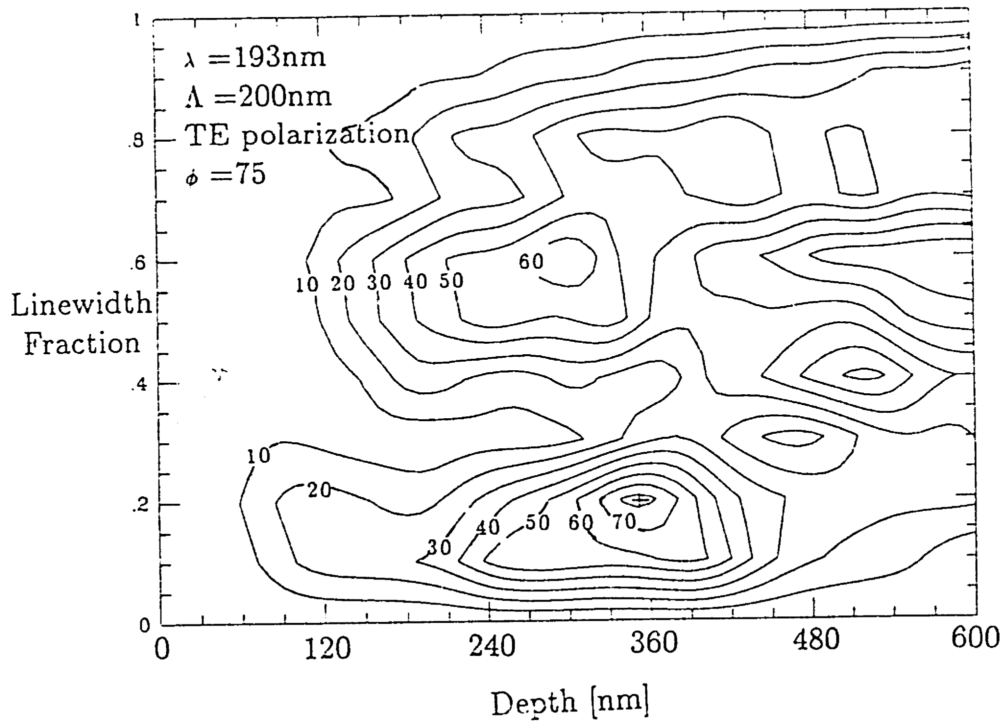

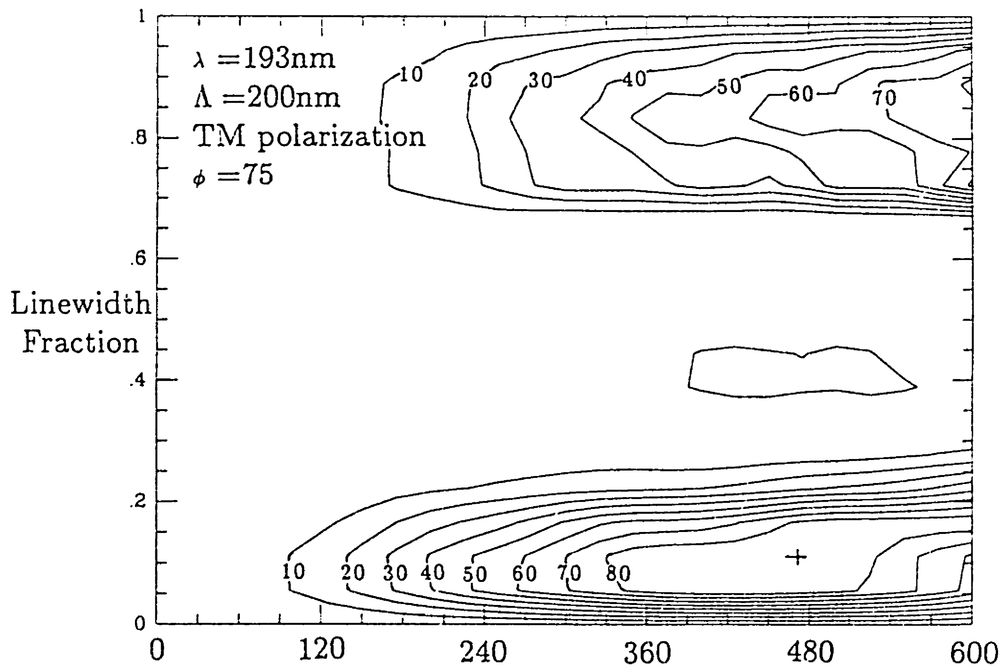

Figure 6.4: This shows the minus second order efficiency for both TE and TM polarizations with the incident wave at an angle of 75 degrees. For both polarizations, the efficiency is surprisingly high with a maximum of 83.7% for TE at b=0.2 and a depth of 350nm and 90.2% at b=0.15 and a depth of 475nm for the TM polarization.

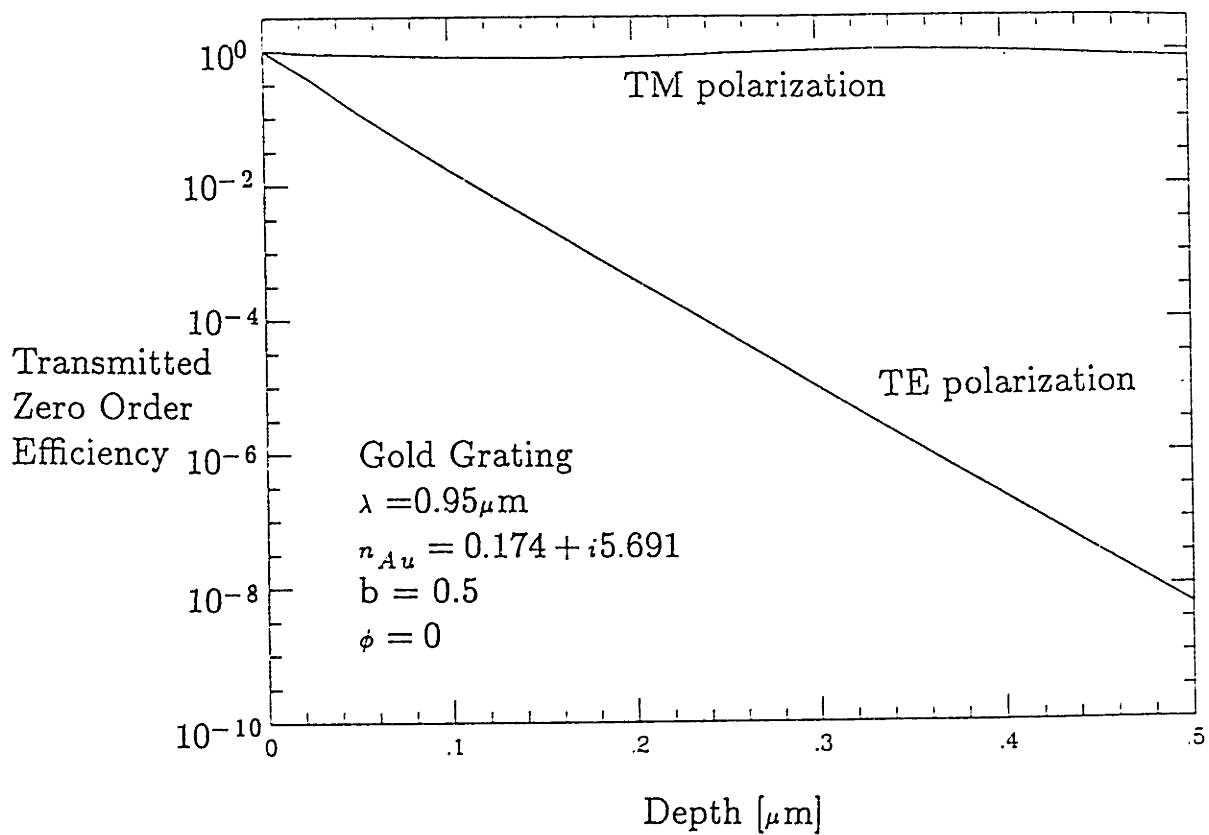

Figure 6.5: This plot shows the calculated zero order transmitted efficiency for a 200nm period Au grating with a linewidth of 0.5 as a function of depth.

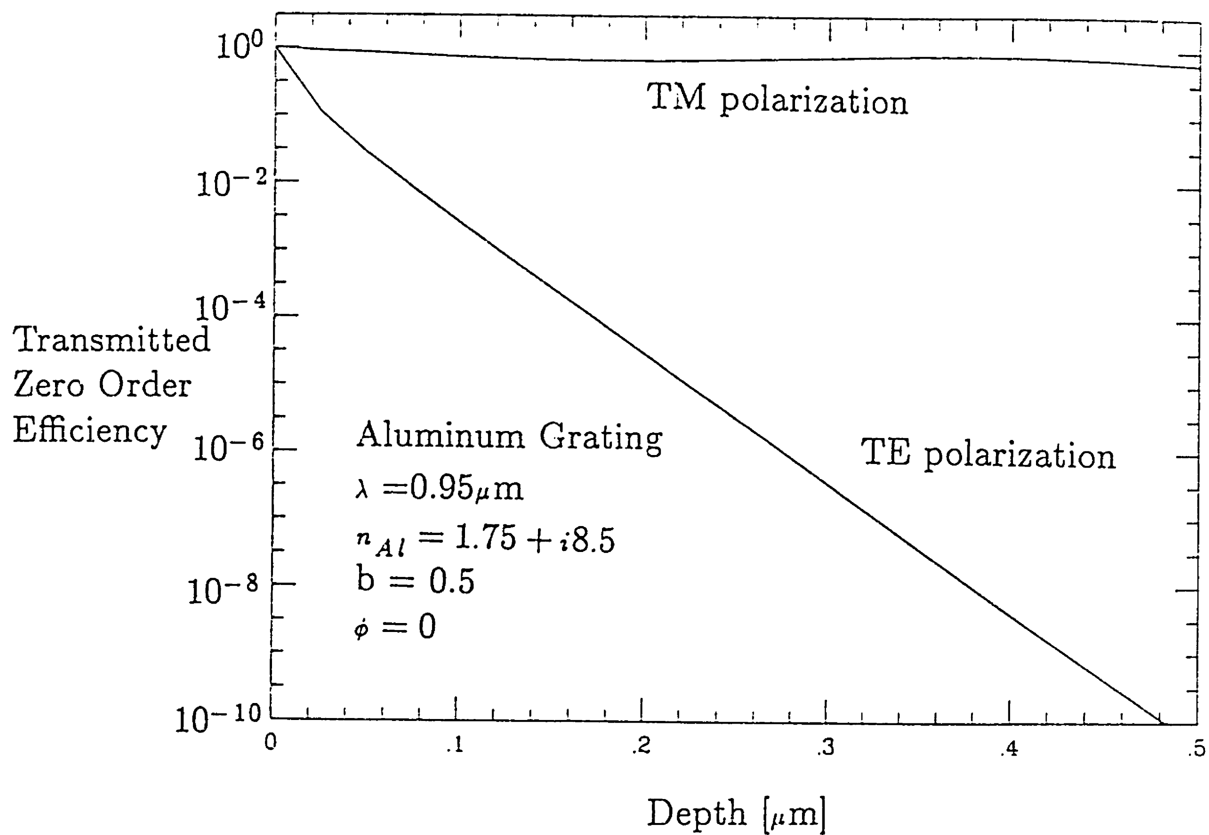

Figure 6.6: This plot shows the calculated zero order transmitted efficiency for a 200nm period Al grating with a linewidth of 0.5 as a function of depth.

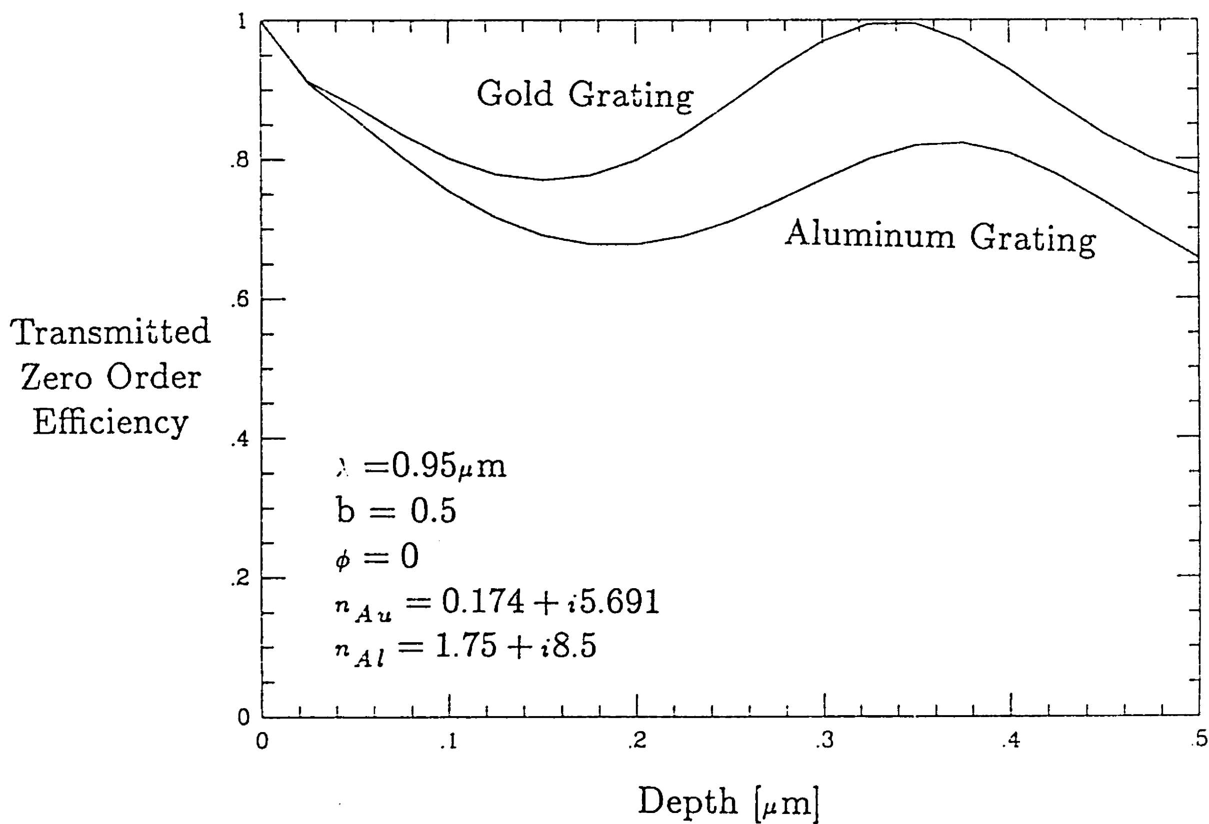

Figure 6.7: This plot show the zero order transmitted beam for Au (top trace) and Al wire grid polarizer gratings. The period of the gratings is $0.2\mu m$ with a linewidth of 0.5 and the wavelength is $\lambda = 0.95\mu m$. Notice the "interference" effect as the depth is varied from 0 to $0.5\mu m$.

6.5 Conclusion

A method for rigorously solving Maxwell's equations for a square wave grating structure has been implemented and found to give accurate results in each case where published calculations from other workers are available to cross check and in various limiting cases. The technique uses the eigenvalues from a complex general matrix routine to determine estimates of the grating eigenmodes. The matrix method depends on the convergence of a Fourier series to a discontinuous function for the TE case and to a singular function in the TM case. The Fourier series convergence to a square wave gives an error that is of order $1/N$ where N is the number of Fourier coefficients included and is even slower for the singular derivative of a square wave. However, the computational effort to find the eigenvalues and eigenvectors increases as N^3. Therefore simply increasing the number of modes is an expensive technique for increasing the accuracy of the matrix method. But the matrix method gives "good" estimates of the correct eigenvalues with just a few Fourier terms. The combination of the matrix method with a polishing technique to quickly zero in on the correct eigenvalues once they are approximately known greatly improves the accuracy of the method while the computation time of polishing is only linear in the number of modes.

This program has been very useful in determining optimum parameters for gratings fabricated in our lab. It has been useful for understanding the behavior of very deep gold gratings in the soft x-ray region where even though λ/Λ is small, scalar diffraction theory is not adequate. For higher energy x-rays it has confirmed scalar theory calculations and gives insight into the energy range where the scalar theory breaks down and the vector theory must be used. Further, our gratings have been used as polarizing elements in cryogenic environments where ordinary polaroid material would be inadequate. The behavior of these "wire grid" polarizers when the wavelength is much larger than the period can be analyzed by this program.

Chapter 7

Summary and Future Work

The motivation for much of the work reported here is the development of grating structures with periods $\approx$ 100nm for use in a number of scientific applications such as solid-state quantum-effect electronics studies, x-ray spectroscopy and interferometry, IR polarizers, thin film materials studies and other applications where the characteristic dimensions (wavelengths, scattering lengths, etc.) are very small. Many different approaches were tried before converging to a feedback-controlled achromatic holographic configuration. In this configuration, the achromatic aspect of the interferometer results from the dispersion properties of transmission gratings used in such a way that the net effect of different wavelengths cancels out. Further, the configuration is insensitive to the angle of the incident wave so that sources with poor spatial as well as temporal coherence properties can be used. The feedback system allows for very long exposure times needed when low sensitivity resists and low power sources are used. The feedback system actively canceles the mechanical drift, locking the fringes for exposure times of 20 minutes or longer. Previous efforts in this field (in our lab as well as others) have produced gratings with periods smaller than 120nm but in each case there has been a subtle reason why these gratings were not further processed to produce a structure such as Fig. 2.8. Further, getting good high contrast exposures is only half the battle, turning them into useful grating structures is the other half. Now, at least the process of getting high contrast exposures with periods of about 100nm has been solved.

The first step for future work is to reduce the period of the parent grat-

ings from 240nm to 200nm resulting in a final grating period of 100nm, the approximate limit imposed by the wavelength of the ArF excimer laser, λ =193nm. But even with the current set of gratings there are a large number of exciting applications to be explored. The observability of surface superlattice effects in quantum-effect electronic experiments in Si and GaAs is a strong function of the grating line density. Therefore, incorporating gratings or grids with periods almost a factor of 2 smaller than the current generation should allow either stronger signals to be observed and/or the effects to be seen at higher temperatures. In the area of x-ray diffraction gratings for spectroscopy, the smaller period will yield higher dispersion and in most systems with the other dimensions unchanged, this will result in higher resolution. The basic achromatic configuration is ideal for interferometric measurements in the soft x-ray region and beyond because of the relaxed spatial and temporal coherence requirements. A very recent experiment has demonstrated the diffraction of Na atoms by a 200nm period grating. If a grating interferometer could be constructed for atomic or molecular particles, it could be an extremely sensitive instrument.

There are also a many interesting scientific applications for the 200nm and larger period gratings that are made with conventional holographic lithography. Before developing the feedback locking of the fringes, exposing the gratings with this system was a very tedious process, resulting in relatively small areas of good grating. When only a small area is needed, the interferometer arms can be made short. Since the fringe phase noise is approximately proportional to the size of the interferometer, sufficient contrast could be achieved to produce useful gratings. But under these conditions, the exposure and development times had to be just right. The process latitude was quite poor and good results required both patience and skill. While attempting to expose larger area gratings, the magnitude of the fringe fluctuations was measured using photodiodes and discovered to be much worse than visual observations of fringe movement on a fluorescent card would indicate. The use of active feedback has worked very well. Now, the feedback system gives much higher contrast to large area gratings than was achieved even for small area gratings in the past. The system is so stable that the optics table can be sharply struck without perturbing the locking of the fringes or the exposure while previously, just *"thinking"* about touching the table could ruin an exposure.

The feedback locking of fringes for grating fabrication should allow one

to use a lower power and much less expensive laser since the fringe drift even for very long exposure times is controlled by the feedback system and thus will be small. An exciting possibility is to extend feedback fringe locking to general holograms. For a general hologram, the simple beamsplitter used to make the Mach-Zehnder interferometer cannot be used but perhaps a poor quality hologram could be used as the feedback beamsplitter. The feedback locking eliminates the subtle and sometimes uncontrollable environmental disturbances that can make holographic exposures a fussy and frustrating process.

X-ray nanolithography masks have been successfully made from patterns exposed by electron beam lithography at IBM. The patterns for these exposures were generated at MIT and sent electronically over the network to IBM's Yorktown Heights research lab. The high resolution vector scan machine VS-6 exposed the patterns on specially prepared substrates. A trilevel process then transforms the thin 80nm PMMA into a high contrast x-ray nanolithography mask. These patterns were then replicated at MIT using x-ray nanolithography which is a high-contrast, and large process latitude technique. The combination of electron beam lithography and x-ray nanolithography gives researchers the best of both technologies: the arbitrary pattern generation and high resolution of electron beam lithography and the good contrast and large process latitude of x-ray nanolithography.

Although, the original motivation for developing this technology was to make 100nm period gratings for x-ray spectroscopy, the arbitrary pattern generation capabilities of electron beam lithography coupled with the high contrast of x-ray nanolithography will probably have a greater impact in electronic microcircuit applications rather than strictly periodic structures. Since periodic structures can be holographically generated over large areas, for applications such as x-ray spectroscopy, holographic methods will be more practical. The generality, small feature sizes, and large process latitude, characteristic of this combination of technologies should open wide vistas for future microcircuit, quantum electronic, optoelectronic, and, no doubt, other applications. However, to realize the full capabilities of this technology, x-ray nanolithography *alignment* techniques must be developed. With high resolution alignment capability, microcircuit researchers will have another very powerful tool to explore complex circuits and devices.

A technique using the partial polarization properties of transmission gratings and a photoelastic modulator (PEM) has been developed which

has very high resolution. The signal, measured on a lock-in amplifier, is proportional to twice the sine of the angle between the PEM crystal axis and the grating lines. Since the signal is *first* order, for small angles, and since lock-in amplifier electronics can measure very small signals buried in noise the resolution of this technique is quite high. The high inherent resolution of this technique may suggest new applications for future research.

In order to analyze gratings under conditions where the scalar theory would be inadequate, a computer program that rigorously solves Maxwell's equations for a rectangular wave, lamellar, grating has been implemented. The program uses the eigenmode method to solve for the fields both inside and outside the grating. The eigenmodes are first found using a matrix technique in which the eigenvalues of a finite size complex general matrix approximate the eigenvalues of the infinite dimensional matrix containing all the Fourier series expansion terms. These approximate eigenvalues are polished so that they will be the solution to a transcendental algebraic equation giving the exact grating eigenmodes. The combination of the two approaches works well since the "searching" part of the problem is accomplished by the matrix eigenvalue routine and the final convergence of the eigenmode, to many decimal places, is done by the numerical solution, using Newton's method, of the transcendental algebraic equation. After finding a set of eigenmodes the boundary condition equations are then applied yielding a large set of coupled linear equations. These equations are normalized and solved in such a way that minimizes errors associated with illconditioned matrices giving the fields both inside and outside the grating.

A number of improvements can be made to the program to make it more efficient. However, only careful measurements of real gratings will reveal how well the program solves Maxwell's equations. For future work, a reliable data base of grating parameters and efficiencies should be generated including IR through x-ray wavelengths and compared to the theoretical calculations. Only then can a high level of confidence be placed in a program that has almost 3000 lines of fortran code.

In summary, a number of new techniques have been developed to fabricate, align, and predict the behavior of very small period gratings and (using the combination of electron beam lithography with x-ray nanolithography) non-periodic structures as well. These advances provide the tools for a variety of scientific and engineering applications of fine linewidth struc-

tures.

Bibliography

[1] M.C. Huntly, *Diffraction Gratings,* New York: Academic Press, 1982.

[2] D. Rudolph and G. Schmahl, "Verfahren sur Herstellung von Röntgenlinsen und Beugungsgittern," *Umschau Wiss,* vol. 67, pp. 255, 1967.

[3] A. Labeyrie, and J. Flamand, "Spectrographic Performance of Holographically made Diffraction Gratings," *Opt. Commun.,* vol. 1, pp. 5-8, April 1969.

[4] E.H. Anderson, K. Komatsu, H.I. Smith, "Achromatic Holographic Lithography in the Deep UV," *J. Vac. Soc. B,* vol. 6, pp. 216-218 Jan.-Feb. 1988.

[5] Amnon Yariv, *Optical Electronics,* New York: Holt, Rinehart and Winston 1971.

[6] D.A. Antoniadis, A.C. Warren, H.I. Smith, "Quantum Mechanical Effects in Very Short and Very Narrow Channel MOSFETs," IEEE Conference Proceedings IEDM 85, pp. 558-561, 1985.

[7] N.M. Ceglio, R.L. Kauffman, A.M. Hawryluk, H. Medecki, "Time resolved x-ray transmission grating spectrometer for studying laser-produced plasmas," *Journal of Applied Optics,* vol. 22, pp. 318-327, Jan. 1985.

[8] E.H. Anderson, C.M. Horwitz, and H.I. Smith, "Holographic lithography with thick photoresist," *Appl. Phys. Lett.,* vol. 49, pp. 874-875, Nov. 1983.

[9] H.I. Smith, E.H. Anderson, and M.L. Schattenburg, "Planar Techniques for Fabricating X-Ray Diffraction Gratings and Zone Plates," Symposium on X-Ray Microscopy, Gottingen, Federal Republic of Germany, Sept. 14-16, 1983, in: D. Rudolph and G. Schmahl, Eds, Springer Series in Optical Sciences, *Vol. 43: X-Ray Microscopy*, Berlin: Springer-Verlag, pp. 51-61, 1984.

[10] C.V. Shank and R.V. Schmidt, "Optical Technique for producing $0.1\mu m$ periodic surface structures," *Appl. Phys. Lett.*, vol. 23, pp. 154-155, Aug. 1973.

[11] G.C. Bjorklund, S.E. Harris, and J.F. Young, "Vacuum Ultraviolet Holography," *Appl. Phys. Lett.*, vol. 25, pp. 451-452, Oct. 1974.

[12] A.M. Hawryluk, H.I. Smith, and D.J. Ehrlich, "Deep-UV spatial-frequency doubling by combining multilayer mirrors with diffraction gratings," *J. Vac. Sci. Technol. B*, vol. 1, pp. 1200-1203, Oct-Dec 1983.

[13] F.J. Weinberg and N.B. Wood, "Interferometer Based on Four Diffraction Gratings," *J. Sci. Instrum.*, vol. 36, pp. 227-230, 1959.

[14] E.N. Leith and B.J. Chang, "Space-Invariant Holography with Quasi-Coherent Light," *App. Opt.*, vol. 12, pp. 1957-1963, Aug. 1973.

[15] Y.S. Cheng, "Fringe formation in incoherent light with a two-grating interferometer," *App. Opt.* vol. 23, pp. 3057-3059, Sept. 1984.

[16] D. Keith, M.L. Schattenburg, and D. Pritchard,
In preparation to be published in Science.

[17] L.E. Nilsson and H. Ahlén, "Stabilization of the exposing interference pattern in holographic grating production," *SPIE vol. 240 Periodic Structures, Gratings, Moiré Patterns and Diffraction Phenomena*, pp. 22-26, 1980.

[18] E.H. Anderson, and H.I. Smith, "Fabrication by Tri-Level Electron Beam Lithography of X-Ray Masks with 50nm Linewidths, and Replication by X-Ray Nanolithography," in: R. Castagné and J. Perrocheau., (eds), *Microcircuit Engineering 6. (1987)*, pp. 541-546., Amsterdam: North-Holland 1987.

[19] H.I. Smith, "A model for Comparing Process Latitude in UV, deep-UV and X-ray Lithography," *J. Vac. Soc. Technol. B.*, vol. 6, pp. 216-220, Jan 1988.

[20] D.C. Flanders, "Replication of 175-Å lines and spaces in polymethylmethacrylate using x-ray lithography," *Appl. Phys. Lett.* vol. 36, pp. 93-96, Jan 1980.

[21] S.Y. Chou, D.A. Antoniadis, and H.I. Smith, "Observation of electron velocity overshoot in sub-100nm-channel MOSFETs in silicon," *IEEE Elect. Dev. Lett.*, vol. EDL-6, pp. 665-667, Dec. 1985.

[22] N.M. Ceglio, A.M. Hawryluk, and R.H. Price, "Imaging x-ray Spectrometer for laser fusion applications," *Appl. Opt.*, vol. 21, pp. 3953-3960, Nov. 1982.

[23] A.C. Warren, D.A. Antoniadis, H.I. Smith, and J. Melngailis, "Surface Superlattice Formation in Silicon Inversion Layers using 0.2μm-Period Grating-Gate Electrodes," *IEEE Elect. Dev. Lett.*, vol. EDL-6, pp. 294-296, June 1985.

[24] M.L. Schattenburg, I. Tanaka, and H.I. Smith, "Microgap X-Ray Nanolithography," in: R. Castagné and J. Perrocheau., (eds), *Microcircuit Engineering 6. (1987)*, pp. 273-279., Amsterdam: North-Holland 1987.

[25] C. Mead, and L. Conway, *Introduction to VLSI Systems,* Reading Massachusetts: Addison-Wesley pp. 115-127, 1980.

[26] Polyimide 2555 electronic grade, DuPont Company Wilmington DE 19898 USA.

[27] H. Neuhaus and M. Allen, personal communication.

[28] D.P. Kern, P.J. Houzego, P.J. Coane, and T.H.P. Chang, "Practical aspects of microfabrication in the 100nm regime," *J. Vac. Sci. Technol. B*, vol. 1, pp. 1096-1100, Oct-Dec 1983.

[29] P. Unger, V. Bögli, and H. Beneking, "Application of Titanium RIE to the Fabrication of nm-scale structures," in: Lehmann H.W. and

Bleiker Ch.,(eds), *Proc. Microcircuit Engineering 5 (1986),* Amsterdam: North-Holland, pp. 279-286, 1986.

[30] Sel-Rex division Oxy Metal Industries Corp. 75 River Road Nutley, New Jersey, 07110 USA.

[31] E.H. Anderson, A.M. Levine, and M.L. Schattenburg, "Transmission X-Ray Diffraction Grating Alignment Using a Photoelastic Modulator," to be published in *Applied Optics.*

[32] N.M. Ceglio, R.L. Kauffman, A.M. Hawryluk, and H. Medecki, "A Time Resolved X-ray Transmission Grating Spectrometer for Investigation of Laser Produced Plasmas," *Journal of Applied Optics,* vol. 22, pp. 318-327, Jan. 1983.

[33] C.R. Canizares, M.L. Schattenburg, and H.I. Smith, "The High Energy Transmission Grating Spectrometer for AXAF," *X-Ray Instrumentation in Astronomy,* S.P.I.E. vol. 597, pp. 253-260, 1985.

[34] Dr. Paul Rockett, personal communication.

[35] H.E. Torberg, W.J. Rowan, and J.R. Vyce, Section 16: Optical Instruments for Metrology, in: W.G. Driscoll and W. Vaughn, Eds., *Handbook of Optics*, New York: McGraw-Hill Book Company, pp. 16-42, 1978.

[36] James C. Kemp, "Piezo-Optical Birefringence Modulators: New Use for a Long-Known Effect," *J. Opt. Soc. Am.*, vol. 59, pp. 950-954, Aug. 1969.

[37] S.N. Jasperson and S.E. Schnatterly, "An Improved Method for High Reflectivity Ellipsometry Based on a New Polarization Modulation Technique," *Rev. Sci. Inst.*, vol. 40, pp. 761-767, June 1969.

[38] H.A. Haus, *Waves and Fields in Optoelectronics,* New Jersey: Prentice-Hall Inc, pp. 370, 1984.

[39] Melles Griot No. 3 FCG 167.

[40] Model PEM-80, Hinds International, Inc., Portland, Oregon.

[41] Model D656, Davidson Optronics, Inc., West Covina, Calif.

[42] T.K. Gaylord and M.G. Moharam "Analysis and Applications of Optical Diffraction by Gratings" *IEEE Proc.*, vol 73, pp. 894-937, May 1985.

[43] H. Kogelnik, "Coupled wave theory for thick hologram gratings," *Bell syst. Tech. J.*, vol. 48, pp. 2909-2947, Nov. 1969.

[44] G.L. Fillmore and R.F. Tynan, "Sensitometric characteristics of hardened dichromated-gelatin films," *J. Opt. Soc. Amer.*, vol. 61, pp. 199-203, Feb. 1971.

[45] J.A. Kong, "Second-order coupled-mode equations for spatially periodic media," *J. Opt. Soc. Amer.*, vol. 67, pp 825-829, June 1977.

[46] R. Magnusson and T.K. Gaylord, "Analysis of multiwave diffraction of thick gratings," *J. Opt. Soc. Amer.*, vol 67, pp. 1165-1170, Sept. 1977.

[47] M.G. Moharam and T.K. Gaylord, "Analysis of multiwave diffraction of thick gratings," *J. Opt. Soc. Amer.*, vol. 71, pp. 811-818, July 1981.

[48] M.G. Moharam and T.K. Gaylord, "Three-dimensional vector coupled-wave analysis of planar-grating diffraction," *J. Opt. Soc. Amer.*, vol. 73, pp. 1105-1112, Sept. 1983.

[49] T. Tamir, H.C. Wang, and A.A. Oliner, "Wave propagation in sinusoidally stratified dielectric media," *IEEE Trans. Microwave Theory Tech.*, vol. MTT-12, pp. 323-335, May 1964.

[50] T. Tamir and H.C. Wang, "Scattering of electromagnetic waves by a sinusoidal stratified half-space I," *Can. J. Phys.*, vol. 44, pp. 2073-2094, Sept. 1966.

[51] T. Tamir, "Scattering of electromagnetic waves by a sinusoidal stratified half-space II," *Can. J. Phys.*, vol. 44, pp. 2461-2494, Oct. 1966.

[52] C.B. Burckhardt, "Diffraction of a plane wave at a sinusoidally stratified dielectric grating," *J. Opt. Soc. Amer.*, vol. 56, pp. 1502-1509, Nov. 1966.

[53] K. Knop "Rigorous diffraction theory for transmission phase gratings with deep rectangular grooves," *J. Opt. Soc. Amer.*, vol. 68, pp. 1206-1210, Sept 1978.

[54] F.G. Kaspar, "Diffraction by thick, periodically stratified gratings with complex dielectric constant," *J. Opt. Soc. Amer.*, vol. 63, pp. 37-45, Jan. 1973.

[55] S.T. Peng, T. Tamir, and H.L. Bertoni, "theory of periodic dielectric waveguides," *IEEE Trans. Microwave Theory Tech.*, vol. MTT-23, pp. 123-133, Jan. 1975.

[56] R.S. Chu and J.A. Kong, "Modal theory of spatially periodic media," *IEEE Trans. Microwave Theory Tech.*, vol. MTT-25, pp. 18-24, Jan. 1977.

[57] R. Magnusson and T.K. Gaylord, "Equivalence of multiwave coupled-wave theory and modal theory for periodic-media diffraction," *J. Opt. Soc. Amer.*, vol. 68, pp. 1777-1779, Dec. 1978.

[58] R. Magnusson and T.K. Gaylord, "Planar dielectric grating diffraction theories," *Appl. Phys. B*, vol. 28, pp. 1-14, May 1982.

[59] I.C. Botten, M.S. Craig, R.C. McPhedran, J.L. Adams, and J.R. Andrewartha, "The dielectric lamellar diffraction grating," *Optica Acta*, vol. 28, pp. 413-428, 1981.

[60] I.C. Botten, M.S. Craig, R.C. McPhedran, J.L. Adams, and J.R. Andrewartha, "The finitely conducting lamellar diffraction grating," *Optica Acta*, vol. 28, pp. 1087-1102, 1981.

[61] I.C. Botten, M.S. Craig, and R.C. McPhedran, "Highly conducting lamellar diffraction gratings," *Optica Acta*, vol. 28, pp. 1103-1106, 1981.

[62] G. Tayeb and R. Petit, "On the numerical study of deep conducting lamellar diffraction gratings," *Optica Acta*, vol. 31, pp. 1361-1365, 1984.

[63] B.T. Smith, J.M. Boyle, J.J. Dongarra, B.S. Garbow, Y. Ikebe, V.c. Klema, and C.B. Moler, *Matrix Eigensystem Routines-EISPACK Guide,* New York: Springer-Verlag, 1976.

[64] W.H. Press, B.P. Flannery, S.A. Teukolsky, and W.T. Vetterling, *Numerical Recipes - The Art of Scientific Computing,* London: Cambridge University Press, 1986.

[65] J.J. Dongarra, C.B. Moler, J.R. Bunch, and G.W. Stewart, *LINPACK Users' Guide,* Philadelphia: Siam, 1979.

[66] G.A. Deschamps, "Electromagnetics and Differential Forms," *Proc. IEEE,* vol. 69, pp. 676-696, June 1981.

[67] *American Institute of Physics Handbook 3ed Ed,* New York: McGraw Hill, 1972.